Flexural behaviour of concrete filled tubular flange girders (CFTFGs)

Rana Al-Dujele

A thesis submitted to Brunel University London for the degree of Doctor of Philosophy in College of Engineering, Design and Physical Sciences

2020

I. Abstract

There is an ever-increasing need to develop innovative structural solutions which offer greater efficiency and resilience compared with existing technologies. In construction, both engineers and also society as a whole are becoming more intolerant of practices which are considered unsustainable such as excessive material usage, short life-spans, high maintenance costs, etc. In this context, the research presented in this thesis is focused on a novel and efficient structural shape called a concrete filled tubular flange girder (CFTFG) and the principle aim is to gain a deep understanding of their behaviour through both numerical and analytical modelling.

CFTFGs are steel beams in which the top flange plate is replaced with a hollow steel section which is then filled with concrete. The concrete in the tube strengthens the compression flange of the girder, providing greater torsional stiffness and thereby increasing the lateral-torsional buckling (LTB) resistance of the girder, relative to a regular steel beam of similar proportions. In heavily loaded applications such as bridges and car parks, CFTFGs can result in time and cost savings relative to more traditional sections as much of the fabrication is conducted off-site with fewer splices and complex connections required on-site. The concrete filled tubular flange can theoretically be any shape and the focus in the current research is on simply supported members with either a rectangular or circular top flange, as well as stiffened webs.

CFTFGs are complex members and their behaviour is governed by several inter-related parameters. In order to investigate these, and develop a deeper understanding of the behaviour, a nonlinear three-dimensional finite element (FE) model is developed using the ABAQUS software and validated using available experimental data from the literature. The validated models are then employed to conduct a series of parametric studies to investigate the influence of the most salient parameters on the performance. The finite element models consider the effects of initial geometric imperfections, as well as other geometrical and material nonlinearities, on the response. For comparison purposes, and to observe the effect of the concrete infill, the same girders with a bare steel tubular flange section are also studied.

In addition to the FE model, and with a view to providing designers with convenient guidance, simplified analytical expressions for the flexural capacity of CFTFGs are also proposed, and the results are compared to those from the FE analyses. It is found that concrete filled members exhibit similar buckling shapes to similar sections without the concrete infill but significantly greater buckling resistance. This highlights the influence of the concrete infill which increases the stiffness of the upper flange, and hence allows the member to carry additional bending

moments compared to bare steel sections. The analytical expressions, which are suitable for design, are also shown to be capable of providing an accurate depiction of the bending moment capacity.

In a further development of the work, the ultimate strength of circular CFTFGs under combined axial tension and positive (sagging) bending moment is also investigated, as this is a common scenario in bridge applications. Current design codes do not explicitly include guidance for the design of CFTFGs, which are asymmetric in nature under the combined effects of tension and bending. A finite element model has been developed using ABAQUS to study this behaviour. Based on the finite element analysis, the moment–axial force interaction relationship is presented and a simplified equation is proposed for the design of circular CFTFGs subjected to combined bending and tensile axial force.

The data and analysis presented in this thesis supports the use of concrete filled tubular flange girders in appropriate, heavily-loaded, design scenarios. They are shown to provide an efficient load-carrying solutions, and can cover large spans without the need for intermediary supports. The design expressions proposed are based on a fundamental review of the behaviour and are shown to provide an accurate depiction of the capacity of these sections either in bending or under combined loading.

II. Acknowledgments

First of all, I would like to express my genuine appreciation to my supervisor, Dr. Katherine Cashell, for her continued support and assistance during my doctoral studies and for sharing me here research, patience and enormous expertise. Her advice and encouragement assisted me in conducting my research, preparing this thesis and also overcoming the challenges that encountered during my Ph.D. study. I couldn't ask for a stronger supervisor and mentor for my research.

I would like to acknowledge the financial support provided by Prime Minster office of Iraq and through The Higher Committee of Education Development in Iraq in support of my Ph.D.

I would like to thank my family with all my heart for supporting me spiritually through my life in general and my study. I dedicate this thesis to my brother, Mr. Ali Aldujaili who stood beside me through the hardest times during my studies, and my sisters, Shruq and Luma, for their everlasting faith. I am very grateful to my son, Ahmed, for inspiring me with their care and love.

To my husband, Yasir Al-Okbi, words are inadequate to express my appreciation to and feelings for you. Thank you for your enduring love, for having believed in me long when I lost faith in myself and for your patience. Praise be to God for your presence in my life.

Thank you from the bottom of my heart.

III. Author's declaration

I hereby declare that the research contained in this thesis has not been submitted for any other prize and is my own work. I also confirm that this work fully acknowledges the opinions, ideas and contributions of other individuals/works.

Signature:

Rana Al-Dujele

IV. Publications work

Journal articles

- Al-Dujele R, Cashell KA, Afshan S., 2018. Flexural behaviour of concrete filled tubular flange girders. Journal of Constructional Steel Research; 151:263-79.
- Al-Dujele R, Cashell KA. Behaviour of concrete-filled tubular flange girders under combined loading. Engineering Structures Journal, Elsevier (Under review)
- Al-Dujele R, Cashell KA. Study on the flexural behaviour of concrete filled rectangular flange girders (CFRFGs). In Structures Journal, Elsevier (Under review)

Conference papers

- Al-Dujele R, Cashell KA., Afshan S., 2017. Ultimate behaviour of concrete filled tubular flange girders (CFTFGs). Poster conference, Brunel University London, UK.
- Al-Dujele R, Cashell KA., Afshan S., 2018. Numerical analysis of the flexural behaviour of concrete-filled rectangular flange girders. Proceedings of 20th International Conference on Civil, Structural and Construction Engineering (ICCSCE), Paris, pp. 913-917.
- Al-Dujele R, Cashell KA., Afshan S., 2018. Ultimate behaviour of concrete filled tubular flange girders. Proceedings of 20th young researcher conference (YRC), UK.
- Al-Dujele R, Cashell KA., 2018. An extended evaluation for flexural behaviour of concrete-filled rectangular flange girders. Proceedings of 9th International Conference on Advances in Steel Structures (ICASS), Hong Kong, China.
- Al-Dujele R, Cashell KA., 2019. The effects of axial tension on the sagging-moment regions of concrete-filled tubular flange girders. Proceedings of 9th International Conference on Steel and Aluminium Structures (ICSAS), Bradford, UK.
- Al-Dujele R, Cashell KA., 2019. Flexural behaviour of concrete-filled rectangular flange girders (CFRFGs). Proceedings of 21th young researcher conference (YRC), UK.
- Al-Dujele R, Cashell KA., 2019. Flexural behaviour of concrete filled tubular flange girders (CFTFGs). First Annual Research Students Conference, Brunel University London, UK.
- Al-Dujele R, Cashell KA., 2020. The effects of axial tension on the sagging-moment regions of rectangular concrete filled tubular flange girders (RCFTFGs). 9th International Eurosteel conference, Sheffield University, UK.

V. Table of Contents

VI. List of figures

VII. List of tables

VIII. Nomenclature

Roman letters	
a	Distance between the simple support and the vertical force
A_s	Cross-sectional area of the steel
B_{Bf}	Width of the bottom flange in RCFTFGs
b_f	Width of the bottom flange in CCFTFG
B_{Tf}	Width of the rectangular tube
d_c	The compressive damage parameter
D_f	Depth of the rectangular tube
d_t	The tensile damage parameter
D_{tube}	Outer diameter of the tube
e	Eccentricity between the location of the axial load and the PNA
E_c	Modulus of elasticity of concrete
E_s	Modulus of elasticity of structural steel
f_c	Uniaxial compressive cylinder strength of unconfined concrete at 28 days
f_{cc}	Uniaxial compressive cylinder strength of confined concrete at 28 days
fl	Confining pressure
f_s	The stress in the steel section
f_t	The tensile strength of concrete
f_u	Ultimate strength of structural steel
f_y	Yield strength of structural steel
h_w	Web depth
L	Member length
M	Moment after equilibrium.
M_u	Ultimate bending capacity of a CFTFG in pure flexure
$M_{u,Exp}$, $M_{u,Calc}$ and $M_{u,FE}$	The experimental, calculated and FE ultimate moment capacity, respectively
N	Horizontal axial force
N_u	Ultimate axial strength of the steel section
P	Vertical force
$P_{u,Exp}$, $P_{u,FE}$	Ultimate experimental and FE load, respectively
R	Outer radius of the steel tube
r	Inner radius of the steel tube
t_{beam}	Thickness of the steel section
t_f	Thickness of the bottom flange
$t_{stiffener}$	Stiffener thickness
t_t	Tube thickness
t_w	Web thickness
u_x, u_y and u_z	Displacements about the global x, y and z axes, respectively
x_0, y_0	Center of the circular tube
y_1	Predicting the location of the PNA from the top of the girder
y_2	The vertical height of the triangular stress block
Greek letters	
ε	Strain
ε_c	Unconfined concrete strain at peak stress
ε_{cc}	Confined concrete strain at peak stress
ε_{eng}	Engineering strain

ε_{true}	True strain
ε_u	Strain at the ultimate tensile stress
ε_{st}	Strain at the onset of strain hardening
ε_y	The yield strain
ε_s	The strain in the steel section
ε_t	Strain for concrete in tension
ε_{cr}	The strain at tensile cracking
ε_{end}	Total tensile strain at the end
σ	Stress
σ_c	Uniaxial compression yield stress of concrete
σ_t	Stress for concrete in tension
σ_{eng}	Engineering stress
σ_{true}	True stress
θ_x, θ_y and θ_z	Rotations about the global x, y and z axes, respectively
$\bar{\lambda}_w$	Web slenderness value
γ_c	The strength reduction factor proposed by Liang (2009)
β_c	A constant which accounts for the confinement effect on the concrete ductility

List of Abbreviations

BASP	The finite element programme stands for Buckling Analysis of Stiffened Plates
CCFTFG	Circular concrete filled tubular flange girder
CDP	The concrete damage plasticity
CFST	Concrete-filled steel tubes
CFTF	Concrete filled tubular flange
CFTFGs	Concrete-filled tubular flange girders.
CHTFG	Compression hollow tubular flange girder
DP	The drucker-prager
FE	Finite element
HFB	Hollow flange beam
HSS	High strength steel
HTF	Hollow tubular flange
HTFG	Hollow tubular flange girder
IGs	Steel I-girders
LDB	Lateral–distortional buckling
LSBs	LiteSteel beams
LTB	Lateral torsional buckling
PNA	Plastic neutral axis
RCFTFGs	Rectangular concrete filled tubular flange girders
RDB	Restrained-distortional buckling
r_T	Radius of gyration of the compression flange
SRFGs	Rectangular steel tubular flange girders (without infilled concrete)
STFGs	Circular steel tubular flange girders (without infilled concrete)
TFG	Tubular flange girder
THTFGs	Triangular hollow tubular flange girders
RHTFGs	Rectangular hollow tubular flange girders

Chapter 1 : Introduction

1.1 Background

Steel I-girders (IGs) are very common elements in modern construction and bridge engineering, especially for heavily-loaded applications. They are typically obtained by welding the two flat-plate flanges and flat web plate together. In bridge applications, the height of an I-girder is typically quite large to provide the necessary flexural strength and stiffness. However, for global stability, these large heights can be disadvantageous. Their behaviour depends on the structural response of the plate elements, which are primarily subjected to various loading. Steel design standards (e.g. AISC, 1999) usually define the flexural strength of IGs, based on local buckling and lateral–torsional buckling (LTB) limit conditions. Local buckling is generally described as a mode which involves the deformation of its individual plates without translating the intersection lines of the adjacent plate elements. Local buckling is therefore dependent on the slenderness ratios of the flange and web components. On the other hand, a rigid-body lateral translation and cross-sectional twist are defining features of LTB, which depends on the unbraced length of the member. IG's which are susceptible to LTB can have significantly reduced moment capacities compared with stockier members are girders with more bracing.

Another common failure mode for IGs is through web distortion (Hassanein and Silvestre, 2013), as shown in Fig. 1.1a. This mode of failure is usually referred to as lateral–distortional buckling (LDB) which is due to the concurrent occurrence of (i) high lateral displacements and compressed flange rotation, (ii) low lateral displacement of the tension flange and (iii) web distortion (i.e. transverse bending). If the I-girder is connected to more stiff structural elements such as concrete slabs in composite girders, web distortion becomes even more obvious. In this case, it is referred to as restrained-distortional buckling (RDB), as shown in Fig. 1.1b.

In light of these challenges, and to order to improve the twisting strength of beams with open sections and decrease their sensitivity to lateral–torsional buckling (LTB), a relatively new section has been developed by replacing the flat compression flange with a tubular shape (i.e. a hollow flange). The resulting section is called a tubular flange girder (TFG), or a hollow tubular flange girder (HTFG).

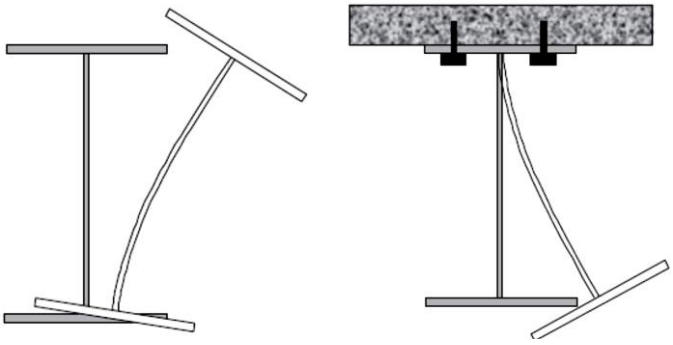

(a) (b)

Fig. 1.1 Steel I-girder (a) LDB (positive bending) and (b) RDB (negative bending)

Fig. 1.2 shows the different types of TFG's which have been developed in recent years for long beams, bridges and other construction applications. One of the main advantages of these girders is that they can support high loads in structural applications which cannot be supported or would be uneconomical using universal rolled sections or built-up I-girders.

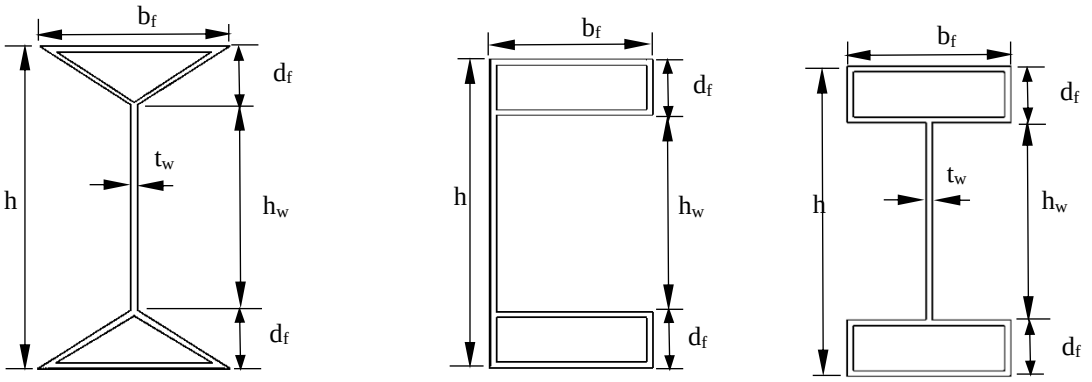

(a) (b) (c)

Fig. 1.2. Hollow flange girders including (a) triangular hollow flange beam, (b) LiteSteel beam and (c) rectangular hollow tubular flange plate girder

Due to its closed section, beams with a hollow tubular flange (HTFGs) have considerably greater local buckling resistance, reduced web slenderness and higher torsional stiffness compared with I-shaped girders of a similar weight (Wassef et al., 1997; Hassanein and Kharoob, 2010; Kharoob, 2017). They also offer higher shear strength and stiffness but remain sensitive to LDB since the minor axis second moment of area of their hollow flanges is slightly increased (Hassanein and Kharoob, 2010; Hassanein and Silvestre, 2013; Hassanein, 2014). However, owing to the relatively thin walls, two typical failure modes can occur, namely web distortion and local buckling (Anapayan et al., 2011a; Hassanein and Silvestre, 2013). Web distortion takes place when the web is quite slender

and can be effectively prevented by using stiffeners along the length (Avery and Mahendran, 1997).

It is clear from the above discussion that HTFGs offer a good alternative to I-shaped girders for heavily loaded applications, although there are some challenges also. Some of these can be overcome by filling the hollow tube with concrete to form a concrete-filled tubular flange girder (CFTFG), as shown in Fig. 1.3. The global stability resulting from combining an I-steel girder with a concrete-filled steel tube (CFST) has been shown to be significantly enhanced through both experimental tests and finite element analyses (Kim and Sause, 2005, 2008; Gao et al., 2014).

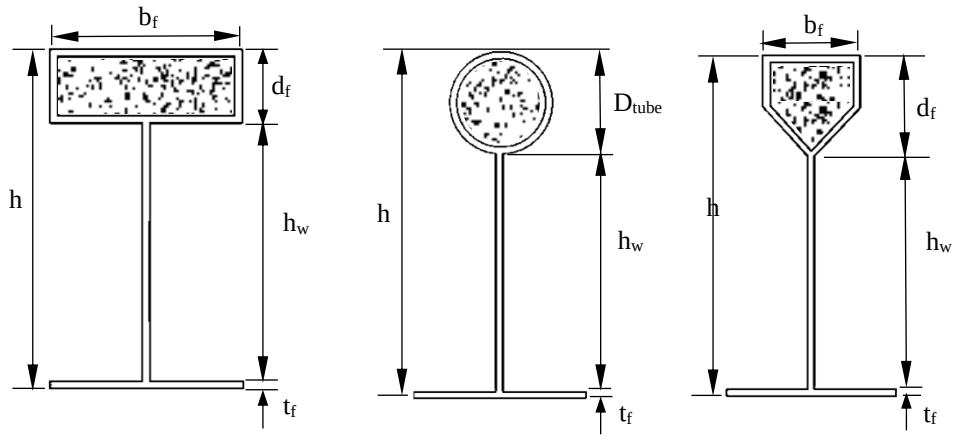

(a) (b) (c)

Fig. 1.3 Girders with concrete filled tubular flanges inlcuding (a) rectangular flange, (b) circular flange and (c) pentagonal flange

1.2 Concrete behaviour in the tubular flange

Composite steel–concrete members are structural systems that embrace the respective qualities of both constituent materials to create an efficient structural solution. Concrete-filled steel tubes (CFSTs) are widely used throughout the world in construction and transportation structures as columns, beams and bridge application. There has been considerable research into CFSTs and they have been shown to offer excellent structural performance, including high strength, good ductility, an attractive appearance, excellent fire resistance and a large capacity to absorb energy (Hu et al., 2003; Han et al., 2007; Giakoumelis and Lam, 2004). In addition, confinement of the concrete core by the steel tube improves the strength of the concrete core and shows different behaviour compared with the normal unconfined concrete. The steel tube provides confining pressure to the

concrete and makes the concrete core under triaxial state of compressive stresses, as shown in Fig. 1.4 (Hu et al., 2003).

This occurs because when the concrete approaches failure, the Poissons ratio of the concrete core is greater than that of the steel tube. The concrete effectively restricts any local buckling of the steel tube and increases the stability and strength of the member as a system whereas the steel tube offers longitudinal and transverse strengthening of the concrete. The natural bond between the tube and the core plays a significant role in transferring the load from the steel tube to the concrete core. A key hypothesis in using CFSTs is that the steel tube and the concrete core work together to resist the applied loads. The steel tube also prevents the concrete core from spalling during fire exposure (Hu et al., 2005, Hu et al., 2003). In light of the many advantages of CFSTs in construction, the addition of a concrete filled tubular flange to a steel girder, creating a concrete filled tubular flange girder, CFTFG) is a promising way of extending the capacity and stability of steel girders such that they can carry very large loads over long spans. Tubular flange girders (TFGs) including hollow (HTFG) and concrete filled (CFTFG) members, are one of several innovative steel beam systems which have been suggested in recent years.

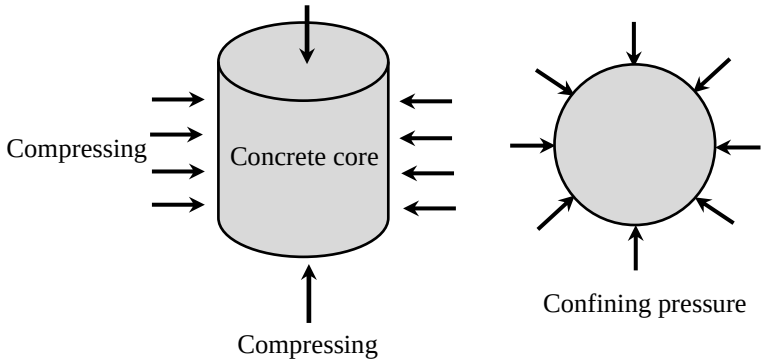

Fig. 1.4 Concrete confined by the steel tube subjected to triaxial compressive stresses (reproduced from Mollazadeh, 2015)

1.3 Types failure modes

Buckling is defined as deformation of the plate elements or members subjected to compressive stresses. When beams exposed to bending action creates tensile and compressive stress on either side of the neutral axis where buckling in the compressive stress region is probable to occur. Local buckling, distortional buckling and lateral torsional buckling are the cross-sectional instabilities of steel beams. Local buckling takes place in short span members, whereas lateral torsional buckling happens in long span

members and distortional buckling mode in intermediate span beams. Fig. 1.5 (a) to (d) show the different modes of buckling failure that take place in channel cross-sections. A brief summery of each types of failure mode as followes

1.3.1 Local buckling

Local buckling involves cross-section distortion, with only rotation occurring at the section's internal fold lines. In a flexural member with HTFG cross section, owing to the nature of thin plate elements, the top flange (tube) is subject to pure compressive stress and is likely to buckle locally. At the same time, the compression portion of the web can buckle because of the compressive stress that caused by bending. Fig. 1.5a show the pattems of local buckling mode of LiteSteel beam (LSB) cross-section purlins under pure bending. On the other hand, CFTFGs do not experience local buckling even at high levels of deflection, due to the confinement effect provided by the concrete core.

1.3.2 Distortional buckling

Distortional buckling is a failure mode which can be found in the compression and flexural members. This type of buckling includes distortion of the cross-section with the incidence of rotation and translation at the inner fold lines. For example, distortional buckling of flexural components like channel section typically involves rotation of the compression flange and lip around the flange-web junction (Fig. 1.5b). This mode is also called (flange distortional buckling). The web undertakes flexure at the equivalent half wavelength as the flange buckle, and the compression flange can slightly translate to the web in a direction normal, even at the identical half-wavelength as the flange and buckling web deformations. Distortional buckling may happen at stresses significantly lower than yield stress, particularly for steels with high strength (Hancock, 2003). The distortional buckling wavelength typically lies between that of local buckling and global buckling.

1.3.3 Lateral distortional buckling

Distortional buckling is also called lateral distortional buckling, where the web bends transversely and the flanges remain either unrotated or to some degree rotated. Fig. 1.5c illustrates lateral distortional buckling of LiteSteel beam (LSB) cross-sections when bending and restraining of the stress flanges.

1.3.4 Lateral torsional buckling

Lateral torsional buckling prevents cross section distortion; but the entire cross section is translated and rotated. Most of the cross-sections generated are mono-symmetric with their shear centre positioned away from their centroid, such as channel sections. A thin-walled beam's shear centre must be loaded through to achieve flexural deformation without twisting. Any eccentricity from the load to this axis can typically cause substantial torsional deformations within a thin-walled plate. Usually beams need torsional restraints either at intervals or continuously such as long span beams demonstrate lateral torsional buckling failure mode. The lateral torsional buckling modes of LiteSteel beam (LSB) cross-section is shown m Fig. 1.5d.

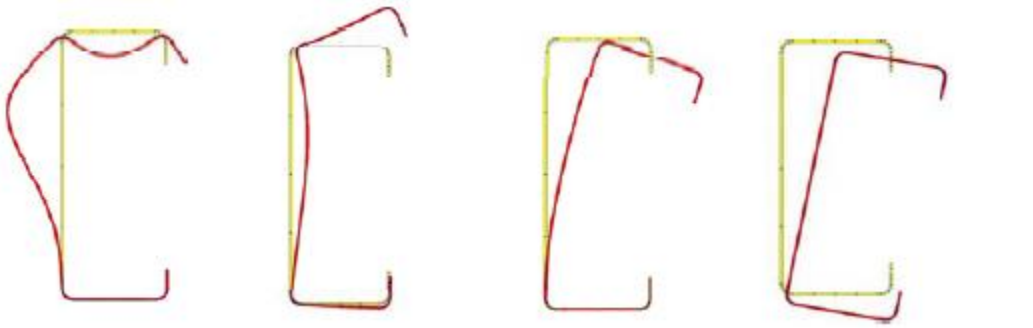

Fig. 1.5 Different buckling modes of LiteSteel beam (LSB) cross-section

1.4 Applications

1.4.1 Hollow tubular flange girder (HTFG)

The applications of structural HTFG sections cover various fields of construction due to their cost efficiency, flexural capacity, ease of connection, large clear spans and availability. Sometimes, HTF sections are used because of the beauty of their shape, to express a lightness or in other cases their geometrical properties determine their use. Although in the past, researchers have investigated different types of HTF beams. They are increasing in popularity not only because of their light weight and efficiency in residential, industrial and commercial buildings, but also because of their beneficial characteristics, including torsionally rigid flanges combined with economical fabrication processes. The investigations on hollow tubular flange (HTF) members in the past were limited to short to medium span applications with a maximum span of 15 m. Since increased torsional rigidity of HTF members is an essential and useful characteristic for long span girders subjected to bending, the advanced architectural designs increase

the demand of innovative steel HTF members with more favourable properties in design of large span applications. In view of long span constructions (Fig. 1.6a) such as bridges. The LiteSteel beam (LSB) sections, another example of HTF, which can be used in a range of construction such as flexural members, truss members and studs, see Fig. 1.6b-e.

(a) Pedestrian bridge in Houdan, France (Wardenier et al., 2002)

(b) Floor Joists (Keerthan, 2010)

(c) Purlins (Anapayan, 2010)

(d) Roof Beams(Keerthan, 2010)

(e) Floor Bearers (Anapayan, 2010)

Fig. 1.6 Applications of HTF sections

1.4.2 Concrete filled tubular flange girder (CFTFG)

There are a number of recent examples of composite bridges, which comprise concrete-filled steel tubes, in different structural arrangements. A number of tubular truss bridges have also been reported (e.g., Lully viaduct in Switzerland (Schumacher et al., 2001)) and also a railway bridge with concrete-filled steel tube girders (Nakamura et al., 2002). Concrete filled steel tubular arch bridges have become widely used around the world in recent decades due to the inherent advantages such as high load-carrying capacity, efficient construction costs and pleasant appearance. As stated before, the concrete prevents the steel tube from buckling locally, whereas the steel tube confines the concrete to resist tension, bending moment and shear force, which increases the load-carrying capacity of the member through the composite structural action of the concrete core and the steel tube. Furthermore, during the construction of the bridge, the steel tube can act as formwork which saves significant building costs (Wu et al., 2006). Fig. 1.7 presents a concrete-filled steel tube arch bridge in China (Zheng and Wang, 2018). In the United States, the Lynch Village Bridge was constructed in 2010 and is one of the earliest examples of a concrete filled tubular flange girder (CFTFG) being used in a bridge, as shown in Fig. 1.8 (NSBA, 2012).

(a)

(b)

Fig. 1.7 Concrete filled steel tube arch bridge (Zheng and Wang, 2018) including (a) Guangxi San'an Yong River Bridge and (b) Hurongxi Expressway Zhijing River Bridge

Fig. 1.8 Lynch Village Bridge (NSBA, 2012) as an example of composite bridges comprising concrete filled tubular flange girders (CFTFGs)

1.5 Methodology

CFTFGs are complex members and their behaviour is governed by a number of inter-related parameters. The analysis of this study is conducted on:

- Two different cross-sections (circular and rectangular CFTFGs)
- Finite element models have been developed using ABAQUS
- Analytical expressions developed suitable for design, based on fundamental principles of structural engineering

1.6 Validation of the numerical modelling

The study required to assess the accuracy of the response predicted by the FE model. Therefore, the model was validated against the test data available. A good agreement is achieved between the experimental and finite element modelling results (e.g. circular and rectangular CFTFG). The overall behaviour is well depicted and the load values are very closely predicted. Therefore, the modelling approach is satisfactory. Using FE results to develop design expressions, based on equilibrium in the section, for moment capacity. The CCFTFG of FE model is developed under different loading conditions and propose the moment–axial force interaction diagram for the design of CFTFGs under combined load.

1.7 Aims of the study

The specific aims of the research are as follows:

- For these types of girder, a specific flexural design formulae in Eurocode 4 (EN 1994-1-1, 2004) is not presented.
- Develop and validate a numerical simulation model for circular and rectangular concrete filled tubular flange girders;
- Study influential parameters (e.g. girder geometry, material strength and initial geometric imperfections)
- Develop analytical expressions which are suitable for design for predicting the bending capacity of CFTFGs;
- The effect that combined axial load and bending moment has on the ultimate capacity of CFTFGs has not yet been covered in a comprehensive way either in the research literature or in codes of practice.
- Eurocode 4 (EN1994-1-1, 2004) provides detailed guidance for the design of composite columns under combined actions, but do not address the effects of combined loading for CFTFGs.
- Study different loading conditions and propose the moment–axial force interaction diagram for the design of CFTFGs under combined load.

1.8 Objectives of the study

The specific aims of the research are as follows:

- The flexural strength of CFTFGs is affected by the contact stresses between the steel tube and concrete infill. The contact stresses increase the compressive strength of the concrete infill by confinement, and decrease the uniaxial yield stress of the steel tube by requiring tensile hoop stresses in the tube.
- Based on a fundamental assessment of the behaviour, it is important to give careful consideration to all factors when designing a CFTFG (e.g. capacity requirements, flange depth, web depth, welding needs, etc).
- The numerical simulations demonstrated that it is important to account for the axial force in the design of CFTFGs which are subjected to combined loading.
- Finally, based on the absence of specific flexural design formulae for the CFTFGs in Eurocode 4 (EN 1994-1-1, 2004), a design model providing suitable ultimate moment capacity values predictions for CFTFGs is presented.

- The final outcome is that CFTFGs provide a viable, efficient and novel solution for heavily loaded structural applications.

1.9 Thesis outline

As well as this introductory chapter, this thesis consists of a further five chapters, as follows:

- Chapter 2 presents a review of the existing information related to this research. General information about concrete filled tubular flange girders including their development, properties, main advantages, and applications are presented and discussed, as well as a thorough review of existing research.
- Chapter 3 presents a detailed description of the development of the finite element model for circular CFTFGs. The numerical simulation model is validated against available test data. Thereafter, it is employed for an extensive numerical parametric study to investigate the behaviour of circular CFTFGs under bending. Also in this chapter, a series of analytical expressions are developed and proposed, based on fundamental structural engineering principles, for calculating the bending moment capacity. The chapter concludes with a comparison between the FE and analytical results.
- Chapter 4 presents the development of a finite element model for simulating the behaviour of circular CFTFGs under combined loading. A detailed discussion is presented on the loading and solution method, boundary conditions, failure criteria, as well as proposals for an appropriate interaction diagram and analytical design equations.
- Chapter 5 presents a detailed description of the numerical modelling of rectangular CFTFGs under bending. The chapter begins with a description of the finite element (FE) model which is validated using the test data available in the literature. This include boundary condition as well as concrete and steel materials information. The validated model is then employed to conduct a parametric study to investigate the effect of key parameters and observe how the cross-section geometry affects the behaviour of tubular flange girders. Based on the analysis, as well as a fundamental assessment of the behaviour, a series of analytical expressions which are suitable for design are presented and assessed for predicting the bending capacity of rectangular concrete filled tubular flange girders

(RCFTFGs). The chapter concludes with a comparison between the FE and analytical results.

- Chapter 6 summarises the main findings of this research study draws conclusions on the main contributions made. Also in this chapter, as series of recommendations for future research is presented.

Chapter 2 : Literature review

2.1 Introduction

The purpose of this chapter is to background and review of the history and basic fundamentals of concrete filled tubular flange girders (CFTFGs). The work and achievements of key researchers in the field are presented and their methods, theories and findings are reviewed. Research in this field in recent years has increased considerably, although the majority of the studies are limited to hollow tubular flange girders (HTFGs) with fewer investigations on CFTFGs.

2.2 Use of CFTFG

A CFTFG is a steel girder which uses a concrete filled hollow structural section top flange. The compression flange (tube) is filled with unreinforced concrete in the manufacture shop after girder fabrication. The concrete in the tube strengthens the hollow structural top flange of the girder. It is worthy to mentioned that the compressive strength of concrete infill contributes to increase the strength of LTB. However, the contribution of the concrete infill for CFTFGs with long unbraced lengths is comparatively low in comparison with the contribution of the concrete infill for CFTFGs with short and intermediate unbraced lengths. Kim and Sause (2005) compared CFTFGs with conventional steel I-beams and also steel–concrete composite beams, these type of girders offer a number of advantages, including:

- Providing more strength, stiffness and stability compared with a conventional steel I-girder, which uses a similar amount of steel or a hollow flange. This is an important benefit under bridge construction conditions before the girders are made composite with a concrete deck (i.e. during construction of the concrete deck);
- The web depth being decreased compared to a steel I-girder of the same total depth, which reduces the web slenderness effects;
- Fewer diaphragms (or cross frames) being required to sustain lateral–torsional stability compared with corresponding steel I-girders, which decreases the fabrication and erection efforts required in bridge constructions;
- Increasing the torsional stiffness, thus improving the lateral torsional buckling (LTB) resistance of the girder.

2.2.1 Manufacturing Process

The manufacturing process for the CFTFG is identical to that for regular tubular parts. The contrast with CFTFG is its special dual weld manufacturing process and its concrete-filled hollow flanges, both patented by Smorgon Steel Tube Mills. Fig. Fig. 2.1 Shows the comparison between single welded tubular sections and dual welds of the LSB.

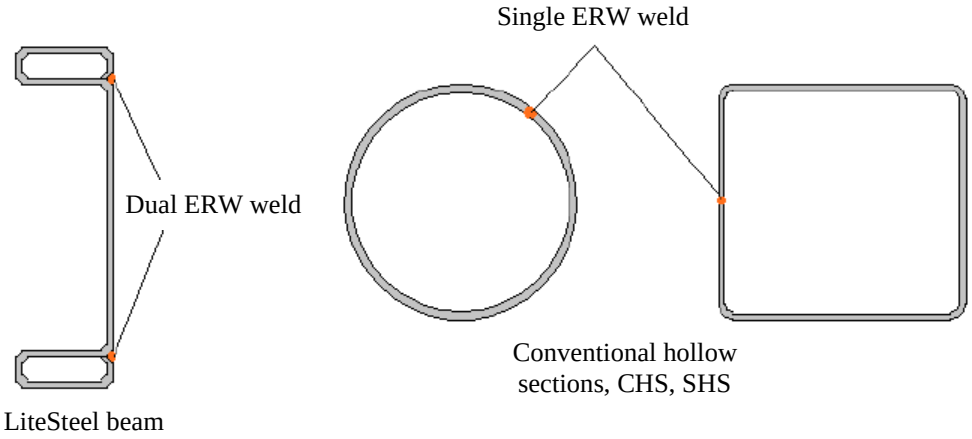

Fig. 2.1 Weld types including, LSB and standard hollow sections

The fabrication process starts by feeding a large sheet steel roll through a series of flattening rollers. The steel is trimmed to the required width, and in a cold forming process the edges are coiled over. This is followed by a full penetration butt weld along the steel length using a dual electric resistance welding (DERW) method. The section is passed through an additional set of rollers that shape and size the section and flanges to its final dimensions. The tube is filled with concrete after girder fabrication. Cleaning and painting are then carried out before bundling and stacking. The manufacturing process is illustrated in Fig. 2.2.

CFTFGs can be most useful when accelerated construction is needed. The use of span-by-span erection and only a few diaphragms increases the speed of erection. This arrangement greatly reduces the demands on the negative moment region at the pier.

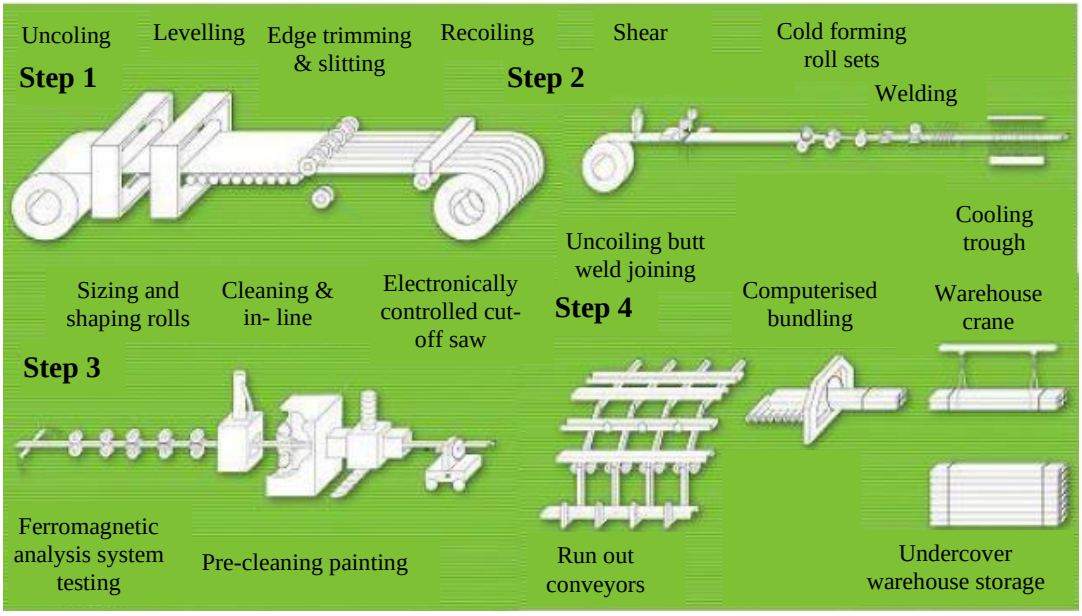

Fig. 2.2 CFTFG manufacturing process

2.2.2 Installation and splice at pier

In CFTFG bridge, preliminary design (Kim and Sause 2008) suggested the use of simple spans for dead load made continuous for the effects of live and superimposed dead load. This was done in anticipation that when accelerated construction is needed. Use span-by-span erection, with just a few diaphragms, increases erection speed. This system significantly decreases the demands on a negative moment area at the pier. The design approach at the pier location is that as simple spans the CFTFGs resist dead loads from CFTFGs and concrete deck. The CFTFGs are then spliced up and made continuous for dead and live superimposed loads. In the deck, the longitudinal reinforcing steel was designed to withstand the stress forces at the pier resulting from the negative moment of bending. The bottom flange resists the forces of compression from negative bending. Owing to the size of the deck reinforcement steel to withstand the negative bending tension forces, tension stresses in the tube are very low and tube resistant, neglecting the infill concrete. In negative bending the advantages sited for the CFTFGs are lost. The CTFTGs return to simply acting as a plate girder with no support from the concrete tube filled in.

The bearing stiffeners are placed outside the splice area to serve as contact plates for the near-pier end diaphragms. On the other hand, the bearing stiffeners at the end diaphragm locations were required for the LTB resistance (Kim and Sause, 2005) . The requirement for a hand-hole in the tube was eliminated by specifying high strength steel bolts with the

appropriate bolt grip through the whole hollow structural section top flange. A wide tolerance in the distance between the girder ends as well as field drilling on one side of the splice was defined to account for field conditions which may deviate from calculation. In the manufacturing shop the tube was filled with concrete on the shop-drilled side of the splice. Greased bolts were put in the holes of the bolts and then removed after cured concrete. In the fabrication shop, the tube at the splice's field-drilled region was not filled with concrete. This area was grouted in the field after bolting up the splice. It is worthy to mention that the tube was filled with concrete in the shop.

It should be observed that the sole plate on the bearing at the pier was welded to the splice plate on the bottom flange. Because of this, the splice bolt spacing at the bottom flange meets the specifications of AASHTO sealing. The sealing criteria have been relaxed because the splices are well protected against moisture and have a painted weathering steel corrosion safety system.

2.2.3 Constructability-erection

Post-tensioned deck slabs precast together with CFTFGs form a well-suited framework system for accelerated construction. However, in the final design process of the CFTFG bridge, further considerations have removed the use of precast deck panels to simplify the design, Fig. 2.3 shows the deck panels before and after concrete was cast, respectively.

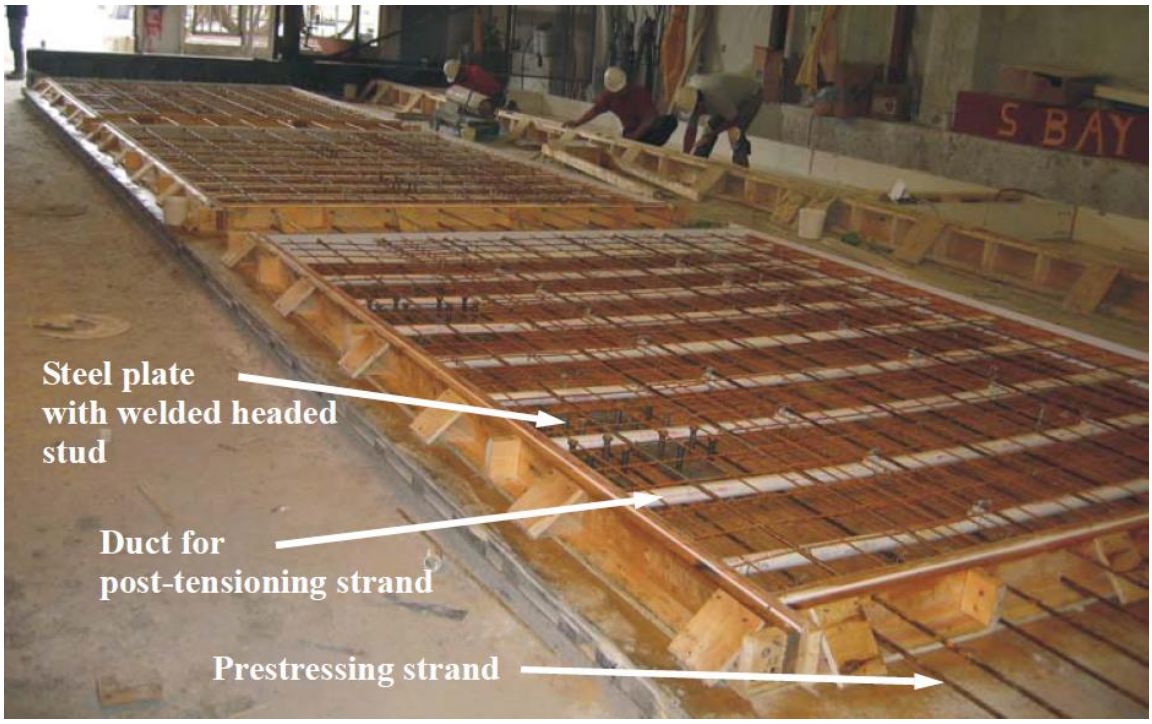

Fig. 2.3 Precast concrete deck panels before casting concrete (Kim and Sause, 2005)

A conventional reinforced concrete deck with cast-in-place was used. When the reinforced concrete deck had been placed, continuity with the bolted splice was created at the pier. The external, fascia CFTFGs are subjected to torisonal loading during deck installation, unlike the preliminary design utilising precast deck panels. For conventional steel plate I-girders, the torsional loading creates major flange lateral bending stresses.

For this purpose, a thorough erection study was performed to verify the deck placement's constructability.

The substructures were designed in standard fashion. On permanent abutment bearings, the girders were erected, and a temporary erection bearing supported by pier brackets. Since the girders were set as simple spans, significant rotation was experienced at the supports. After the deck was placed, the permanent bearings were reset at the far abutment and the girders rotated to their final location. Using an integral abutment at the other end of the bridge will remove the need to reset the bearings at that position, The safety supports involved of concrete and steel beams as shown in Fig. 2.4..

Fig. 2.4 Safety supports (Kim and Sause, 2005)

Subsequently, the bridge deck was placed in the positive moment regions as a simple span bridge, except for the blockout regions at the pier and abutments. A region of blockout was given directly over the splice region to allow the girders to splice after the rest of the deck cured. At each abutment blockouts were provided because an integral abutment was at one end and a concrete diaphragm of full depth was at the other end. However, as the girder deflected from its cambered location it technically assumed the form of the grade

of the profile, the bolt holes on one side of the splice were only sub-punched in the shop and then reamed in the field before making the contact to compensate for camber inaccuracies. The splice of the girder was then made at the pier, leaving out several rows of bolts from the bottom splice plates. The girders were raised with hydraulic jacks placed on the brackets of the erection. The temporary bearings were removed, and the CFTFG's on the final bearings were brought to rest. All girders were raised at the same time and there would be no undue tension in the diaphragms or the wall (Wimer, 2004).

Finally, the remaining bolts were placed in the splice of the bottom flange. The anchor bolts were swedged and installed in the pier cap and grouted into preformed holes. The temporary brackets on erection have been removed. The splice was then grouted to the field- drilled side. After that, the blockout regions of the deck were placed. The contractor was allowed to build the blockout region at the pier using removable deck shapes to allow access from the top of the deck to the work area around the splice. For potential replacement of the bearing the temporary sole plates near the pier were left in place. The holes in the pier cap were then grouted for the temporary erection braces.

2.3 Overview of concrete filled steel tubes (CFSTs)

A composite steel-concrete design can provide an effective structural solution through the use of both component materials in order to create a single composite section. The high tensile strength and ductility of steel in combination with the excellent strength of and robustness of concrete results in an efficient composite cross-section suitable for various applications. Because of these credentials, in recent decades the market share of composite construction has increased dramatically (Vasdravellis et al., 2012a).

A variety of composite members provided with a range of different arrangements have been devised, including composite beams in which a steel section is attached to a concrete slab through shear connectors, and also steel tubes filled with concrete (CFST), which are commonly used for beams as well as columns. CFSTs present a widely versatile application and is an excellent solution to incorporate into structures. These solutions have been used in the design and construction of large buildings and bridges, because of their high axial load-bearing capacity and competitive cost/efficiency ratio.

Fig. 2.5 (a) shows the most widely used cross section shapes in CFST systems, which are circular, square and rectangular (Kovac, 2010). Moreover, some researchers have carried out studies on the behaviour of elliptical sections (Lam and Testo, 2011; Dai and Lam, 2010), while others have examined an innovative X section (Chen and Jin, 2010). For

architectural reasons, the round ended rectangular and polygon cross section forms are used (Han et al., 2014), as shown in Fig. 2.5 (b). When the concrete filled steel tube is exposed to axial compression, a gap occurs between the steel tube and the concrete core in the elastic range because Poisson's ratio for the concrete is smaller than that of the steel tube. Beyond the elastic range, the inner concrete dilates (strains transversely) at a higher/faster rate than the steel tube, hence making contact between the steel tube and the concrete to develop again (Shanmugam and Lakshmi, 2001; Susantha et al., 2001). As the axial compressive stress increases further, continued dilation of the concrete core is restricted by the steel tube, generating a variable confining pressure in the concrete in the transverse direction. This confining pressure effectively increases the compressive strength of the concrete core. In a CFST, the concrete is confined by steel tube section, which results in increased ductility and strength of the concrete core, compared to unconfined concrete (Knowles and Park, 1969; Shanmugam and Lakshmi, 2001; Susantha et al., 2001; Kovac, 2010), as shown in Fig. 2.6.

The ultimate load of a CFST is larger than the sum of loads which can be achieved by independent loading of concrete and steel (Susantha et al., 2001). Fig. 2.7 demonstrates in a schematic way the failure modes of each part individually a steel tube, a concrete core and of a CFST section in compression. In economic terms, a steel tube is used as formwork, for this reduces the manpower, time and constructions costs. Generally, because of the high confinement offered by the circular tube, the post yield and stiffness for the circular sections is greater than that with square and rectangular tubes. The confinement in the rectangular and square sections is limited, being located around the corners and centre, as the straight parts of these sections are too weak to resist the internal pressures, because of the dilation of the concrete core (Shams and Saadeghvaziri, 1997; Schneider, 1998; Huang et al., 2002; Hu et al., 2003; Kovac, 2010). Fig. 2.8 demonstrates the difference between circular and square sections in the confining effect, where local buckling is less likely to take place due to a strong confinement effect in the circular section (Hu et al., 2005).

In order to simulate the behaviour of the confined concrete core, Mander et al. (1988) developed a theoretical stress-strain model for confined concrete and implemented it using the concrete damage plasticity. To simulate steel behaviour, an elastic-plastic response was assumed. Tests revealed that strength development from confinement and the slope of the descending branch of the concrete stress-strain curve have a significant effect on the flexural strength and ductility of reinforced concrete columns. The

theoretical stress-strain model, as shown in Fig. 2.9, was adopted by Mander et al. (1988). Other researchers, such as Ellobody and Young (2006), Ellobody et al. (2006), and Dai and Lam (2010) studied the behaviour of circular, square and elliptical concrete filled steel tubes. Generally, the numerical models have been successful in predicting the compressive behaviour of concrete filled steel tubes with various cross-sectional forms.

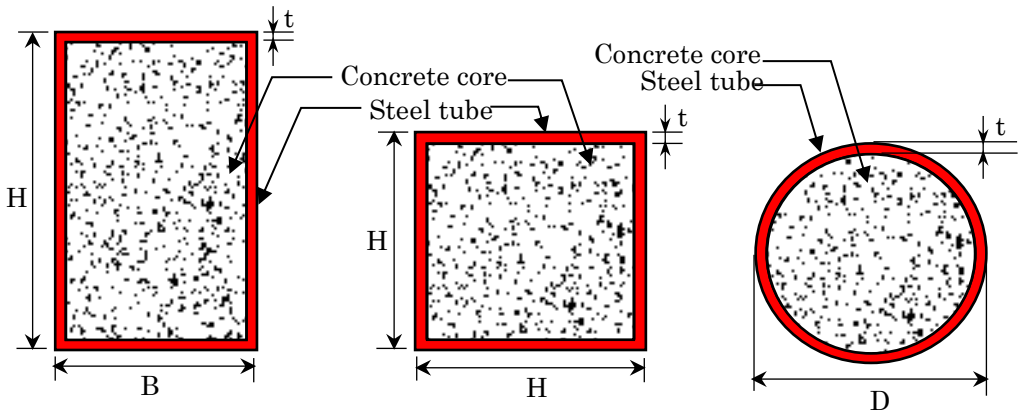

(a) The most widely used cross section shapes

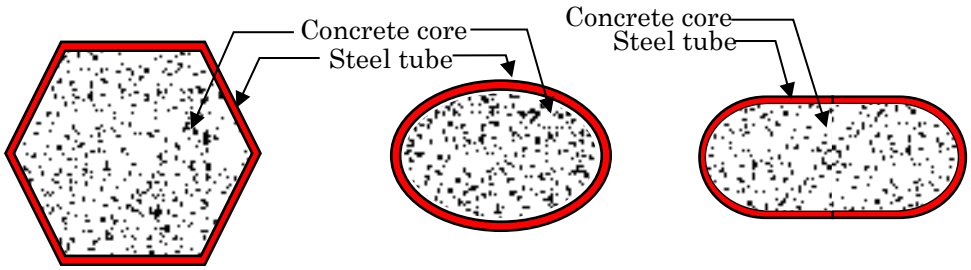

(b) Rarely used cross section shapes

Fig. 2.5 Typical cross section shapes for CFST columns (Han et al., 2014)

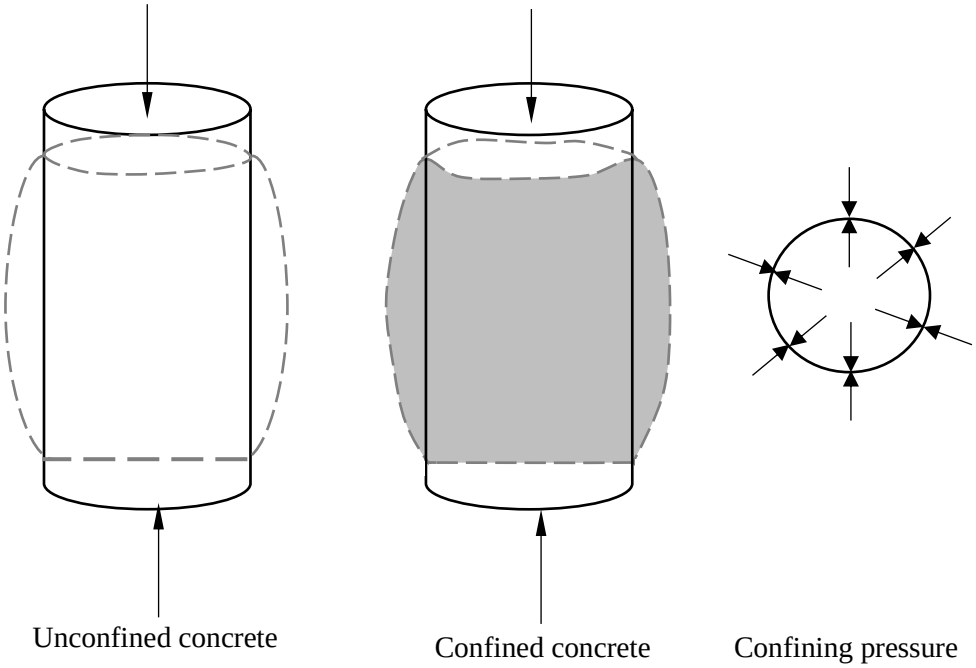

Fig. 2.6 Confining pressure engaged by the dilation of concrete (Harries and Kharel, 2003)

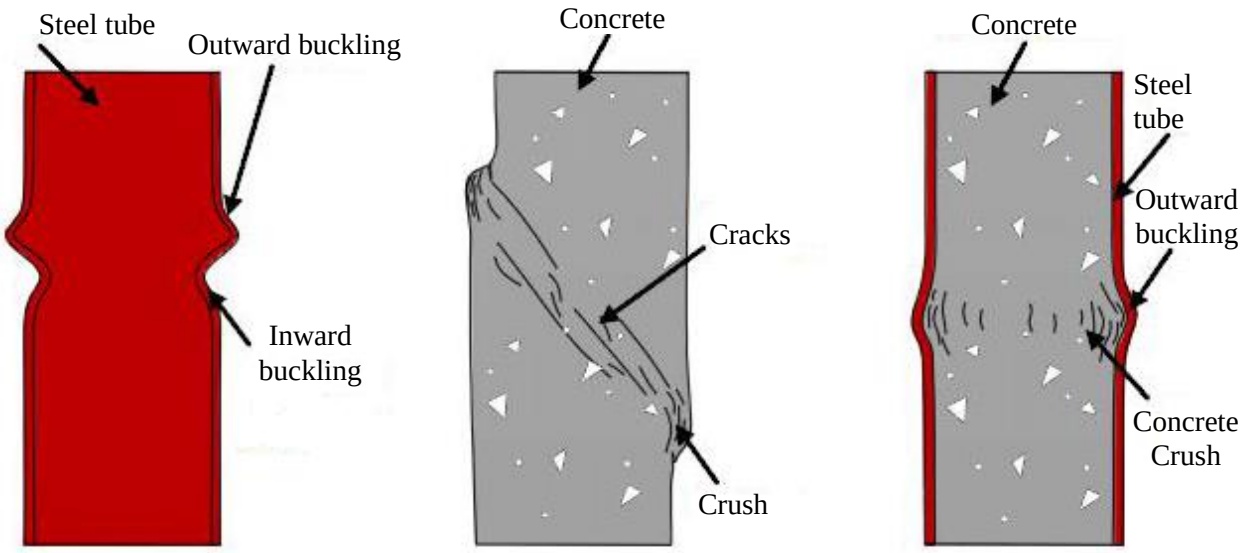

Fig. 2.7 Schematic failure modes of a steel tube, concrete and CFST

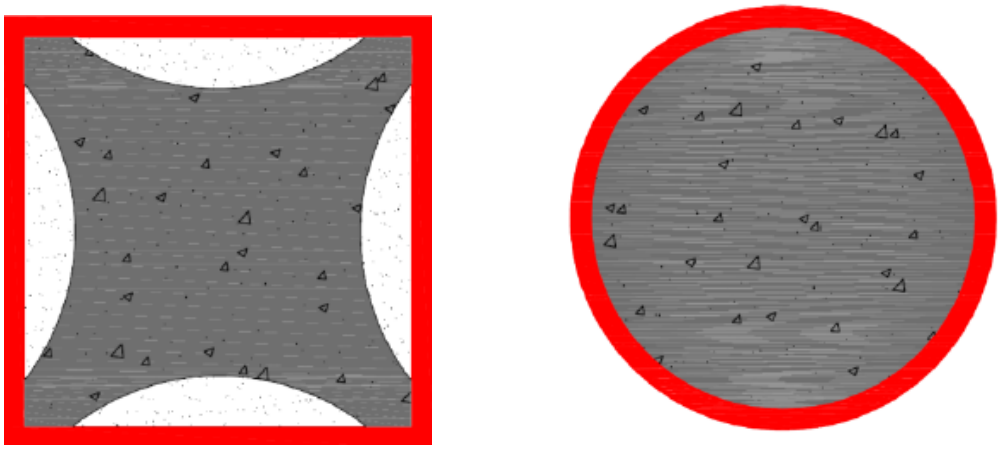

(a) Partial confinement (b) Full confinement

Fig. 2.8 The confinement effect in circular and square sections (De Oliveira et al., 2009)

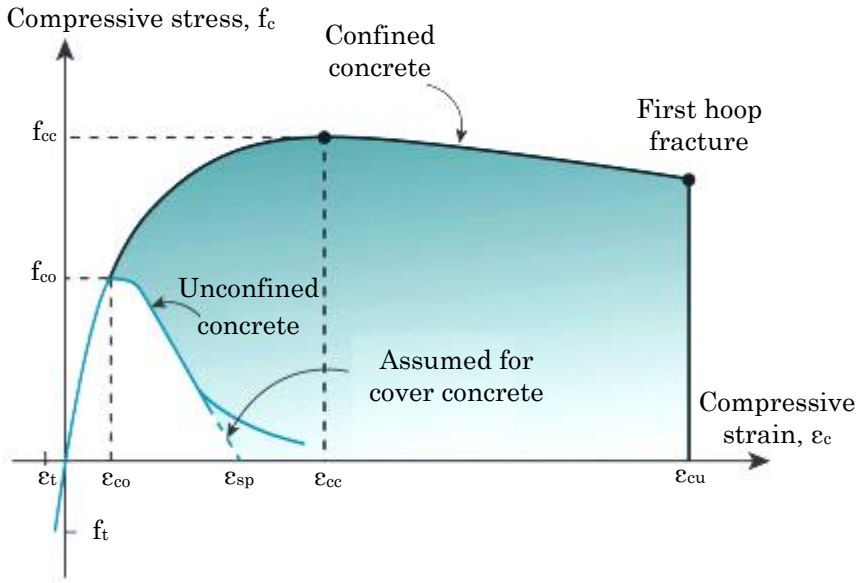

Fig. 2.9 Mander's model for confined concrete (Mander et al., 1988)

2.4 Tubular flange girders (TFGs)

The advances in the technology of structure and construction also led to the improvement of the flange tubular girders, with a primary goal of increasing their lateral-torsional buckling. A design engineer should ensure that the designed element is safe in various possible modes of failure. The earlier studies included theoretical, analytical, and experimental research. TFGs for straight as well as curve bridges have been considered, including hollow and filled concrete. For straight girder bridges, the great torsional

stiffness of a tubular flange girder (TFG) results in considerably larger lateral–torsional buckling strength in a comparison with corresponding I-girder. For horizontally curved girder bridges, the great torsional stiffness of a TFG results in less total normal stress, vertical displacement and cross-sectional rotation compared with corresponding I-girder (Sause, 2015).

2.4.1 Hollow tubular flange girders (HTFGs)

Since the early 1990s, hollow tubular flange girders (HTFGs) for structures and bridges have been developed. The flanged beams of the I-section are not stiff torsionally and therefore, web distortion will not be important unless the web is particularly slender or when only the tension flange is torsionally restrained. On the other hand, the webs are relatively flexible with hollow tubular flanges, hence enabling the effects of web distortion to decrease their resistance to flexural-torsional buckling. Based on the torsional rigid closed flanges in combination with economical fabrication processes, the structural efficiency of these hollow flange sections was the basis for their improvement (Dempsey, 1990). These girders were primarily designed to bear high loads that universal-rolled sections and built-up I-steel girders cannot support or when they are uneconomical.

The history of the hollow flange beam (HFB) can be traced back to 1965, when O' Connor et al. (1965) first demonstrated how the inclusion of several closed cells on I-steel beams improved their buckling behaviour considerably (see Fig. 2.10). The enhancement in buckling behaviour was primarily due to an increase in torsional rigidity. However, the studies did not take into consideration the feasibility of mass scale for practical applications of this type of HFB.

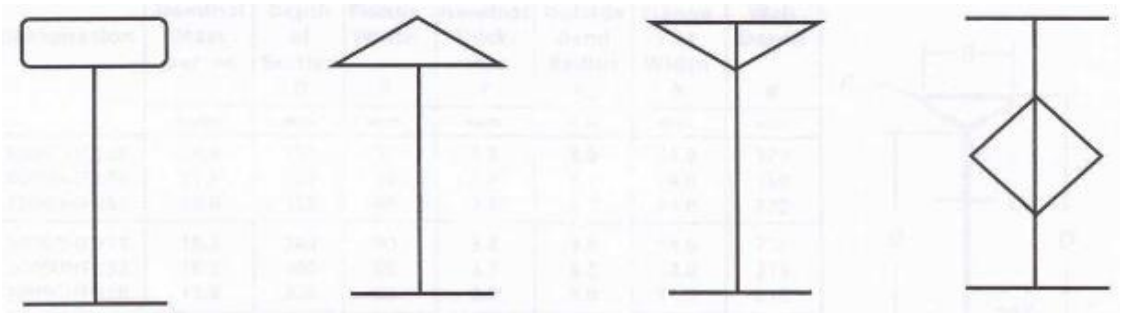

Fig. 2.10 Closed-cell section types investigated by O’Connor et al. (1965)

2.4.1.1 Triangular hollow tubular flange girders (THTFGs)

Throughout the 1990s, Palmer Tube Mills Pty Ltd of Australia extended the creativity to the mass production of cold-formed, high-strength steel sections with two closed triangle hollow flanges, as shown in Fig. 2.11. This product was unique, being the first hollow flange section anywhere in the world. The triangle is manufactured from a single strip of high strength steel using electric resistance welding. The design efficiency of the hollow flange was as a result of the torsionally rigid closed triangular flanges combined with economical fabrication processes, which was the basis of the hollow tubular flange development (Keerthan, 2010).

However, only one group of 90 mm THTFGs was capable of being produced and other flange widths were not manufactured using the existing equipment. Also, it was found that the electric welding process was somewhat expensive for the manufacturers. The use of THTFGs would significantly develop the structural efficiency, whereas eliminating or delaying several undesirable buckling modes and, as a result, production was discontinued in 1997. Fig. 2.10 (a) and (b) show the typical cross-section and an isometric view of a THTFG respectively, while Table 2.1 presents its details. This double-symmetrical section was used as both compression and flexural members (Anapayan, 2010).

Nevertheless, one study has found that the flexural capacity of THTFGs is limited under certain restraint, span and loading conditions by the lateral distortional buckling mode of failure, as shown in Fig. 2.12 (Anapayan, 2010). Unlike the frequently observed lateral torsional buckling of steel beams, the lateral distortional buckling of THTFGs is defined by simultaneous lateral deflection, twist and cross-sectional change owing to web distortion, as seen in Fig. 2.12. The cross-sectional distortion causes considerable reduction in strength and is particularly severe in intermediate spans. Several researchers have studied the effect of web stiffeners on the buckling strength. Pi and Trahair (1997a, 1997b) improved upon pioneering studies into the lateral-distortional buckling of the tirangular girder where a simple expression was suggested to explain the effect of web distortion on the flexural strength when these members were subjected to uniform bending. Nevertheless, their research was limited to analytical studies using assumed residual stresses as well as geometric imperfections.

Avery and Mahendran (1997), using finite-element (FE) analyses of stiffened and unstiffened hollow flange beams (HFBs), investigated the effects of various parameters,

such as thickness and location of web stiffeners on the lateral-distortional buckling behaviour of HFBs. The findings show that the use of transverse web plate stiffeners significantly improves the LTB strength of beams. Avery et al. (2000) carried out research on the flexural capacity of cold-formed HFBs subjected to pure bending, considering web lateral distortional buckling using the finite element method.

(a) Cross-sectional view (b) Isometric view

Fig. 2.11 Geometry of triangle (HTFs) (Dempsey, 1990)

Table 2.1 Geometry of THTFGs (Anapayan, 2010)

Designation	Nominal mass per m	Depth of section	Flange width	Nominal thickness	Outside bend radius	Flange flat width	Web depth
		D	B	t	R_o	b	d
	kg/m	mm	mm	mm	mm	mm	mm
45090HFB38	23.0	450	90	3.8	8.0	74.0	370
40090HFB38	21.5	400	90	3.8	8.0	74.0	320
35090HFB38	20.0	350	90	3.8	8.0	74.0	270
30090HFB38	18.5	300	90	3.8	8.0	74.0	220
30090HFB33	16.2	300	90	3.3	8.0	74.0	219
30090HFB28	13.8	300	90	2.8	8.0	74.0	218
25090HFB28	12.7	250	90	2.8	8.0	74.0	168
25090HFB23	10.5	250	90	2.3	8.0	74.0	168
20090HFB28	11.6	200	90	2.8	8.0	74.0	118
20090HFB23	9.6	200	90	2.3	8.0	74.0	118

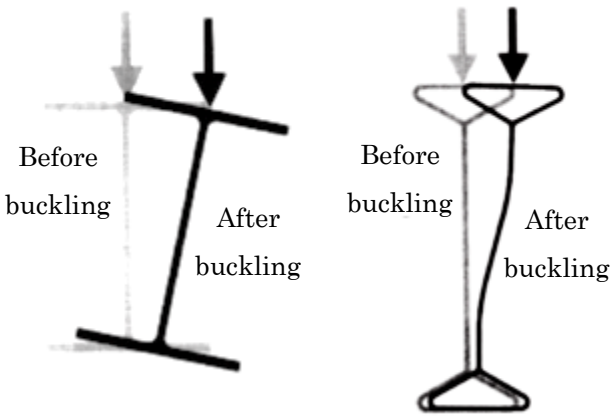

Fig. 2.12 Lateral torsional and lateral distortional buckling modes

Cuong et al. (2016) studied the mono-symmetrical I-beam with a hollow flange, as shown in Fig 2.13a, pointing out that its critical moment of lateral torsional buckling is considerably greater than for the ordinary I-beam, which has almost similar cross-sectional dimensions. Welding delta stiffeners in a THTFG between the compression flange and the web plates increases their torsional stiffness and the LTB moment resistance of the original beam, as shown in Fig. 2.13b. The use of delta stiffeners not only improves the global LTB resistance of the beams, but also delays premature local buckling of their slender constituent plates (compression flange and web plates) in non-compact and slender sections (Mohebkhah and Azandarariani, 2015).

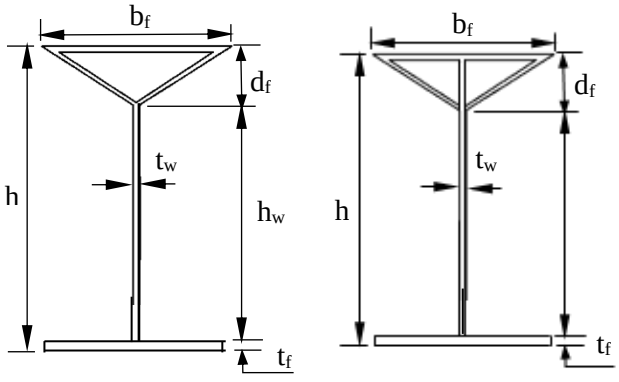

Fig. 2.13 A typical delta hollow flange beam

2.4.1.2 LiteSteel Beams (LSBs)

LiteSteel beams (LSBs), another kind of hollow tubular flange (HTF), have also been developed and studied in recent years. They are typically produced from cold-formed steel, with a channel form comprising two closed rectangular hollow tubular flanges and

a slender web, as illustrated in Fig. 2.14 (Anapayan, 2010). An LSB has a unique mono-symmetric shape, which can be potentially used for a wide range of applications, such as flexural members in residential, commercial and industrial constructions. Many experimental and numerical studies have been conducted on the structural behaviour and design of LSBs at Queensland University of Technology in Australia. These studies have been aimed at determining the section moment capacities when they are subjected to lateral distortional and lateral torsional buckling (Anapayan et al., 2011a), the pure moment capacities (Anapayan et al., 2011b; Anapayan and Mahendran, 2012) and finally, the shear capacities (Keerthan and Mahendran, 2011; Keerthan et al., 2014).

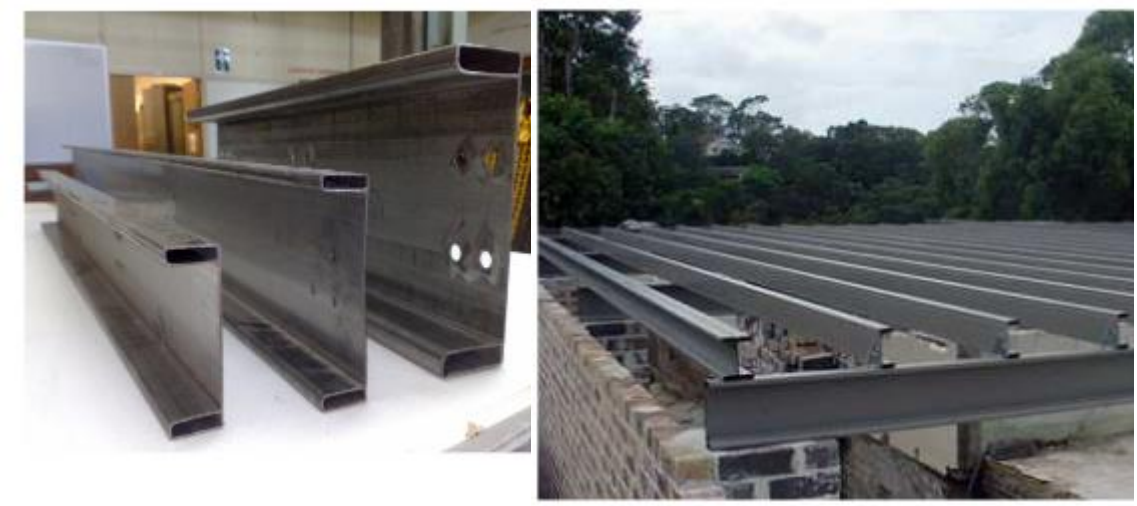

Fig. 2.14 Typical LSBs (Anapayan, 2010)

This research has considerably enhanced the understanding of the structure behaviour of the LSBs, particularly in flexural applications. There has been a focus on hollow flange channel members, which have been subject to bending action only, so that they were subjected to transverse loads applied at the shear centre, and the torsion of the sections is not possible. Because of its mono-symmetric characteristics, the channel section is also be subjected to torsion when the transverse loads are applied away from the shear centre. Torsion is often ignored, however, because it is commonly considered to be rare and, in any case, is seen as being unimportant when it does occur.

2.4.1.3 Rectangular hollow tubular flange girders (RHTFGs)

The tubular flange girder system that has been suggested and considered as one of the most efficient bridge sections. Straight hollow tubular flange girders (HTFGs) with two rectangular steel tubes for both the compression and tension flanges have been studied by

Dong and Sause (2009a). In this study, the effects of several parameters were investigated including geometric imperfections, residual stresses, cross section dimensions, transverse web stiffeners, and bending moment distribution on the lateral-torsional buckling flexural strength of HTFGs. The results of the FE analysis were used to evaluate the accuracy of the formulas for determining the lateral–torsional buckling flexural strength of HTFGs. The study also demonstrates that the flexural strength of straight HTFGs with intermediate unbraced lengths is significantly affected by the residual stresses. The outcomes of the work were used to validate the flexural strength formulas proposed by Kim and Sause (2005).

RHTFGs with a slender web have also been proposed and investigated by Hassanein and Kharoob (2010, 2012). In this research, homogenous and hybrid RHTFG shear strengths were examined, with hybrid girders being the members, using various web and flange materials, as well as probing the buckling behaviour of sections with slender stiffened or unstiffened transverse webs. After that, Hassanein (2014) examined the effect of square opening sizes on the shear behaviour of RHTFGs. The results of these works (Hassanein, 2014; El-Khoriby et al., 2016) provided two important results: (1) using the HTFGs rather than steel I-girders is a powerful tool that not only improves the shear strength of the girders in the tension field, for it also significantly saves weight; and (2) it offers a high performance solution for a drop in shear capacity owing to the presence of web openings. However, the results of (Hassanein and Kharoob, 2010; Hassanein, 2012) showed that the HTFGs were not entirely compliant with the international steel structures codes, because of their unique forms. This encouraged Hassanein and Silvestre (2013) to examine the lateral–distortional buckling (LDB) of RHTFGs with slender unstiffened webs. The results indicated that using HTFGs (without stiffeners) rather than steel I-girders (with stiffeners) is a very effective tool for improving the flexural strength of the girders. It was observed that RHTFGs are still sensitive to lateral-distortional buckling even with hollow tubular flanges, although they can resist much greater critical loads than conventional steel I-beams.

Furthermore, a compression hollow tubular flange girder (CHTFG), with one rectangular hollow steel tube, has been conducted to investigate the shear strength behaviour by Hassanein and Kharoob (2013). The findings of this investigation indicate that the CHTFGs provide smaller depths, compared to the HTFGs, which are suitable for structures with relatively limited construction depths. As a result, the unacceptably large construction depths of the HTFGs could be reduced by using the CHTFGs. It is worth

pointing out that this benefit (i.e. decreasing the depth of the girder) could be achieved without reducing the radius of gyration of the compression flange required for lateral stability. Kharoob (2017), used a finite-element (FE) investigation to study lateral torsional buckling of simply supported CHTFG subjected to uniform bending. The results revealed that using beams with less slender webs for medium-to-long spans optimises the girders by decreasing their weight. Moreover, increasing the tubular compression flange depth (i.e. increasing the radius of gyration of the compression flange (r_T)) leads to an increase in the bending moment capacity of the CHTFG. Furthermore, increasing (r_T) at the same time as decreasing the web depth reduces fabrication costs by decreasing the weld lengths used for the connections between the stiffeners and webs. HTFG and CHTFG are shown in Fig. 2.15a and 2.15b, respectively.

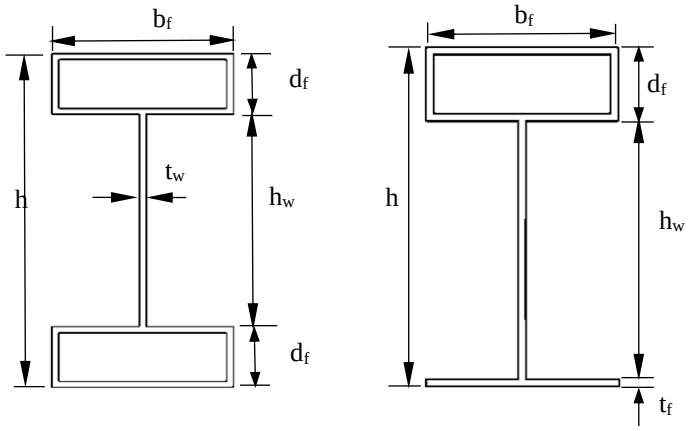

Fig. 2.15 Definition of symbols of typical girders: (a) HTFG and (b) CHTFG

2.4.2 Concrete filled tubular flange girders (CFTFGs)

For hollow flange girders, it has been widely observed that beams with a relatively thin tube thickness are subjected to local buckling of the compression tubular flange, which limits the flexural resistance of the member. To overcome this problem, concrete filled tubular flange girders (CFTFGs) have been suggested and studied by several researchers. The primary benefits of CFTFGs compared with steel I-girders have been outlined by Wassef et al. (1997), which including large local buckling resistance, great torsional stiffness, and reduced web slenderness.

2.4.2.1 Rectangular CFTFGs

Owing to the efficiency of composite construction, and the interesting and promising development of hollow tubular flange plate girders, it was a natural progression to

consider filling the top hollow tube with concrete to create a concrete-filled tubular flange girder (CFTFG). Researchers at Lehigh University in the United States conducted an experimental, numerical and analytical study of the cross-section depicted in Fig. 2.16, and assessed the influence of boundary conditions and diaphragm (or stiffener) arrangement on the structural response (Wimer, 2004). The proposed analytical model was based on a transformed section approach and a good agreement was shown with the experimental and numerical results. Two 18 m long of rectangular concrete filled tubular flange girders (RCFTFGs) with flat and corrugated webs were tested, as depicted in Fig. 2.16. Wimer (2004) investigated the test specimen for two conditions: (1) RCFTFGs that are non-composite with a concrete deck when the lateral-torsional buckling strength controls the flexural capacity, and (2) RCFTFGs that are composite with a concrete deck when the RCFTFG section flexural strength controls the flexural capacity. The girders were scaled down by a 0.45 factor, fabricated and tested to examine their ability to carry their design loads. The advantages of experimental and analytical analysis are as follows:

- Tubular flanges allow for the use of large girder unbraced lengths by improving the torsional stiffness of the girder;
- Corrugated webs generate lighter weight designs compared with unstiffened flat webs since the corrugated web is thinner, although the flanges are slightly greater;
- Because of the increased steel yield stress, hybrid designs produce lighter weight designs compared with homogeneous ones.

Kim and Sause (2008) studied a two-span continuous tubular flange girder demonstration bridge. The steel girder consisted of a web and bottom flange conventional plate, with the top flange fabricated with a rectangular hollow tube that was then infilled with concrete. The results of this study have shown that in terms of construction load conditions, the RCFTFGs designed for the demonstration bridge had enough lateral torsional stability, even with no interior bracing within the span, with the aim of fabrication and erection effort which could be reduced by eliminating diaphragms. Also, it emerged that the precast concrete deck can decrease the time required for construction, compared with a cast-in-place one, by reducing the time needed to place shapes and reinforcing steel as well as eliminating the time required for the concrete to cure.

In investigations on the shear behaviour of RCFTFGs with a corrugated web, Shao and Wang (2016) found from experimental tests that this has greater resistance to buckling, because of its high flexural stiffness. Local buckling can be stopped efficiently, if appropriate dimensions of corrugated web are designated. Based on the experimental

results, it was concluded that RCFTFGs with corrugated webs have both higher load carrying capacity and better ductility compared with a steel I-girder. In addition, the mechanisms for both a conventional steel I-girder and a RCFTFG with a corrugated web were much different when they had a short span and they were subjected primarily to shear action. The conventional steel I-girder is much more sensitive to local buckling of the web as a result of its high slenderness ratio. In contrast, the RCFTFG with a corrugated web behaves much more like a flexural beam, and flexural strength because of yielding is normally dominant.

Fig. 2.16 Straight TFGs with a concrete-filled rectangular steel tube compression flange (Wimer, 2004)

2.4.2.2 Circular CFTFGs

Kim and Sause (2005) examined the performance of straight CFTFGs with a circular concrete filled tube as the top flange, instead of a rectangle, as illustrated in Fig. 2.17. A four girder, simply supported bridge prototype was developed in order to design flexural strength formulas for CFTFGs that take LTB and cross-section yielding into consideration. These equations have been calibrated to finite element (FE) analysis results. The prototype bridge was developed for design criteria in terms of strength, stability, service and fatigue.

Kim and Sause (2005) examined a 0.45-scale test specimen with two straight circular CFTFGs. The test specimen of a circular concrete filled tubular flange girder (CCFTFG), non-composite with a concrete deck, as shown in Fig. 2.17, was tested for two conditions:

(1) construction conditions when flexural capacity is controlled by the LTB strength; and (2) service conditions when the flexural strength is controlled by the CFTFGs' cross-section. A concrete deck, extra concrete and steel blocks were loaded for the test specimen. For the construction conditions, the circular CFTFGs were not braced by the concrete deck, however, for the service ones, this was the case. The experimental results were compared with those for the FE analysis and indicated that the test specimen's behaviour can accurately be estimated by using FE models. Kim and Sause (2005) also suggested formulas to predict the lateral-torsional buckling (LTB) strength of CFTFGs.

Fig 2.18 compares the whole steel girder weight of the composite I-girders, the circular CFTFGs composite with a slab deck, and the circular CFTFGs alone without one. In this figure, the weight of the total steel is compared to either the web depth (for the I-girders) or the web depth plus the tube diameter (for the circular CFTFGs). It should be noted that for all the cases unstiffened web is used. It can be seen in this figure that the circular CFTFG composites with a slab deck, even when a large diaphragm spacing is used, are more than 10% lighter than the composite I-girders. Hence, the circular CFTFGs composite with a slab deck have the advantages of decreased steel weight as well as reduced fabrication and erection effort (i.e. fewer diaphragms).

It was also found that the circular CFTFGs composite with a slab deck are lighter in total girder steel weight than the circular ones alone, i.e. without a slab deck, i.e. non-composite. For the circular CFTFGs without a slab deck, however, less construction effort is needed, whereas the construction effort required to make the circular CFTFGs composite with a slab deck can make their designs less economical. For example, if the girders are designed to be the CFTFGs without a slab deck (non-composite), a precast deck is easier to install. Moreover, in this case, the girders made of 485 MPa steel have an entire girder steel weight 25% more than the total steel weight of the circular CFTFGs made of 690 MPa steel (Kim and Sause, 2005).

Fig. 2.17 Straight CFTFGs with circular steel tube top flange (Kim and Sause, 2005)

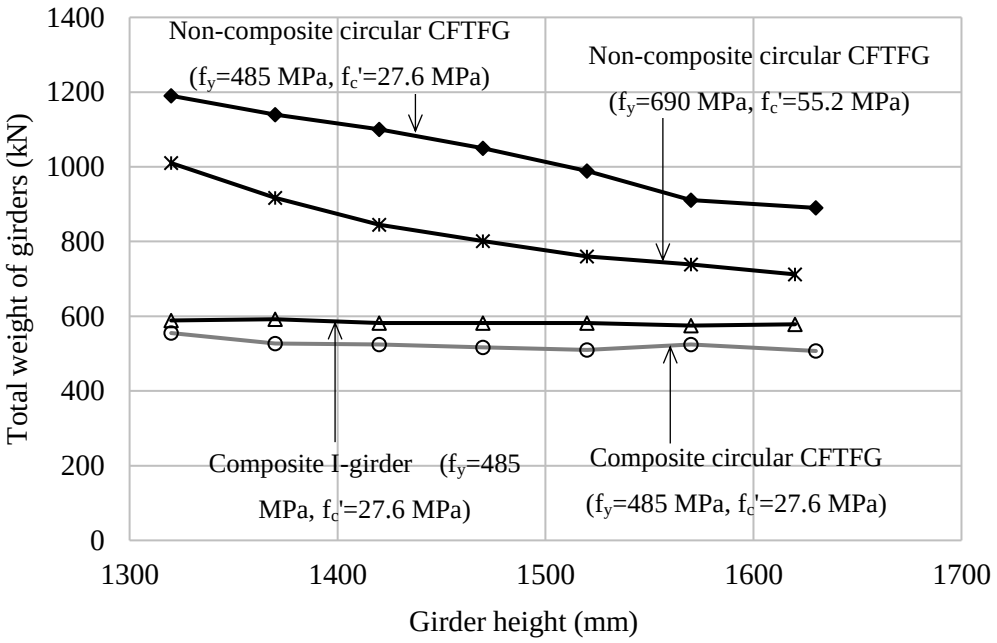

Fig. 2.18 Comparison of I-girders and circular CFTFGs with unstiffened webs (Kim and Sause, 2005)

2.4.2.3 Pentagonal CFTFGs

A new type of CFTFG using a concrete filled pentagonal flange in the girder was presented recently by Gao et al. (2014). This cross-section was fabricated by welding an extra steel plate onto the compression flange of a steel I-girder, which was then filled with concrete, as shown in Fig. 2.19. Gao et al. (2014) studied the flexural behaviour of pentagonal CFTFGs using both experimental and numerical investigation. In the analysis,

it was assumed that the section geometry is identical to that of a rectangular concrete-filled flange, but with a larger flange depth to width ratio in order to reduce the tendency of local buckling occurring in the web.

Hassanein (2015) investigated, using a numerical study, the behaviour of pentagonal CFTFG specimen of Gao et al. (2014) under shear action. The results of this study indicated that a cross-section with the maximum possible inclined depth only is advantageous (economical) and should be used. This is because it improves the ultimate-to-plastic shear ratio of the girder much more than the increase in the cross-sectional area.

Fig. 2.19 Pentagonal CFTFG specimen (Gao et al., 2014)

2.5 Curved TFGs

Curved steel girder highway bridges are usually used at locations where the roadway alignment is constrained. The horizontal curvature causes considerable torsion in the bridge girder system, which is an essential consideration for the design and thus, the behaviour of these bridges is more complicated than that of straight ones. At present, steel I-girders or box-girders are used for curved steel bridges. However, there are potential issues with each of these systems (Ma, 2014). The steel I-girder has an "open" section with very little torsional resistance. First of all, stability during construction is a major challenge. During bridge erection, curved steel I-girders are commonly supported temporarily at intermediate places between piers before the girders are attached to

permanent cross frames (or diaphragms). Because the torsional stresses and displacements can be large, even under self-weight of the girder, owing to the little torsional stiffness of the steel I-girder. As a result, temporary shoring may be required to erect a steel I-girder bridge framing system. Secondly, both the I-girders and the cross-frames have to be designed as main load-carrying members since they work together with girders to resist torsion carried by the bridge system. As curved steel I-girders improve substantial warping stress caused by their low torsional stiffness, many cross frames can be used to reduce the warping stress which may be expensive (Hampe, 2012).

A box-girder is a "closed" section with a relatively large torsional resistance and insignificant warping stress. Because of the great cross-section width and depth of the box-girders, cross-section distortion is an area of concern, which can lead to considerable distortional stresses. In order to maintain the box shape and avoid cross-section distortion, the brace should be used inside the box. The internal bracing inside a box-girder makes box-girder design, construction, and maintenance complex and expensive. Fatigue issues are also a concern for box-girders due to the possible cross-section distortion and the bracing details (Sennah and Kennedy, 2002). As shown in Fig. 2.20, a box-girder cross section can take the shape of a single cell (one box), multiple spine (separate boxes), or multicell with a common bottom flange (contiguous cells or cellular shape).

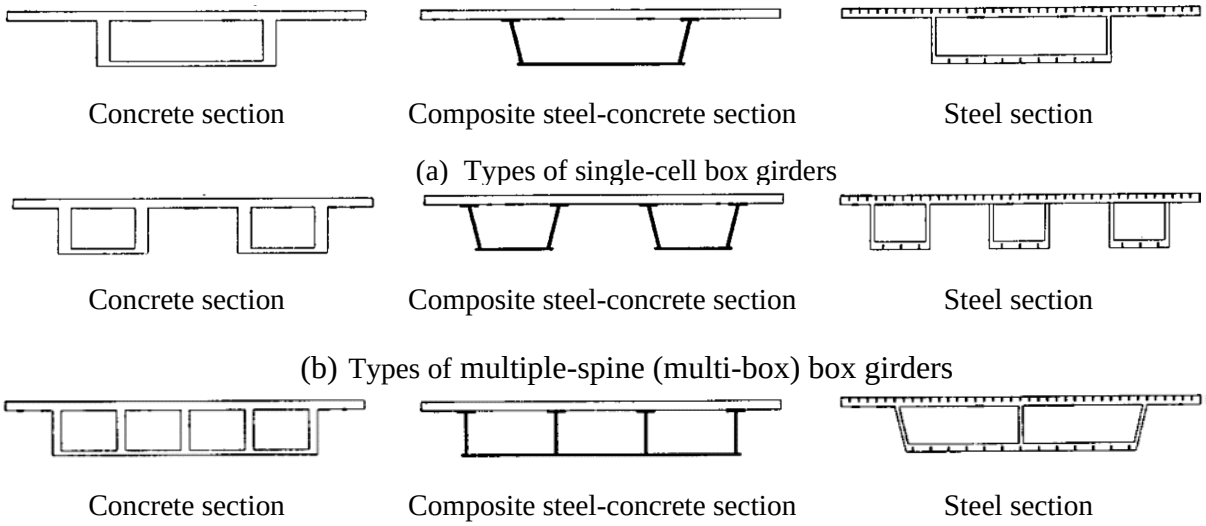

Fig. 2.20 Box girder cross sections (Sennah and Kennedy, 2002)

An extensive number of analytical and experimental studies have been carried out on both curved steel I-girders and box girders. For instance, the nonlinear behaviour of curved steel I-girders was studied by Pi et al. (2000). Under vertical loading, a curved I-girder improves both the main bending and uniform torsional action, with vertical deflections were combined with cross-section rotations. These main activities and deformations combine together to produce second-order bending actions about the minor axis. In steel I-girders with large initial curvatures, the second order effects are important. Formulas for the design of standard curved steel I-girders against combination bending and torsion actions were proposed by Pi and Bradford (2001), as shown in Fig. 2.21. The AASHTO LRFD Bridge Design Specifications (2004) provide standard design guidelines for curved I-girders for highway bridges.

A curved tubular flange girder (TFG) is an innovative curved steel I-girder for highway bridges, which combines the flexural efficient open cross-section of an I-girder with a closed tube as the top flange. The TFG has a circular or rectangular tube shape in place of the compression plate flanges of steel I-girder, whereas its web is similar to that of a conventional I-girder. Due to the torsional stiffness of the tubular flanges, a TFG has considerably more torsional stiffness compared with a steel I-girder and is expected to have less cross-section distortion than a box-girder (Sause, 2015).

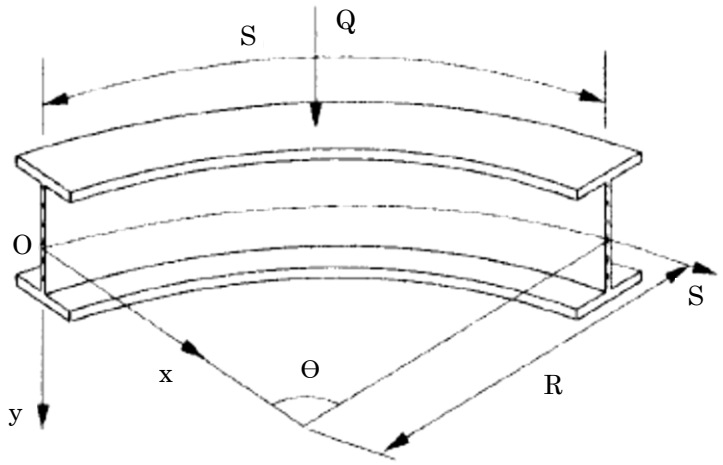

Fig. 2.21 System of curved steel I-girder in Plan (Pi and Bradford, 2001)

Fan (2007) extended the work on single curved girders by Dabrowski (1968) to curved TFGs, with either an open or a closed cross-section. Linear elastic theoretical analysis methods were developed for single curved TFGs and multiple cross-frame curved TFGs. A parametric study of the girder curvature was completed on individual curved TFGs and curved TFG systems. A parametric study was also carried out on the number of cross-

frames in curved TFG systems. The behaviour of curved TFG systems was compared with that of standard curved steel I-girder systems.

In order to compare the behaviour of curved TFGs with corresponding curved I-girder systems, Fan developed a stress analysis approach and finite element (FE) models. FE analysis of a TFG curved bridge framing system (girders and cross-frames) with dead loads and also of a TFG curved bridge framing system with a composite concrete deck with dead and live loads, were carried out. Curved TFGs have less warping normal stress and cross section rotation compared with corresponding curved steel I-girders, particularly for individual girders. The cross-frames in a curved TFG system can be lighter compared with those in a corresponding curved steel I-girder system, since the cross-frame forces are reduced. Both a curved bridge with a composite concrete deck, a TFG system and a corresponding steel I-girder system, have similar behaviour. However, fewer cross-frames are needed in the curved TFG system compared with the corresponding curved steel I-girder system. Dong and Sause (2009a, 2009b) used the design criteria from the 2004 AASHTO LRFD Bridge Design Specifications for conventional curved steel I-girders to curved TFGs. The FE findings showed that these equations can be used for the safe design of curved TFGs for highway bridges.

2.5.1 Individual curved TFGs with two hollow tube flanges

Curved TFGs with rectangular hollow steel tubes for both flanges were studied by Dong and Sause (2010). FE studies were completed on individual girders and simply supported three-girder systems of curved hollow TFGs and standard steel I-girders. For comparative purposes, the curved hollow TFGs and steel I-girders had similar weight, depth, and flange width. The span, L, was kept constant and the radius of curvature, R, was varied in order to produce different L/R ratios from 0.1 to 0.45 for studying torsional effects. A study of an individual curved hollow TFG was completed in order to determine the effects of several parameters, such as cross section distortion, stiffeners, tube diaphragms and cross-section dimensions on the load capacity (Dong and Sause, 2010), as shown in Fig. 2.22. The results indicated that cross-section distortion decreases the load capacity, however, the use of stiffeners and diaphragms in the steel tubes mitigate this distortion. Furthermore, second-order effects, initial geometric imperfections and residual stresses were taken into consideration. The FE analysis results indicate that initial geometric imperfections and residual stresses do not have a huge influence on the load capacity.

The behaviour of both curved TFG systems and corresponding steel I-girder systems was compared by Dong (2008). The research showed that curved TFGs have several advantages including: (1) an individual curved TFG improves smaller vertical displacement, less warping normal stress owing to the greater torsional rigidity, less total normal stress and smaller cross-section rotation when compared with a corresponding curved steel I-girder subjected to the same load. (2) an assembled curved TFG system improves less interior diaphragm (or cross frame) forces compared with a corresponding curved steel I-girder system. The steel I-girder has less principal bending stress, because of the slightly higher flexural rigidity. (3) a smaller number of interior diaphragms (or cross frames) are required for an assembled curved TFG system than for a corresponding curved steel I-girder system. The curved TFG with hollow flanges has a lesser maximum whole longitudinal normal stress compared with the conventional I-girder, since the steel I-girder has much greater warping normal stress. (4) individual curved TFGs with hollow flanges can be carried their own weight across the span without temporary shoring or bracing within the span, whereas individual curved steel I-girders would need temporary support during erection. The overall cross-section areas as well as dimensions of both TFGs and the corresponding steel I-girder were maintained similarly in this work.

A 1/2-scale individual curved TFG with hollow steel tube flanges and concrete infilled ends test specimen was examined by Putnam (2010), as shown in Fig. 2.23. The behaviour of the curved TFG subjected to vertical loads was studied and the results revealed that an FE model, which was validated using test results, can accurately predict vertical displacements, cross-section rotations, typical strains and shear strains away from the ends of the curved TFG. A parametric study of the end conditions and the shear strains near the ends of the curved TFG was carried out considering internal steel tube diaphragms and infilled concrete. The end conditions had an important influence on the shear strains, with the values depending on the method of stiffening used, the position of the internal diaphragm and the extent to which the infill concrete was extended.

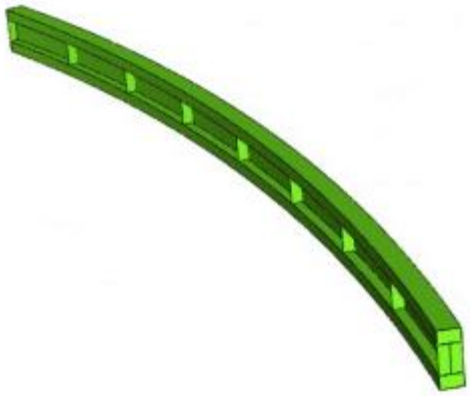

Fig. 2.22 FE model of an individual curved TFG with two hollow tube flanges (Dong and Sause, 2010)

Fig. 2.23 Curved TFG with hollow steel tube flanges and concrete infilled ends (Putnam, 2010)

2.5.2 Curved systems of TFGs with two hollow tube flanges

FE analyses on three-girder systems of curved TFGs with hollow flanges were conducted by Dong and Sause (2010), as illustrated in Fig. 2.24. The schemes were compared with curved three I-girder systems. The horizontal curvature, the dimensions of the cross-section, the number of cross-frames and inclusion of composite action with the concrete deck were varied. The minor decrease in load capacity as a result of initial geometric imperfections and residual stresses was neglected. The three-girder systems were loaded

with a vertical and uniformly distributed load over the span. There were two main loading conditions under consideration. During construction of the deck, the first loading condition was loading of the girder system alone (without a composite concrete deck). In the final constructed condition, the second loading scenario was loading of the girder system with a composite deck. The curved TFGs (with hollow flanges) in the three-TFG system had a lesser maximum entire normal stress compared with the corresponding steel I-girders in the three-I-girder system (Dong and Sause, 2010). Moreover, both three-girder systems had similar vertical displacements. Within the I-Girder system, the maximum cross-frame force was significantly higher than that in the TFG. The three-girder systems with a composite concrete deck have improved stiffness and load capacity, a reduced maximum normal stress, vertical displacement and maximum cross-frame force. The load capacity of the TFG system is the same as the load capacity of the I-girder system.

A further study was carried out by Sause (2015) on curved TFGs. The results indicated that the curved TFGs, which have great torsional stiffness, have significantly larger load carrying capacity than standard straight beams. The advantages of a curved TFG with hollow flanges system compared with corresponding curved steel I-girder system were summarised by Sause (2015) as follows:

- Under similar load, the TFGs improve fewer whole normal stress compared with corresponding curved steel I-girders.
- The forces in the cross-frames of the TFG systems are less than in the corresponding curved steel I-girder systems and thus, lighter cross-frame members can be used for the TFG systems;
- Smaller numbers of cross-frames are required for the TFG systems;
- Without any support within the span and without interior cross-frames, the TFG systems can carry their own weight (plus the weight of a concrete deck) and may therefore not need temporary support for the TFG Systems during the construction (before the concrete deck is composite with the girders), which makes bridge erection quicker and less costly.

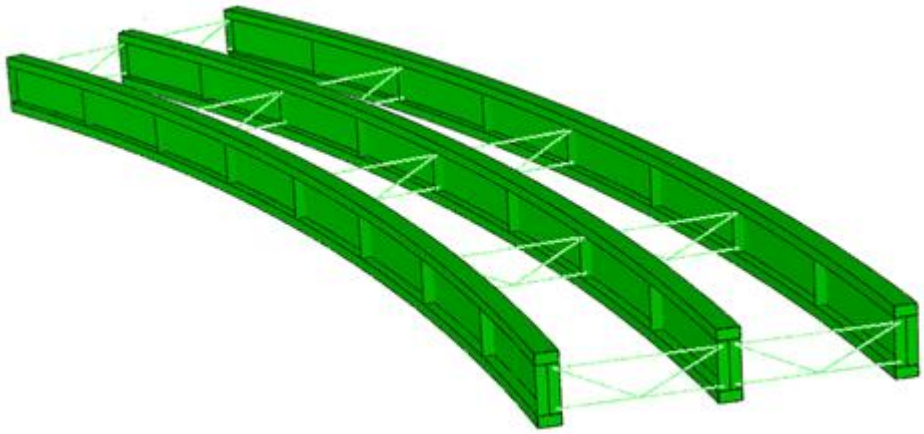

Fig. 2.24 FE model of a curved system of TFGs with two hollow tube flanges (Dong and Sause, 2010)

2.5.3 Curved TFGs with single hollow tube top flange

Tests on a large-scale test specimen were required to validate the FE results and design criteria equations established by Dong and Sause (2009b). A TFG with only one hollow tube as the compression flange was investigated by Ma (2014), being selected rather than two tubular hollow flanges for several reasons. Firstly, local deformations of the tension hollow tube flange can occur at the bearings owing to the compressive force from the reactions. To avoid these deformations, the tube would require an internal steel diaphragm or infilled concrete. Secondly, there is the possibility of a greater bending force with a flat plate with suitable width and height than a tube with the bottom flange, since the tubes are provided at limited depth and width when the girder is composite with a concrete deck (in the final constructed condition). Thirdly, the unit cost of steel plates is lower than that for steel tubes.

A 2/3-scale sample specimen was designed, fabricated and erected/assembled with two curved hollow TFGs braced with three intermediate diaphragms (Ma, 2014; Putnam, 2010), as presented in Fig. 2.25. The results showed that FE models are suitable for prediction for several parameters, such as vertical displacement, cross section rotation, normal strain, and shear strain compared to experimental test results. Ma (2014) conducted further studies on curved hollow TFGs and curved hollow TFG systems. FE models were developed and examined for additional curved hollow TFG systems. Parametrical studies on the erection process of the TFG systems, which included installation of the diaphragms or cross-frames, were used for the FE models.

Fig. 2.25 Curved TFG with hollow steel tube top flange (Ma, 2014)

2.6 Combined tubular flange with a corrugated web

Combining the idea of using tubular flanges with corrugated web results in the development of beams in which the corrugate web can contribute to the resistance to local buckling and the tubular flange is efficient at increasing the global stability of the girders. The use of rectangular thin wall tubes as the flanges which are continuously welded to the webs. Two kinds of web corrugation profiles are usually used in these beams: one is trapezoidal, which is the most commonly used; the other is sinusoidal corrugation, which is used sometimes in constructions that have unusual requirements to prevent fatigue failure.

Wang (2003) investigated the behaviours of hollow tubular flanges with a corrugate web under different loading conditions through both testing and FE analysis (Fig. 2.26). Steel members with trapezoidal corrugated webs and tubular flanges were subjected to shear, bending, and axial compression during the test stage. The work involved the testing of full scale specimens and nonlinear FE analyses. The results indicated that FE analysis is an effective way to predict the failure load and failure mode of the structural members of combined corrugated webs with tubular flanges.

Shao and Wang (2016) conducted a study to examine the shearing behaviour through experimental testing of a short girder combined rectangular concrete-filled tubular flange with a corrugated web subjected to three-point loading. Based on the experimental results, the girder combined rectangular concrete-filled tubular flange with a corrugated web had

both higher load carrying capacity and better ductility in comparison with the conventional steel I-girder. In 2017, Shao and Wang also studied the static behaviour of two specimens of tested girder under concentrated load at mid-span. One of these two was a standard I-girder with flat-plate flanges, whilst the other was a rectangular tubular flange filled with concrete, a flat-plate flange and a trapezoidal corrugated web. The experimental testing results demonstrated that the conventional steel I-girder fails due to global buckling, since this is an open section, which has weak resistance to torsion. On the other hand, the rectangular concrete-filled tubular flange with trapezoidal corrugated web, which has a significantly developed torsional stiffness owing to a closed section at the tubular flange, fails through flexural yielding at the mid-span. Moreover, the corrugated web can still resist the shear force as a result of its improved bending stiffness.

El Hadidy et al. (2018) studied large-scale bridge girders with corrugated webs and hollow tubular flanges under constant shear loading, with the main aim of examining the effect and behaviour of using hollow tubular flanges on the strength of these girders. With respect to strength enhancement, the results indicated that using hollow tubular flange increases the shear by about 20% (and more by increasing the depth of the flange) compared with the girders of flat flanges. The initial stiffness also increased as well.

Fig. 2.26 Hollow tubular flanges with trapezoidal corrugated webs (Wang, 2003)

2.7 The finite element method (FE)

Finite element analysis (FE) is now one of the most famous and widely used techniques for simulating and analysing structures. The main objective of this numerical method is to divide the structure into small divisions or elements, where each element is defined by a particular number of nodes (this process involves modelling a body by dividing it into an equivalent system of lesser bodies or units called finite elements). The finite element method (FE) is a numerically acceptable solution, which results in a solution system of simultaneous algebraic equations instead of requiring analytical solutions (solutions of ordinary or differential equations), which because of the complicated geometries, loadings, and material properties, are frequently not available.

The modern development of FE started with the use of (one-dimensional) elements (bars and beams) in structural engineering by Hrennikoff in 1941 and McHenry in 1943. In 1947, Levy improved the flexibility or force method, and in 1953 he proposed that another method (the stiffness or displacement method) could be a promising alternative for use in analysing statically redundant aircraft structures. His equations, however, were cumbersome to solve by hand and thus, became commonly deployed only after the advent of high-speed computers. Turner (1956) were the first to introduce the treatment of two-dimensional elements. They derived stiffness matrices in plane stress for truss elements, beam elements, and two-dimensional triangular and rectangular elements. The FE was expanded to cover three-dimensional problems only after the improvement of the tetrahedral stiffness matrix, which was undertaken by Martin in 1961.

2.8 Numerical studies of tubular flange girders

Today, FE has emerged as a powerful analytical tool for structural analysis with the development of digital computers and numerical techniques. This has aided engineers in modelling several aspects of the phenomenological behaviour encountered in TFGs (Kim and Sause, 2005). The effect of confinement, modelling of cracking and crushing, behaviour of the materials after cracking and crushing and many other characteristics are some of these aspects. Carrying out experimental parametric studies consumes a lot of time and results in high research costs. Regarding which, finite element analysis is an effect approach for studying the influence of several parameters of structural behaviour under different loading conditions. Extensive research has been conducted using the FE to study the structural response of hollow and concrete filled TFGs with different tubular

flange shapes. The outputs indicate reasonable and expected results in parametric studies using the validated models.

A suitable finite element software code should be used to design the various characteristics of the CFTFG for establishing a functional and reliable model, such as the interaction between the steel tube and the concrete core, the failure mode and the material properties (Hassanein, 2015). In many numerical studies on TFGs, the hollow and concrete filled tubes under almost quasi-static and dynamic loading, the software package ABAQUS was efficiently used. The findings show that the numerical results are in good agreement with the corresponding experimental data. In addition, a numerical study was also conducted to simulate flexural behaviour using another software program, ANSYS, for beams with pentagonal (CFTFG) subjected to mid-span loading (Gao et al, 2014).

2.9 Concluding remarks

This chapter showed effectively how CFTFGs are a viable alternative bridge when erected span by span. It has also revealed improved performance of CFTFGs over conventional plate girders. As verified during construction, CFTFGs have improved strength and stability during steel erection and deck placement. These attributes eliminate the need for many diaphragm lines or cross frames required in typical girder plate bridges. In addition, the CFTFG enables engineers to use shallower sections at places where depth limits are a concern. Erecting CFTFGs as simple spans over obstacles like traffic lanes results in much easier and quicker construction of bridges. The steel erection will continue faster, with fewer diaphragms.

It should be noted that although CFTFGs have several indicated advantages over conventional steel plate I-girders. Decreasing the web depth (h_w) reduces the volume of steel in the section as well as the fabrication costs as less welding is required and the associated risk of weld distortion is lowered. Constructing the field splices at the piers, with the temporary bearings also resulted in a couple of weeks of extra construction time which is somewhat offsetting due to less diaphragms and contact plates for manufacturing and erecting.

Chapter 3 : Flexural behaviour of circular concrete filled tubular flange girders (CCFTFGs)

3.1 Introduction

In this chapter, the flexural behaviour of circular concrete filled tubular flange girders (CCFTFGs) and circular steel tubular flange girders (STFGs) is examined. These type of girders have a similar shape to conventional steel beams, but the top flange plate is replaced with a hollow steel section. The tube may be infilled with concrete to create a concrete filled tubular flange girder (CFTFG).

3.2 Numerical modelling

3.2.1 General

The finite element analysis package ABAQUS 6.14-4 (Simulia, 2011) was employed to examine the ultimate moment capacity of simply supported CFTFGs, considering the geometrical and material nonlinearities. The numerical models contained an initial geometric imperfection which was generated by means of the first buckling mode shape of a perfect beam (i.e. perfectly straight and constant geometry) multiplied by an amplitude factor. For this purpose, an elastic eigenvalue buckling analysis was first conducted, and then the first buckling mode shape of the beam with an imperfection amplitude of L/1000, where L is the beam length, was imported to the nonlinear model as the starting geometry. The global imperfection amplitude was taken as L/1000, in accordance with the permitted out-of-straightness tolerance in CEN 1090-2 (2008) and the AISC (1999), and has been used by other researchers in similar studies [e.g. Hassanein, 2015; Kim and Sause, 2005]. The global imperfection amplitude was taken as L/1000, where L is the column length, in accordance with the permitted out-of-straightness tolerance in EN 1090-2.

The implicit dynamic analysis method in ABAQUS was used to solve the geometrically and materially nonlinear problem, where the load was applied incrementally and the nonlinear geometry parameter (*NLGEOM, in ABAQUS) was included to allow for changes in the geometry under load. This nonlinear dynamic analysis method uses an implicit time integration scheme to determine the quasi-static response of the system, which was found in the current study to provide the best convergence behaviour owing to the high-energy dissipation associated with quasi-static applications during certain stages of the loading history.

3.2.2 Details of validation model

The specimen details incorporated in the validation FE model are based on the circular tubular flange girder which was examined in the test programme of Wang et al. (2008). Accordingly, the cross-section is 0.5 m in height and 4.3 m in length, as shown in Figs. 3.1 and 3.2. Table 3.1 presents the principal dimensions of the tests, namely D_{tube}, t_t, h_w, t_w, b_f, t_f, and $t_{stiffener}$ which represent the tube outside diameter, tube thickness, web depth, web thickness, width of the bottom flange, thickness of the bottom flange and stiffener thickness, respectively. The beam is subjected to two concentrated loads in the vertical direction on the top surface and the distance between the loading points is 1 m. There are four stiffeners along the beam length, as shown in Fig. 3.2, and each has a thickness of 12 mm. These are located at the supports and loading points in order to prevent local instability of the web at these locations. Simply supported boundary conditions in the tests were simulated in the FE model by restraining suitable displacement and rotational degrees of freedom at the beam ends. The steel section was made from Q235 steel, and the material properties incorporated in the model are presented in Table 3.2 including the yield strength f_y, ultimate strength f_u, Young's modulus (E_s) and Poisson's ratio (Ding al., 2009). Also included in the Table 3.2 are the compressive strength f_c and Poisson's ratio of the concrete.

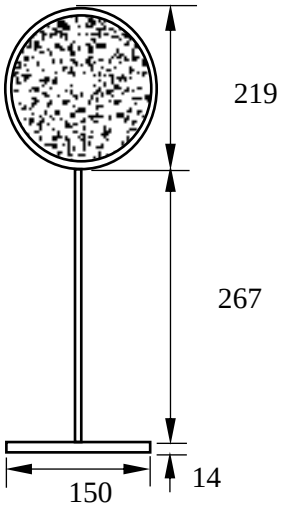

Fig. 3.1 Cross-section of a composite beam with a concrete filled circular tubular flange (all units in mm)

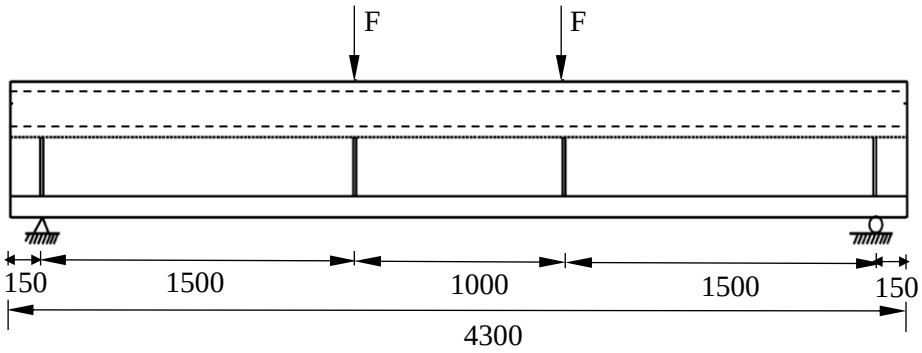

Fig. 3.2 Schematic of the simply supported beam (all units in mm)

Table 3.1 Dimensions of the CCFTFG cross-section

D_{tube} (mm)	t_t (mm)	h_w (mm)	t_w (mm)	b_f (mm)	t_f (mm)	$t_{stiffener}$ (mm)
219	8	267	6	150	14	12

Table 3.2 Details of the material properties

Steel (Ding et al., 2009)				Concrete (EN 1992-1-1, 2004)	
Yield stress, f_y (N/mm^2)	Ultimate stress, f_u (N/mm^2)	Young's modulus, E_s (N/mm^2)	Poisson's ratio	Compressive cylinder strength of concrete, f_c (MPa)	Poisson's ratio
287.9	430.2	195000	0.28	38.6	0.20

3.3 Material modelling

3.3.1 Concrete

The stress-strain relationship of unconfined concrete is shown in Fig. 3.3, where f_c is the unconfined ultimate cylinder compressive strength of concrete, ε_c is the corresponding strain at f_c which is determined (as a percentage) as given by Eq. (3.1) in accordance with Eurocode 2 Part 1-1 (EN 1992-1-1, 2004).

$$\varepsilon_c = 0.7(f_c)^{0.31} \leq 2.8 \quad (3.1)$$

When the concrete filled steel tube is exposed to axial compression, a gap occurs between the steel tube and the concrete core in the elastic range because Poisson's ratio for the concrete is smaller than that of the steel tube. Beyond the elastic range, the inner concrete dilates (strains transversely) at a higher/faster rate than the steel tube, hence making

contact between the steel tube and the concrete to develop again. As the axial compressive stress increases further, continued dilation of the concrete core is restricted by the steel tube, generating a variable confining pressure in the concrete in the transverse direction. This confining pressure effectively increases the compressive strength of the concrete core. In a CCFTFG, the concrete is confined by the circular steel tube section, which results in increased ductility and strength of the concrete core, compared to unconfined concrete.

In the current study, the stress-strain response of confined concrete proposed by Hu et al. (2003) is adopted in the numerical simulations. This approach has been adopted by other researchers for the simulation of concrete filled tubular columns which are eccentrically loaded, leading to non-uniform confining pressure, as occurs in the current scenario (Lee et al., 2011; Ellobody, 2013). Typical uniaxial stress–strain curves of unconfined concrete is shown in Fig. 3.3, where f_{cc} and ε_{cc} are the uniaxial compressive strength and the corresponding strain of confined concrete, respectively. Mander et al. (1988) proposed relationships between confined and unconfined concrete strength and strain values, as given by Eq. (3.2) and (3.3), respectively.

$$f_{cc} = f_c + k_1 fl \tag{3.2}$$

$$\varepsilon_{cc} = \varepsilon_c \left(1 + k_2 \frac{fl}{f_c}\right) \tag{3.3}$$

Values of 4.1 and 20.5 are used for k_1 and k_2, respectively, based on the study of Richart et al. (1928). The term 'fl' denotes the confining pressure in the concrete, which is determined in the current study based on the empirical relationships presented in Eqs (3.4) and (3.5) proposed by Hu et al. (2003).

$$fl/f_y = 0.043646 - 0.000832(D_{tube}/t_t) \quad \text{for} \quad 21.7 \leq D_{tube}/t_t \leq 47 \tag{3.4}$$

$$fl/f_y = 0.006241 - 0.000357(D_{tube}/t_t) \quad \text{for} \quad 47 \leq D_{tube}/t_t \leq 150 \tag{3.5}$$

The stress-strain curve of confined concrete, as presented in Fig. 3.3, consists of three parts. Initially, it is assumed that the confined concrete responds linearly, obeying Hooke's law, and this continues up to around 40% of compressive strength in the ascending branch (EN 1992-1-1, 2004; Goode and Lam, 2011). During this phase of the response, the behaviour of confined and unconfined concrete is identical, as shown in Fig. 3.3. The initial Young's modulus (in GPa) can be estimated with reasonable accuracy

from the empirical formulation provided in Eurocode 2 (EN 1992-1-1, 2004) given in Eq. (3.6).

$$E_c = 22 \times (f_c/10)^{0.3} \tag{3.6}$$

The second part of the stress-strain curve defines the nonlinear behaviour before the concrete reaches its maximum strength, starting from the proportional limit ($0.4f_c$) to the maximum confined concrete strength f_{cc}. The relationship of concrete stress σ_c and strain ε in this part of the response was proposed by Saenz (1964), and is as described by Eq. (3.7)-(3.9)

$$\sigma_c = \frac{E_c \varepsilon}{1+(R+R_E-2)\left(\frac{\varepsilon}{\varepsilon_{cc}}\right)-(2R-1)\left(\frac{\varepsilon}{\varepsilon_{cc}}\right)^2+R\left(\frac{\varepsilon}{\varepsilon_{cc}}\right)^3} \tag{3.7}$$

where:

$$R_E = \frac{E_c \varepsilon_{cc}}{f_{cc}} \text{ and} \tag{3.8}$$

$$R = \frac{R_E(R_\sigma - 1)}{(R_\varepsilon - 1)^2} - \frac{1}{R_\varepsilon} \tag{3.9}$$

where R_ε and R_σ were both assumed to be 4.0, in accordance with the recommendations by Hu and Schnobrich (1989).

The third and last part of the curve is the descending branch which begins at the maximum confined concrete strength f_{cc} and decreases linearly until a stress of $f_{c,u}$ is reached at a corresponding strain of $\varepsilon_{c,u}$, which are determined as given in Eqs (3.10) and (3.11), respectively.

$$f_{c,u} = rk_3 f_{cc} \tag{3.10}$$

$$\varepsilon_{c,u} = 11\varepsilon_{cc} \tag{3.11}$$

where the value of the parameter k_3 for concrete filled circular steel tubes is calculated using Eq. (3.12), based on the recommendations presented by Hu et al., (2003).

$$k_3 = 1 \quad \text{for} \quad 21.7 \leq D_{tube}/t_t \leq 40 \tag{3.12}$$

$$k_3 = 0.0000339\left(\frac{D_{tube}}{t_t}\right)^2 - 0.010085\left(\frac{D_{tube}}{t_t}\right) + 1.3491 \text{ for } 40 \leq D_{tube}/t_t \leq 150$$

As a result of the experimental studies carried out by Giakoumelis and Lam in 2004, it was proposed by (Ellobody et al., 2006; Ellobody and Young, 2006) that the parameter r may be taken as 1.0 for concrete with cube strength of 30 MPa and 0.5 for concrete with a cube strength of 100 MPa and linear interpolation can be used for intermediate values.

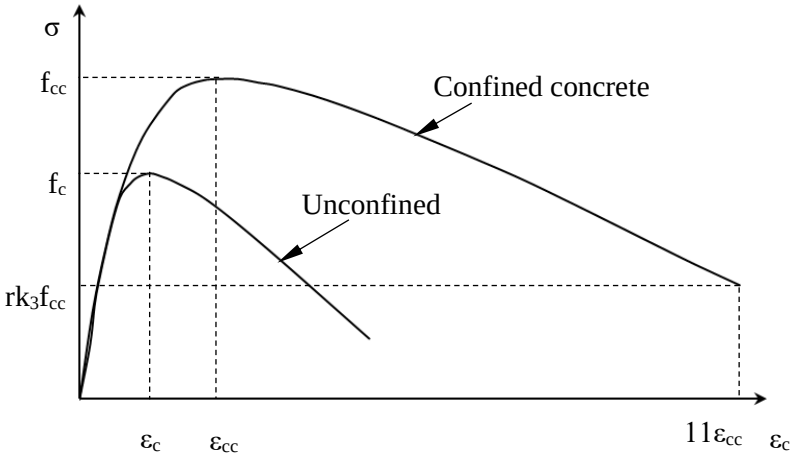

Fig. 3.3 Typical stress-strain curve of confined and unconfined concrete (reproduced from Hu et al., (2003))

In the ABAQUS FE model, the concrete infill is represented using 8-noded brick elements with reduced integration, known as C3D8R in the ABAQUS library. The concrete damaged plasticity (CDP) model is employed for modelling the constitutive behaviour of the concrete, based on the relationships described before. The model assumes that the infilled concrete fails either in compression, through crushing, or tension, through cracking. In addition to the compressive and tensile constitutive relationships, a number of other parameters are required in the CDP model, including the dilation angle, flow potential eccentricity and viscosity parameter which are assigned values of 36˚, 0.1, and 0, respectively, as used by other researchers (Kmiecik and Kamiński, 2011). The ratio of the strength in the biaxial state to the strength in the uniaxial state, f_{b0}/f_c, is taken as 1.16 whilst the ratio of the second stress invariant on the tensile meridian (K) is given a value of 0.667 in the present analysis.

In addition, the compressive damage parameter d_c needs to be defined at each inelastic strain level. It ranges from zero, for undamaged material, to unity, when the material can

no longer sustain any load. The value for d_c is found only for the descending branch of the stress-strain curve of concrete in compression, as given by Eqs (3.13) and (3.14).

$$d_c = 0 \qquad \text{when } \varepsilon_c < \varepsilon_{cc} \tag{3.13}$$

$$d_c = \frac{f_{cc} - \sigma_c}{f_{cc}} \qquad \text{when } \varepsilon_c \geq \varepsilon_{cc} \tag{3.14}$$

In this study, it was assumed that after the tensile strength of concrete f_t at corresponding strain of ε_{cr} has been reached, the tensile strength decreases linearly to reach zero stress at a total tensile strain at the end ε_{end} of 0.01, as shown in Fig. 3.4. The tensile strength of concrete f_t, according to Eurocode 2 (EN 1992-1-1, 2004), is taken from Eqs (3.15) and (3.16).

$$f_t = 0.3 {f_c}^{2/3} \qquad \text{for } f_c \leq 50 \text{ N/mm} \tag{3.15}$$

$$f_t = 2.12 \ln(1 + 0.1 f_c) \qquad \text{for } f_c > 50 \text{ N/mm}^2 \tag{3.16}$$

Similar to the simulation of concrete in compression in the CDP model, the tensile damage parameter d_t, which is valid only in the descending branch of the stress-strain curve for concrete in tension, is defined at each increment of cracking strain, as described by Eqs (3.17) and (3.18). follows:

$$d_t = 0 \qquad \text{for } \varepsilon_t < \varepsilon_{cr} \tag{3.17}$$

$$d_t = \frac{f_t - \sigma_t}{f_t} \qquad \text{for } \varepsilon_t \geq \varepsilon_{cr} \tag{3.18}$$

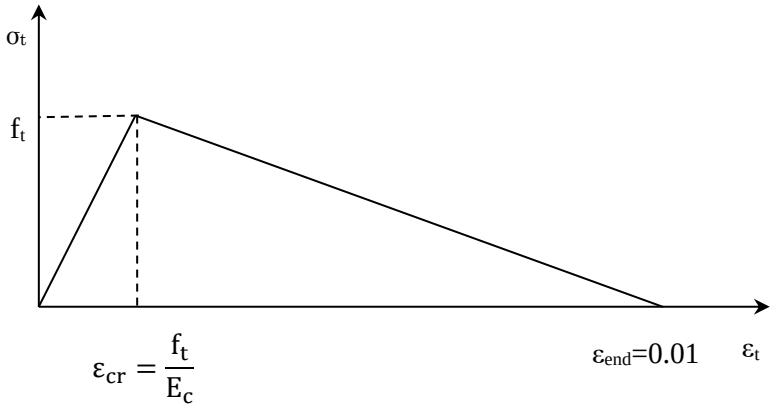

Fig. 3.4 Tensile stress-strain curve for concrete

3.3.2 Steel

The steel employed in the tested beam which is used later for validation is Q235 steel with nominal yield stress and ultimate tensile stress of 287.9 and 430.2 MPa, respectively

(Ding et al., 2009). An idealised tri-linear stress–strain relationship is assumed to model the steel material in the FE model, as shown in Fig. 3.5, where f_y and ε_y are the yield stress and strain, respectively, ε_{st} is the strain at the onset of strain hardening and f_u and ε_u are the ultimate tensile stress and strain at ultimate tensile stress, respectively. The key values used in the model are presented in Table 3.2. The strain at the onset of strain hardening ε_{st} and the strain at the ultimate tensile stress ε_u are taken as 0.025 and 0.2, respectively (Ban and Bradford, 2013). The engineering stress–strain (σ_{eng}-ε_{eng}) curve is converted to true stress–strain (σ_{true}-ε_{true}) curve for the ABAQUS model using Eqs (3.19) and (3.20), respectively.

$$\varepsilon_{true} = \ln(1 + \varepsilon_{eng}) \tag{3.19}$$

$$\sigma_{true} = \sigma_{eng}(1 + \varepsilon_{eng}) \tag{3.20}$$

The top tubular flange, web, bottom flange and stiffeners are all modelled using the four-noded, three-dimensional shell element with reduced integration (S4R in the ABAQUS library). The S4R element has six active degrees of freedom per node, including three displacements and three rotations. The reduced integration enables more efficient computation without compromising the accuracy of the results. A tie contact is defined between the surface of the steel section and the edges of the stiffeners. Following a mesh sensitivity study, it has been found that an element size of 30×30 mm provides the best combination of accuracy and computational efficiency and therefore is applied to all elements in the model. The finite element mesh of a typical specimen is presented in Fig. 3.6(a).

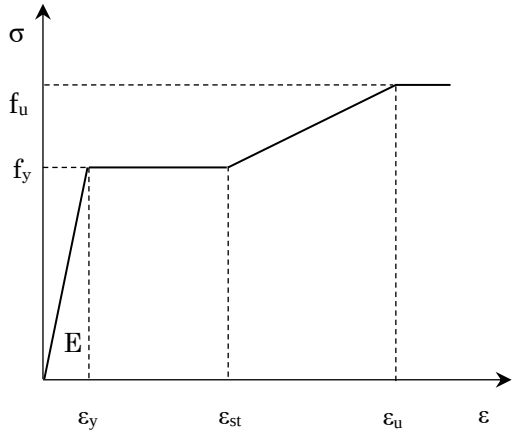

Fig. 3.5 Stress–strain curve of steel beam (reproduced from Ban and Bradford, 2013)

3.4 Support and loading conditions

The geometry and loading conditions of the beam are symmetrical about the mid-span and therefore only half the girder length is modelled. Accordingly, one end section of the beam model has simply supported boundary conditions whilst the other end has symmetrical boundary conditions, as shown in Fig. 3.6(b), in which u_x, u_y, u_z, θ_x, θ_y, and θ_z are the displacements and the rotations about the global x, y and z axes, respectively. The y-z plane is considered to be in-plane whilst the x-z and x-y planes are out-of-plane, in the current study. At the end of the beam (i.e. at the support), the vertical u_y and lateral displacements u_x of all nodes along the y-axis (i.e., when x = 0), and the twist rotations about z and y-axes (θ_z and θ_y) are restrained against movement and therefore assigned values equal to zero. At the middle of the beam, the longitudinal displacements u_z and rotations about the x and y-axes (θ_x and θ_y) are also restrained against all movement. The loading is applied to the top surface of the beam in displacement control through two concentrated loads along the full length or one loading point when half the span is considered.

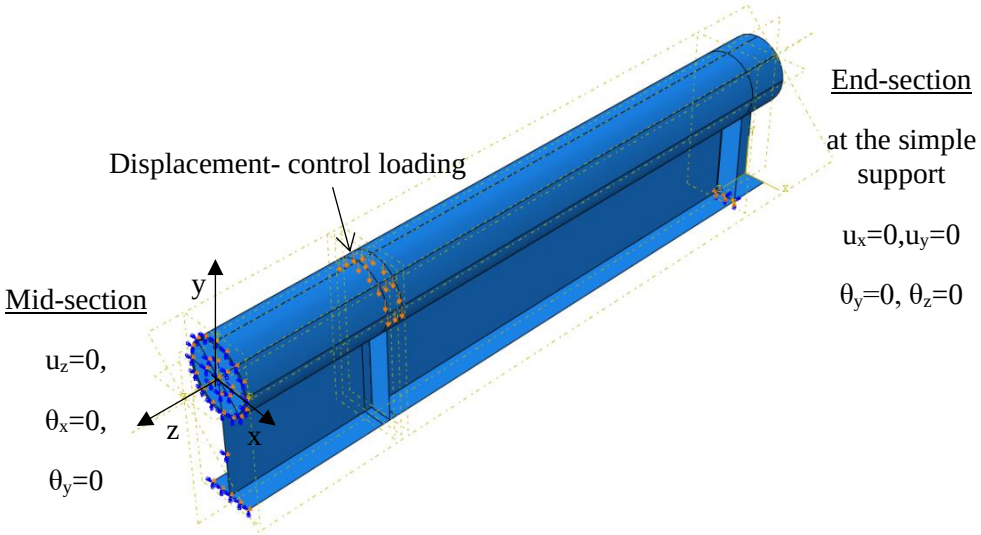

(a)

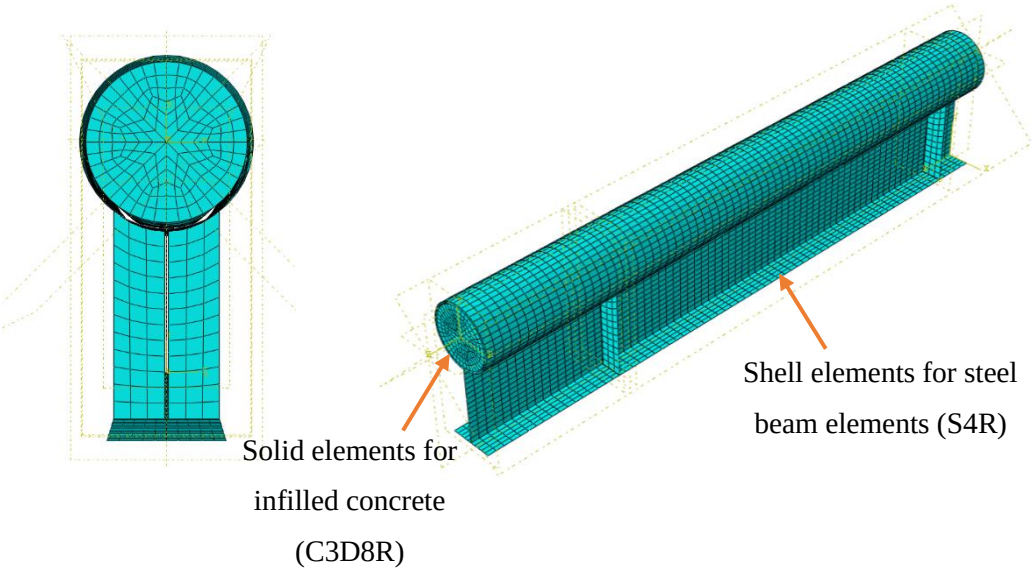

(b)

Fig. 3.6 FE model for the CCFTFG, including (a) finite element mesh and (b) support and loading conditions

3.5 Validation of the load-displacement response

To assess the accuracy of the load-displacement response generated by the FE model, the test conducted by Wang et al. (2008) was simulated as described in previous sections. This is the only test which has been done on concrete filled tubular flange girders with a circular top flange, to date, in the public domain. The load-displacement response of the CCFTFG from both the FE model and the experimental programme is presented in Fig. 3.7. From Fig. 3.7, it is clear that the FE model is capable of providing a good representation of the general response and also offers an excellent prediction of the ultimate load and moment of the CCFTFG. Residual stresses are not incorporated in the FE model as it has been shown that they can be neglected for short unbraced members which are less than 20 m in length (Dong and Sause, 2009a).

In terms of the general behaviour, and with reference to Fig. 3.7, it can be observed that the response predicted by the FE model is divided into four phases. Firstly, below a load of around 400 kN, there is a linear relationship between load and displacement in the elastic phase, and the response is very well predicted by the model in this range. Secondly, when the load reaches 500-600 kN, the behaviour becomes nonlinear. With the expansion of the yielded region from the bottom flange to the middle of the steel section, the flexural rigidity decreases and the stress redistributes. In this elastic-plastic stage, there are some disparities between the experimental and numerical curves and the model somewhat over-predicts the capacity of the beam. This difference is likely to be due to a combination of factors which affect deformations, such as the idealisation of the material nonlinearity in

the FE model as well as the likelihood of initial imperfections in the real structure. In the third phase, when loading exceeds 600 kN, the displacement increases rapidly as plasticity spreads in the middle region of the beam. Finally, in the fourth phase when the load reaches around 728 kN, the response plateaus as the displacement continues to increase with very little change in the load. The failure mode observed in both the FE model and the experiment, is a combination of steel yielding and torsional buckling. Overall, the simulated load-deformation curves reflect the experimental behaviour very well. Although there is only one experiment available for validation which is not ideal, it is concluded that the FE model is capable of predicting the behaviour and strength of that member and is suitable for conducting further parametric studies on CCFTFGs under bending.

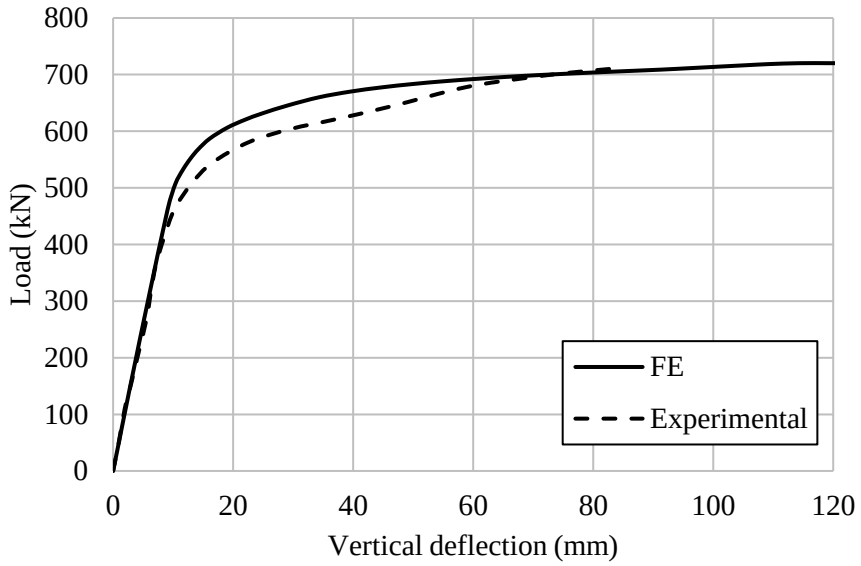

Fig. 3.7 Load versus deflection relationship from the FE analysis and experimental results

3.6 Use a proper stress-strain curve of steel in validation

Both a multi-linear (trilinear) and a bilinear stress-strain curves are studied in the analysis of CCFTFG model. The typical stress-strain curves are illustrated in Fig. 3.8, including (a) multi-linear (trilinear) curve and (b) bilinear curve. The results of FE model are very similar and are capable of providing a strong overall response representation with an excellent prediction of the CCFTFG's ultimate load and moment, as shown in Fig. 3.9 . Therefore, it is not deemed necessary to model the steel in the more complicated way (multi-linear) for the rectangle CFTFG, see chapter 5.

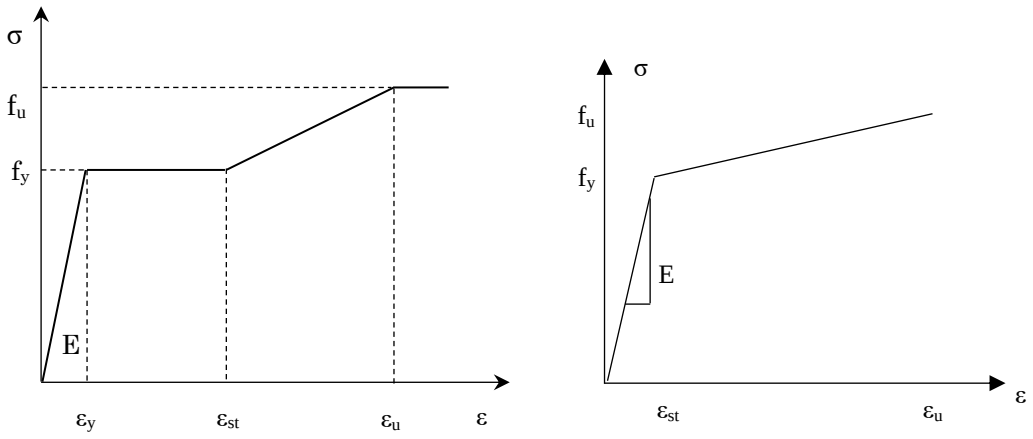

(a) Multi-linear (trilinear) curve

(b) Bilinear curve

Fig. 3.8 Different stress-strain curve of steel beam

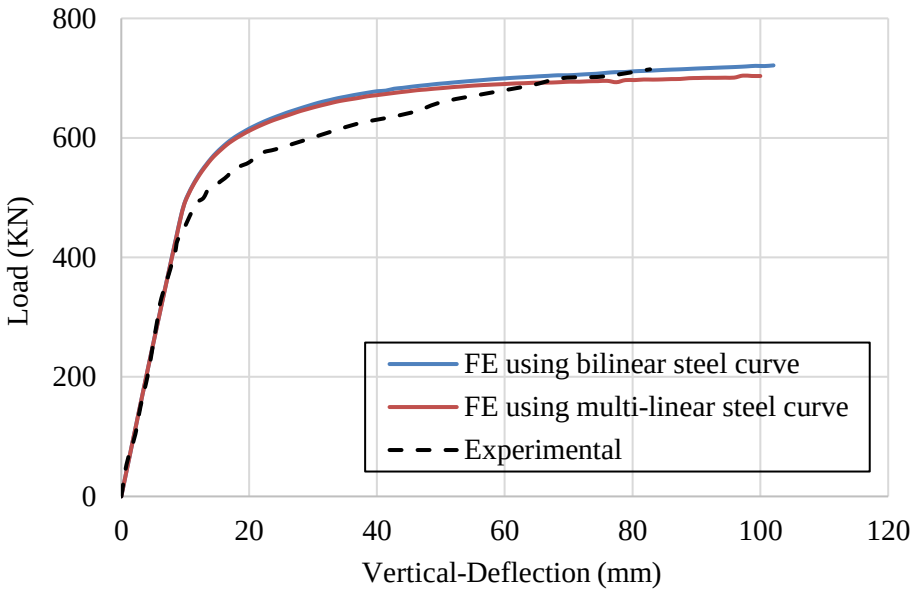

Fig. 3.9 Load versus deflection relationship using different stress-strain curve of steel beam

3.7 Analytical model for flexural strength

In this section, a series of analytical expressions for predicting the bending capacity of circular CFTFGs are developed which can be used both for analysis and design of these members. The approach is based on plastic theory in which the position of the plastic neutral axis and the plastic bending moment capacity can be identified by applying the equilibrium of internal forces equations to the cross-section. An equivalent rectangular and triangular stress block is assumed for the concrete (as shown in Fig. 3.10 and

discussed hereafter) and the steel is assumed to behave in an elastic-perfectly plastic manner. The confining effect provided by the steel tube on the concrete infill is considered in the analytical model.

3.7.1 Location of the plastic neutral axis

In order to determine the bending capacity of the section, it is first necessary to determine the location of the plastic neutral axis (PNA). Two cases are considered in this study. Case 1 assumes that the PNA is in the web of the steel section, as shown in Fig. 3.10, while Case 2 assumes that the PNA is in the tubular flange, as demonstrated in Fig. 3.11. With reference to these figures, and in order to determine the exact location of the PNA, the following assumptions are adopted:

- If the PNA is within the concrete filled portion of the section, it is assumed the concrete below the plastic neutral axis does not contribute to the tension capacity.
- By assuming $x_0=0$ and $y_0=y_1-R$, the coordinate (x_0, y_0) is the centre of the circular tube, where R is the outer radius of the steel tube.
- The term y_2, which is the vertical height of the triangular stress block is determined by interpolating the strain distribution across the cross-section, given by:

  $\frac{\varepsilon_{cc}}{y_1-t_t}=\frac{\varepsilon_y}{y_2} \rightarrow y_2=\frac{\varepsilon_y}{\varepsilon_{cc}}(y_1-t_t)$.
- In the triangular stress block, where the steel is behaving in an elastic manner (i.e. $f_s = \varepsilon_s E$, where f_s and ε_s are the stress and strain in the steel section, respectively, and E is the elastic modulus) interpolation can be applied to establish that, at any location y in this region, the stress in the steel is determined as:

  $f_s=\frac{yf_y}{y_2}$.

As shown in Figs. 3.10 and 3.11, y_1 is the distance from the top of the cross section to the PNA. For Case 1, $y_1 > D_{tube}$ (where D_{tube} is the outer diameter of the steel tube), and therefore the PNA is within the steel web. On the other hand, for Case 2, $y_1 < D_{tube}$, and the PNA is within the concrete filled tube infilled concrete. Both cases are considered hereafter.

Case 1: PNA in the web of the steel section ($y_1 > D_{tube}$)

In the compression zone, the forces can be divided into three regions, as shown in Fig. 3.10, represented by F_{c1}, which is the maximum compressive force in the concrete infill, F_{c2}, which is the compressive force in the steel tube and F_{c3}, which is the compressive

force in the compressive region of the web. Each of these forces can be determined using Eqs. 3.21-3.23, respectively, where σ_c is the stress in the confined concrete obtained using Eq. 3.7 and r is the inner radius of the steel tube:

$$F_{c1} = 2\int_{y_1-D_{tube}+t_t}^{y_1-t_t} \sqrt{r^2-(y-y_0)^2} \times \sigma_c \, dy \tag{3.21}$$

$$F_{c2} = 2\left[\int_{y_2}^{y_1-t_t} \sqrt{R^2-(y-y_0)^2} - \sqrt{r^2-(y-y_0)^2} \times f_y dy + \int_{y_1-t_t}^{y_1} \sqrt{R^2-(y-y_0)^2} \times f_y dy + \int_{y_1-D_{tube}+t_t}^{y_2} \sqrt{R^2-(y-y_0)^2} - \sqrt{r^2-(y-y_0)^2} \times f_s dy + \int_{y_1-D_{tube}}^{y_1-D_{tube}+t_t} \sqrt{R^2-(y-y_0)^2} \times f_s dy\right] \tag{3.22}$$

$$F_{c3} = \frac{1}{2} t_w (y_1 - D_{tube}) \times \frac{f_y (y_1 - D_{tube})}{y_2} \tag{3.23}$$

In the tension zone, below the PNA, the total force in the web in tension, F_{t1}, is determined as:

$$F_{t1} = \frac{1}{2} t_w y_2 f_y + t_w \times (h - y_1 - y_2 - t_f) \times f_y \tag{3.24}$$

On the other hand, the tensile force in the bottom flange is calculated as:

$$F_{t2} = b_f t_f f_y \tag{3.25}$$

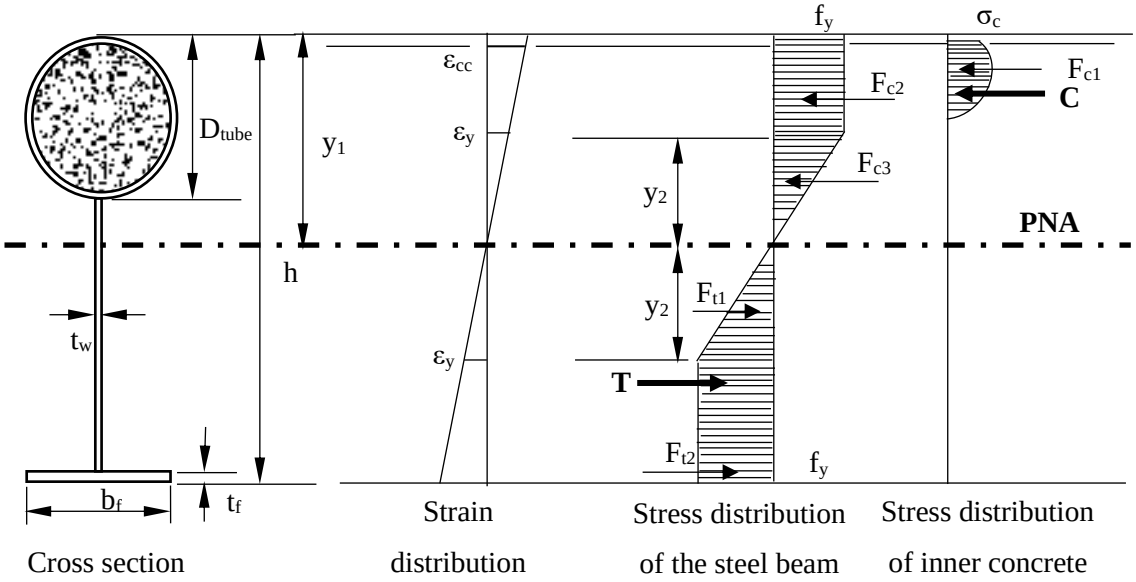

Fig. 3.10 Distributions of strain and stress for Case 1, where the PNA is in the web of the steel section ($y_1 > D_{tube}$)

Case 2: PNA is in the tubular flange ($y_1 < D_{tube}$)

In this case, the total compressive force comprises two components, namely, F_{c1}, which is the force in the infilled concrete above the PNA and F_{c2}, which is force in the steel tube above the PNA. These are determined from Eqs. 3.26 and 3.27, respectively:

$$F_{c1} = 2\int_0^{y_1-t_t}\sqrt{r^2-(y-y_0)^2}\times\sigma_c\,dy \tag{3.26}$$

$$F_{c2} = 2\times\left[\int_{y_2}^{y_1-t_t}\sqrt{R^2-(y-y_0)^2}-\sqrt{r^2-(y-y_0)^2}\times f_y dy + \int_{y_1-t_t}^{y_1}\sqrt{R^2-(y-y_0)^2}\times f_y dy + \int_0^{y_2}\sqrt{R^2-(y-y_0)^2}-\sqrt{r^2-(y-y_0)^2}\times f_s dy\right] \tag{3.27}$$

Below the PNA, there are three components to the total tensile force in the section. As can be seen in Fig. 3.11, y_1 bisects the steel tube, and the tensile force in the steel tube below the PNA (F_{t1}) is calculated as:

$$F_{t1} = 2\times\left[\int_{-(D_{tube}-t_t-y_1)}^{0}\sqrt{R^2-(y-y_0)^2}-\sqrt{r^2-(y-y_0)^2}\times f_s dy + \int_{-(D_{tube}-y_1)}^{-(D_{tube}-t_t-y_1)}\sqrt{R^2-(y-y_0)^2}\times f_s dy\right] \tag{3.28}$$

Eq. 3.29 is used to calculate the tensile force for both the triangular and rectangular plastic stress distribution block areas of the steel web, below the PNA, as illustrated in Fig. 3.11:

$$F_{t2} = \int_{-y_2}^{y_1-D_{tube}} t_w\times f_s d_y + (h-y_1-y_2-t_f)\times t_w\times f_y \tag{3.29}$$

Finally, the tensile force in the bottom flange is:

$$F_{t3} = b_f t_f f_y \tag{3.30}$$

For both Case 1 and Case 2, F_{ci} (i=1, 2, 3,…, etc.) is any compressive force which exists above the PNA and F_{ti} (i=1, 2, 3,…, etc.) is any tensile force which exists below the PNA. C and T are the total compression and tension forces in the CCFTFG, determined from:

$$C = \sum F_{ci} \text{ and} \tag{3.31}$$

$$T = \sum F_{ti} \tag{3.32}$$

In order to maintain equilibrium, the total compressive force (C) must equal the total tensile force (T) in the cross-section.

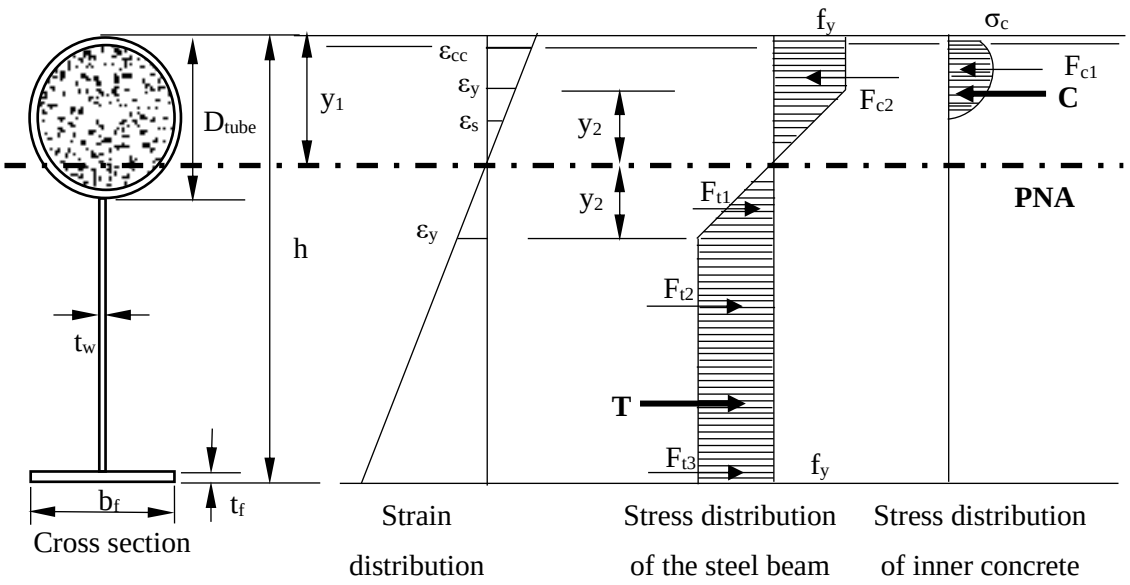

Fig. 3.11 Distributions of strain and stress for Case 2, where the PNA is in the tubular flange section ($y_1 < D_{tube}$)

3.7.2 Ultimate moment capacity

For both cases described in the previous section, the ultimate bending capacity (M_u) for a CCFTFG can be derived based on equilibrium of internal forces in the cross-section, as given in Eq. (3.33):

$$M_u = \sum M_{ci} + \sum M_{ti} \quad (i=1, 2, 3\ldots \text{ etc}) \tag{3.33}$$

The moment generated by the compressive and tensile forces (M_c and M_t, respectively) are found using Eqs. 3.34 and 3.35 for Case 1:

$$\begin{aligned} M_c = 2 \times \Big[& \int_{y_1 - D_{tube} + t_t}^{y_1 - t_t} \sqrt{r^2 - (y - y_0)^2} \times \sigma_c \times y\,dy + \\ & \int_{y_2}^{y_1 - t_t} \sqrt{R^2 - (y - y_0)^2} - \sqrt{r^2 - (y - y_0)^2} \times f_y \times y\,dy + \\ & \int_{y_1 - t_t}^{y_1} \sqrt{R^2 - (y - y_0)^2} \times f_y \times y\,dy + \int_{y_1 - D_{tube} + t_t}^{y_2} \sqrt{R^2 - (y - y_0)^2} - \\ & \sqrt{r^2 - (y - y_0)^2} \times f_s \times y\,dy + \int_{y_1 - D_{tube}}^{y_1 - D_{tube} + t_t} \sqrt{R^2 - (y - y_0)^2} \times f_s \times y\,dy \Big] \end{aligned} \tag{3.34}$$

$$\begin{aligned} M_t = & \frac{1}{2} t_w y_2 f_y \times \frac{2}{3} y_2 + t_w \times (h - y_1 - y_2 - t_f) \times f_y \times \frac{(h - y_1 - y_2 - t_f)}{2} + \\ & b_f t_f f_y \times (h - y_1 - \frac{t_f}{2}) \end{aligned} \tag{3.35}$$

For Case 2, Eqs. 3.36 and 3.37 represent the moments above (M_c) and below (M_t) the PNA:

$$M_c = 2 \times \left[\int_0^{y_1 - t_t} \sqrt{r^2 - (y - y_0)^2} \times \sigma_c \times ydy + \int_{y_2}^{y_1 - t_t} \sqrt{R^2 - (y - y_0)^2} - \sqrt{r^2 - (y - y_0)^2} \times f_y \times ydy + \int_{y_1 - t_t}^{y_1} \sqrt{R^2 - (y - y_0)^2} \times f_y \times ydy + \int_0^{y_2} \sqrt{R^2 - (y - y_0)^2} - \sqrt{r^2 - (y - y_0)^2} \times f_s \times ydy\right] \quad (3.36)$$

$$M_t = 2 \times \left[\int_{-(D_{tube} - t_t - y_1)}^{0} \sqrt{R^2 - (y - y_0)^2} - \sqrt{r^2 - (y - y_0)^2} \times f_s ydy + \int_{-(D_{tube} - y_1)}^{-(D_{tube} - t_t - y_1)} \sqrt{R^2 - (y - y_0)^2} \times f_s \times ydy\right] + \int_{-y_2}^{y_1 - D_{tube}} t_w \times f_s \times yd_y + (h - y_1 - y_2 - t_f) \times t_w \times f_y \times ((h - y_1 - y_2 - t_f) \quad (3.37)$$

The flow chart of the procedure for calculating the position of the plastic neutral axis and the bending moment capacity for case 1 as well as case 2 is shown in Fig. 3.12a and b, respectively. In order to check the validity of the proposed theoretical equations, Table 3.3 presents a comparison between the calculated ultimate moment capacity ($M_{u,Calc}$) and both the experimental value ($M_{u,Exp}$) (Wang et al., 2008) and the FE prediction using the model described previously ($M_{u,FE}$). For this beam, the PNA is found to be in the tubular part of the section and therefore the Case 2 formulations are used. The results show that the term y_1, which is the distance from the top of the steel beam to the PNA, is equal to 155.9 mm. It is clear from the table that the analytical expressions provide a good prediction of the moment capacity for this CCFTFG. The comparison of $M_{u,FE}$ and $M_{u,Calc}$ yields a ratio of 0.992.

Table 3.3 Comparisons of numerical, experimental and analytical ultimate strengths

Specimen	$M_{u,Exp}$ (kNm)	$M_{u,FE}$ (kNm)	PNA location, y_1 (mm)	$M_{u,Calc}$ (kNm)	$M_{u,FE}$/ $M_{u,Calc}$
CCFTFG	537.0	540.2	155.9	544.6	0.992

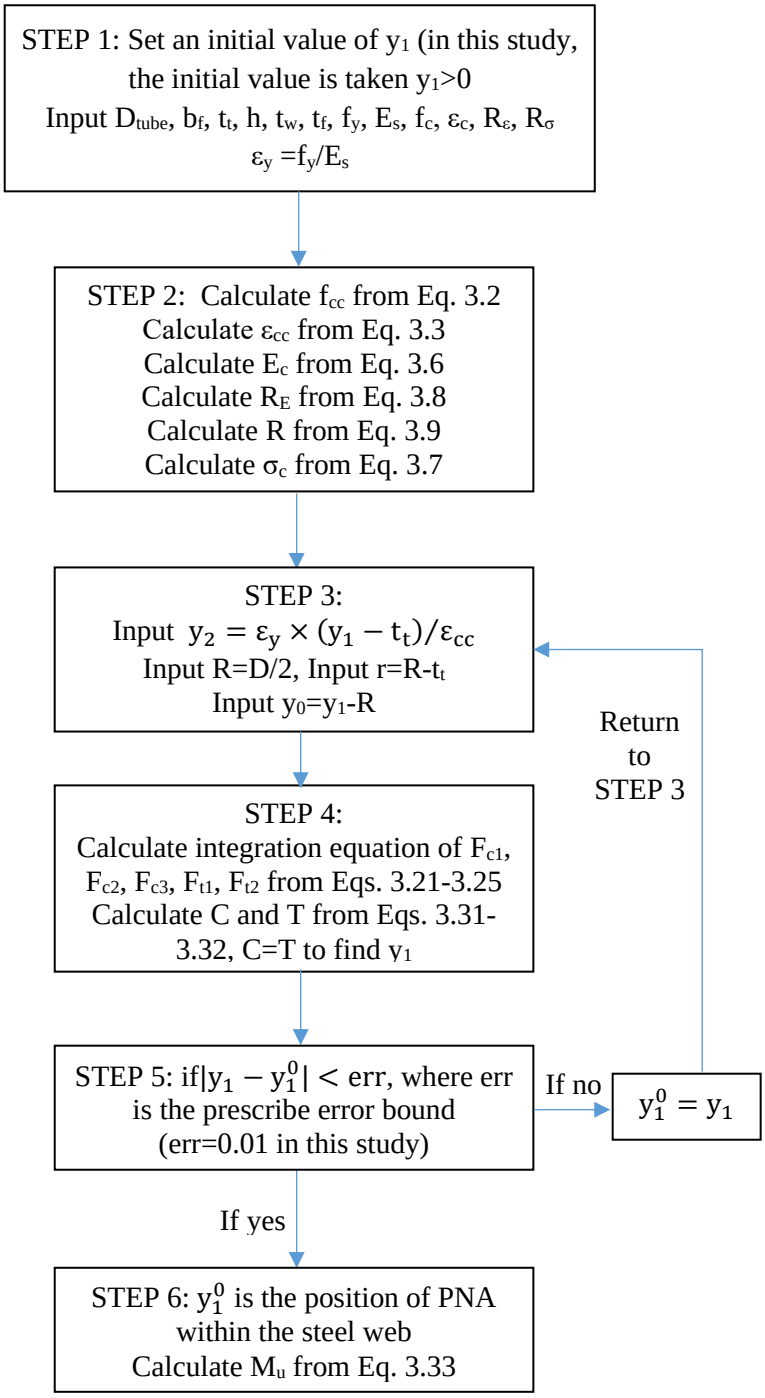
STEP 1: Set an initial value of y_1 (in this study, the initial value is taken $y_1>0$
Input D_{tube}, b_f, t_t, h, t_w, t_f, f_y, E_s, f_c, ε_c, R_ε, R_σ
$\varepsilon_y = f_y/E_s$
STEP 2: Calculate f_{cc} from Eq. 3.2
Calculate ε_{cc} from Eq. 3.3
Calculate E_c from Eq. 3.6
Calculate R_E from Eq. 3.8
Calculate R from Eq. 3.9
Calculate σ_c from Eq. 3.7
STEP 3:
Input $y_2 = \varepsilon_y \times (y_1 - t_t)/\varepsilon_{cc}$
Input R=D/2, Input r=R-t_t
Input y_0=y_1-R
Return to STEP 3
STEP 4:
Calculate integration equation of F_{c1}, F_{c2}, F_{c3}, F_{t1}, F_{t2} from Eqs. 3.21-3.25
Calculate C and T from Eqs. 3.31-3.32, C=T to find y_1
STEP 5: if$|y_1 - y_1^0| < err$, where err is the prescribe error bound (err=0.01 in this study)
If no
$y_1^0 = y_1$
If yes
STEP 6: y_1^0 is the position of PNA within the steel web
Calculate M_u from Eq. 3.33

(a)

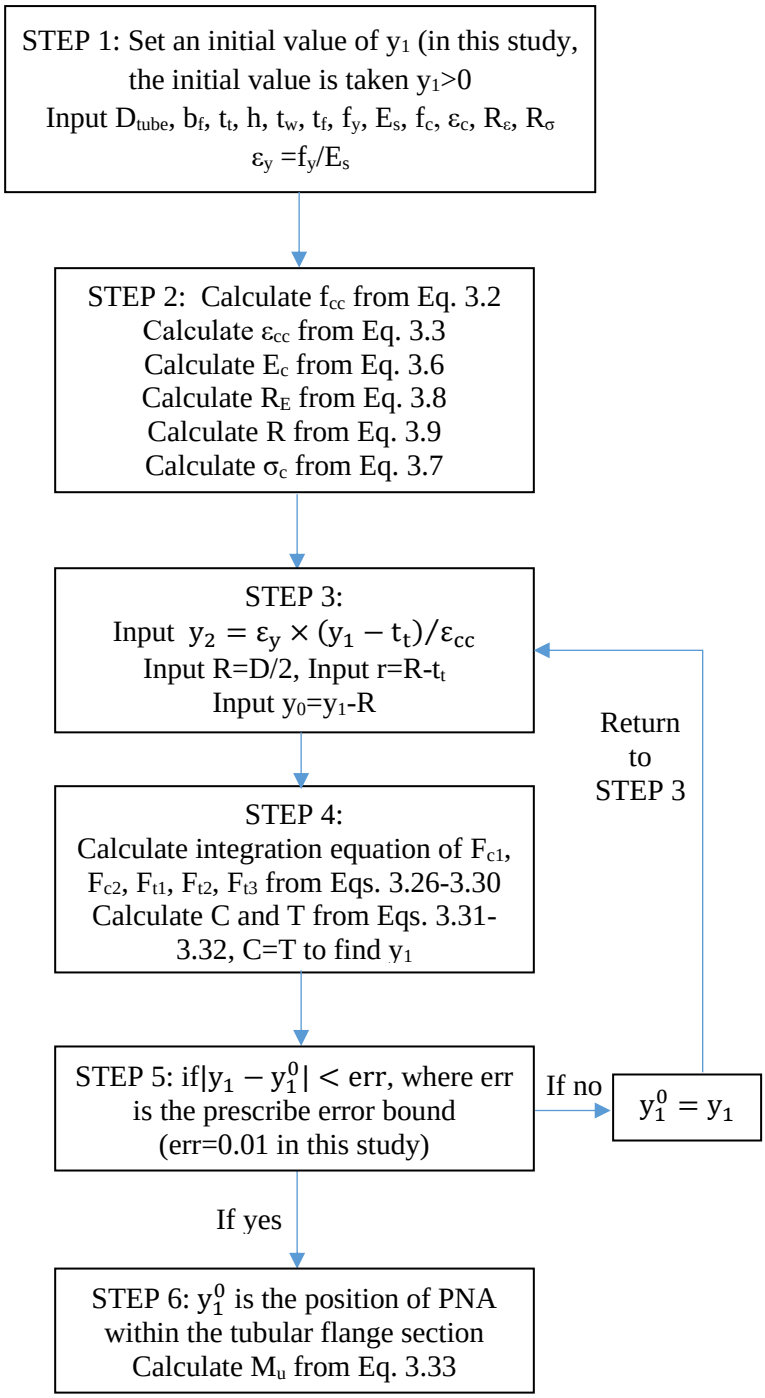

(b)

Fig. 3.12 Flow chart of the solution procedure for (a) case 1, $y_1 > D_f$, (b) case 2, $y_1 < D_f$

3.8 Parametric study

As previously stated, the experimental data available for CCFTFGs is limited to a single test (Wang et al., 2008), mainly owing to the expense associated with large-scale experiments as well as the novelty of these types of structural section. Therefore, a detailed analysis of the behaviour and performance criteria requires the use of numerical and/or analytical tools. In this section, the finite element model and analytical approach previously described are employed to investigate the ultimate behaviour of CCFTFGs and the influence of the most salient parameters on their performance.

A number of parameters are investigated in the parametric study including geometrical and material details. In addition, FE models for steel tubular flange girders (STFGs) are generated in order to study the influence of the concrete infill on the behaviour. For CCFTFGs, buckling takes place in the lateral-torsional mode as the web becomes stiffened transversally at the mid-span location, causing lateral buckling to dominate, rather than the web distortions; Fig. 3.13 shows the buckling mode of the tested girders. A total of 88 different arrangements are considered in this study, as presented in Tables 3.4-3.7. For clarity, in the current section, the results are presented in two general categories: (i) members with different tube diameters (Table 3.4 and 3.5 for CCFTFGs and STFGs, respectively) and (ii) beams with various tube thicknesses (Table 3.6 for CFTFGs and Table 3.7 for STFGs). In all cases, the webs of the girders are transversally stiffened with double-sided flat plate stiffeners which are 12 mm in thickness and located at the support and loading locations. The distance between the two intermediate stiffeners in the girder (a) is 1500 mm. All modelled beams had a length of 4300 mm. All specimens listed in Tables 3.4 and 3.6 contain concrete infill with a compressive strength of 38.6 MPa. In addition, combined yielding and torsional buckling is the failure mode for all models. This type of failure is common for these types of girders (Hassanein, 2015; Kim and Sause, 2005).

In the specimens listed in Tables 3.4 and 3.5, models with five different tube diameters (D_{tube} = 180, 200, 210, 219 and 300 mm) are considered. For each model, two web heights (h_w = 267 and 500 mm), giving two different panel aspect ratios (a/h_w = 5.62 and 3) and two flange thicknesses (t_f = 14 and 28 mm) are considered. The tube and web thicknesses are kept fixed at 8 mm and 6 mm, respectively.

In the specimens listed in Tables 3.6 and 3.7, models with three different tube thicknesses (t_t = 5, 8 and 10 mm) are considered. For each model, two different web heights (h_w =

267 and 500 mm) and two different web thicknesses (t_w = 6 and 10 mm), giving two different panel aspect ratios (a/h_w = 5.62 and 3) and four different web slenderness values ($\bar{\lambda}_w$ or h_w/t_w = 44.5, 26.7, 83.3 and 50), and two flange thicknesses (t_f = 14 and 28 mm) are considered. The tube diameter is kept fixed at 219 mm.

The ultimate moments determined using the FE model $M_{u,FE}$ and the analytical expressions $M_{u,Calc}$ are presented in Tables 3.4-3.7, together with the location of PNA measured from the top of the section (y_1). The results generally show that each pair of CFTFGs and STFGs (i.e. identical properties apart from the inclusion of concrete) has similar buckling shapes but the buckling load of the CCFTFGs is higher than that of the corresponding STFGs. For example, the buckling loads of GR13 and GR33, which are a CFTFG and STFG, respectively, are 540.2 kNm and 391.2 kNm. This equates to a 38% increase in capacity due to the presence of concrete in the tube, which increases the strength and stiffness of the upper flange and hence allows the concrete filled section to carry additional loads.

On the other hand, as expected, girders with a relatively small web panel aspect ratio demonstrate significantly greater ultimate moment capacities compared with members with higher a/h_w ratios. From Tables 3.4 and 3.5, it is seen that the ultimate moment of GR15 is 842.5 kNm while for GR35 it is 650.8 kNm. These girders are identical to GR13 and GR33 previously discussed except that GR15 and GR35 have a web panel aspect ratio of 3 whereas GR13 and GR33 have an equivalent value of 5.62. The ultimate moment capacity is 56% greater for GR15 relative to GR13 whereas the same increase is 66% for GR35 compared with GR33. This demonstrates that irrespective of the presence of concrete, the aspect ratio of the web panel is highly influential to the load-bearing capacity of the girder.

In the following sub-sections, the load-deflection and failure behaviour of both CCFTFGs and STFGs with different key parameters are presented and discussed in detail. Typically, each parameter is varied in isolation while the others are kept constant in order to study the effect of this term.

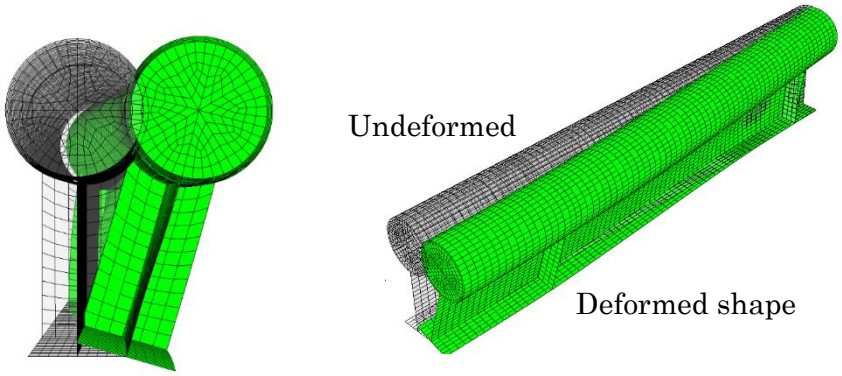

Fig. 3.13 View of the finite element model in both the deformed and undeformed shapes

Table 3.4 Details of CCFTFGs with different tube diameters

CCFTFG Group	Specimen	Geometric details					$M_{u,FE}$ (kNm)	$M_{u,Calc}$ (kNm)	PNA location, y_1 (mm)	$M_{u,FE}/M_{u,Calc}$
		L (mm)	D_{tube} (mm)	h_w (mm)	a/h_w	t_f (mm)				
G1	GR1	4300	180	267	5.62	14	439.7	454.3	137.1	0.968
	GR2					28	650.5	667.2	152.4	0.975
	GR3			500	3	14	744.0	758.4	146.7	0.981
	GR4					28	1010.8	1023.7	166.3	0.987
G2	GR5		200	267	5.62	14	482.1	494.6	146.8	0.975
	GR6					28	703.1	717.2	160.9	0.980
	GR7			500	3	14	793.5	805.4	155.8	0.985
	GR8					28	1062.9	1073.5	172.6	0.990
G3	GR9		210	267	5.62	14	504.1	513.6	151.6	0.981
	GR10					28	729.9	738.1	165.2	0.989
	GR11			500	3	14	818.8	824.5	160.4	0.993
	GR12					28	1089.5	1094.9	176.3	0.995
G4	GR13		219	267	5.62	14	540.2	544.6	155.9	0.992
	GR14					28	754.9	760.3	169.2	0.993
	GR15			500	3	14	842.5	845.9	164.4	0.996
	GR16					28	1117.1	1121.2	179.7	0.996
G5	GR17		300	267	5.62	14	730.3	735.8	189.7	0.992
	GR18					28	1002.4	1008.7	202.2	0.994
	GR19			500	3	14	1079.3	1082.4	197.8	0.997
	GR20					28	1366.0	1363.7	211.4	0.999

a:distance between two intermediate transversally stiffeners

Table 3.5 Details of STFGs with different tube diameters

STFG Group	Specimen	Geometric details					$M_{u,FE}$ (kNm)	$M_{u,Calc}$ (kNm)	PNA location, y_1 (mm)	$M_{u,FE}/M_{u,Calc}$
		L (mm)	D_{tube} (mm)	h_w (mm)	a/h_w	t_f (mm)				
G6	GR21	4300	180	267	5.62	14	342.9	357.7	157.6	0.959
	GR22					28	490.1	505.3	303.3	0.970
	GR23			500	3	14	615.9	629.4	244.8	0.979
	GR24					28	806.4	815.5	419.8	0.989
G7	GR25		200	267	5.62	14	348.4	361.1	151.8	0.965
	GR26					28	499.4	513.0	281.4	0.973
	GR27			500	3	14	613.3	625.7	222.9	0.980
	GR28					28	833.0	840.8	397.9	0.991
G8	GR29		210	267	5.62	14	379.5	392.2	146.8	0.968
	GR30					28	548.9	562.7	270.3	0.976
	GR31			500	3	14	633.1	645.2	211.9	0.981
	GR32					28	875.2	882.6	386.8	0.992
G9	GR33		219	267	5.62	14	391.2	400.8	140.0	0.976
	GR34					28	569.0	580.7	260.6	0.980
	GR35			500	3	14	650.8	663.4	202.1	0.981
	GR36					28	905.8	911.1	377.1	0.994
G10	GR37		300	267	5.62	14	492.8	498.8	114.8	0.988
	GR38					28	665.9	672.2	171.9	0.991
	GR39			500	3	14	756.2	760.5	142.7	0.994
	GR40					28	1173.5	1175.4	288.4	0.998

Table 3.6 Details of CCFTFGs with different tube thicknesses

CCFTFG Group	Specimen	Geometric details							$M_{u,FE}$ (kNm)	M_{uCalc} (kNm)	PNA location, y_1 (mm)	$M_{u,FE}/M_{u,Calc}$
		L (mm)	D_{tube} (mm)	h_w (mm)	a/h_w	h_w/t_w	D_{tube}/t_t	t_f (mm)				
G11	GR41	4300	219	267	5.62	44.5	43.8	14	463.2	477.3	154.2	0.970
	GR42							28	691.3	707.7	183.5	0.977
	GR43						27.4	14	540.2	544.6	155.9	0.992
	GR44							28	754.9	760.3	169.2	0.993
	GR45						21.9	14	557.2	560.7	157.6	0.994
	GR46							28	789.9	793.7	167.8	0.995
G12	GR47					26.7	43.8	14	538.1	552.7	167.8	0.974
	GR48							28	754.2	769.3	197.5	0.980
	GR49						27.4	14	599.8	603.2	164.2	0.994
	GR50							28	824.0	828.9	178.0	0.994
	GR51						21.9	14	634.7	638.3	164.3	0.994
	GR52							28	859.8	863.4	174.9	0.996
G13	GR53			500	3	83.3	43.8	14	786.4	800.8	172.7	0.982
	GR54							28	1058.3	1069.3	209.8	0.990
	GR55						27.4	14	842.5	845.9	164.4	0.996
	GR56							28	1117.1	1121.2	179.7	0.996
	GR57						21.9	14	874.3	878.7	164.2	0.995
	GR58							28	1152.8	1157.3	175.6	0.996
G14	GR59					50	43.8	14	968.7	985.2	201.5	0.983
	GR60							28	1300.3	1312.6	274.1	0.991
	GR61						27.4	14	1035.3	1039.0	179.7	0.996
	GR62							28	1377.2	1381.1	197.8	0.997
	GR63						21.9	14	1069.4	1074.5	176.2	0.995
	GR64							28	1413.2	1417.7	189.2	0.997

Table 3.7 Details of STFGs with different tube thicknesses

STFG Group	Specimen	Geometric details							$M_{u,FE}$ (kNm)	$M_{u,Calc}$ (kNm)	PNA location, y1 (mm)	$M_{u,FE}/M_{u,Calc}$
		L (mm)	D_{tube} (mm)	h_w (mm)	a/h_w	h_w/t_w	D_{tube}/t_t	t_f (mm)				
G15	GR65	4300	219	267	5.62	44.5	43.8	14	292.9	306.9	247.4	0.954
	GR66							28	308.9	322	422.4	0.959
	GR67						27.4	14	391.2	400.8	140	0.976
	GR68							28	569.0	580.7	260.6	0.980
	GR69						21.9	14	435.1	444.9	107.6	0.978
	GR70							28	604.9	613.6	155.3	0.986
G16	GR71					26.7	43.8	14	301.4	310.1	289.4	0.972
	GR72							28	314.2	322.9	394.4	0.973
	GR73						27.4	14	431.1	443.6	192.7	0.972
	GR74							28	557.9	572.1	297.4	0.975
	GR75						21.9	14	480.8	488.2	129.1	0.985
	GR76							28	643.1	648.9	234.2	0.991
G17	GR77			500	3	83.3	43.8	14	334.9	343.4	363.7	0.976
	GR78							28	396.1	404.9	538.9	0.978
	GR79						27.4	14	650.8	663.4	202.1	0.981
	GR80							28	905.8	911.1	377.1	0.994
	GR81						21.9	14	718.6	726.9	116.8	0.988
	GR82							28	946.4	952.6	271.4	0.994
G18	GR83					50	43.8	14	360.3	368	405.9	0.979
	GR84							28	428.2	436.3	510.7	0.981
	GR85						27.4	14	722.3	735.6	308.9	0.982
	GR86							28	942.7	954.6	413.8	0.988
	GR87						21.9	14	840.3	848.6	245.6	0.990
	GR88							28	1029.9	1034.8	350.7	0.995

3.8.1 Effect of specimen geometry

In this section, the effect of a number of the most salient individual geometric properties such as tube diameter (D_{tube}), tube thickness (t_t) and tension flange thickness (t_f) are studied. Firstly, the influence of the diameter of the tubular flange (D_{tube}) is investigated by varying this dimension between 180 and 300 mm, while the thickness of the tube remains fixed at 8 mm. The moment-deflection results are presented in Fig. 3.14 for (a) CCFTFGs and (b) STFGs, and it is evident that in both cases, increasing the diameter of the tubular flange raises the ultimate flexural strength of the girder. This is more significant for the concrete filled members compared with the bare steel sections owing to the increased strength and stiffness resulting from the concrete infill. There is some difference in the general shape of the curves presented in Fig. 3.14 with the concrete filled members showing a more rounded moment-deflection response with no softening whilst the STFGs demonstrate a descending branch after the peak moment has been reached, particularly for GR37. This is attributed to the fact that the concrete filled members do not experience local buckling even at high levels of deflection, due to the confinement effect provided by the concrete core. It is noteworthy that all of the sections in the current study were examined for local buckling using the requirement described in the AASHTO design specifications (1998), and given as:

$$\frac{D_{tube}}{t_t} \leq 2.8\sqrt{\frac{E_s}{f_y}} \tag{3.38}$$

Eq. 3.38 was originally developed based on an unfilled tube although the AASHTO specification recommends using the expression for concrete filled tubes also.

Fig. 3.15 presents the moment-deflection responses for (a) CCFTFGs and (b) STFGs with different D_{tube}/t_t ratios and it is observed that decreasing the tube diameter to thickness ratio, by either reducing D_{tube} or increasing t_t, has the effect of increasing the moment capacity of the girders for both concrete filled and bare steel members. For the STFGs, this is expected as a lower D_{tube}/t_t ratio corresponds to a stockier compression flange, which is less susceptible to local buckling, and does not limit the cross-section flexural resistance of the compression flange. This effect is less prominent for the CCFTFGs, as the confinement effect offered by the concrete infill has a greater effect in improving the local buckling resistance of the compression flange tube of all D_{tube}/t_t ratios. The ratio limits depend on the AASHTO design specifications (1998), as given in Eq. 3.38.

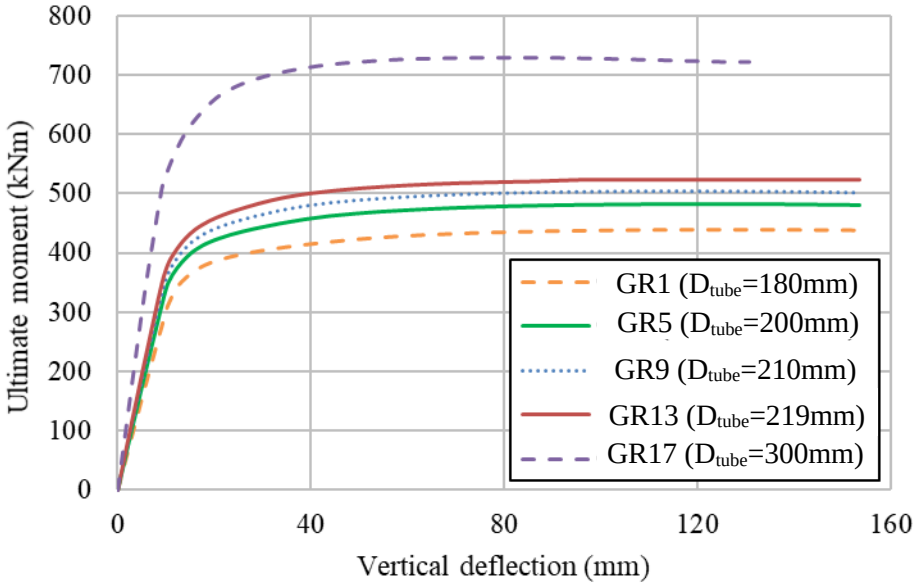

(a)

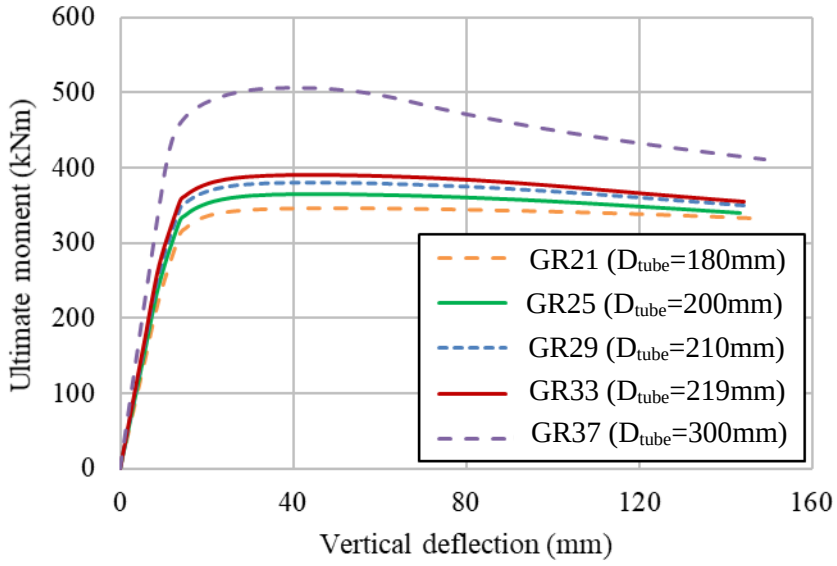

(b)

Fig. 3.14 Ultimate moment versus deflection responses for (a) CCFTFGs (b) STFGs with different tube diameters

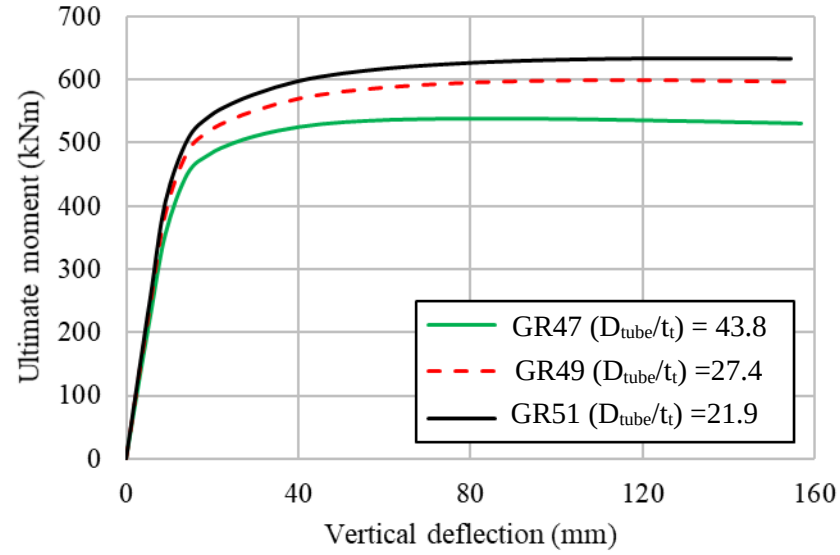

(a)

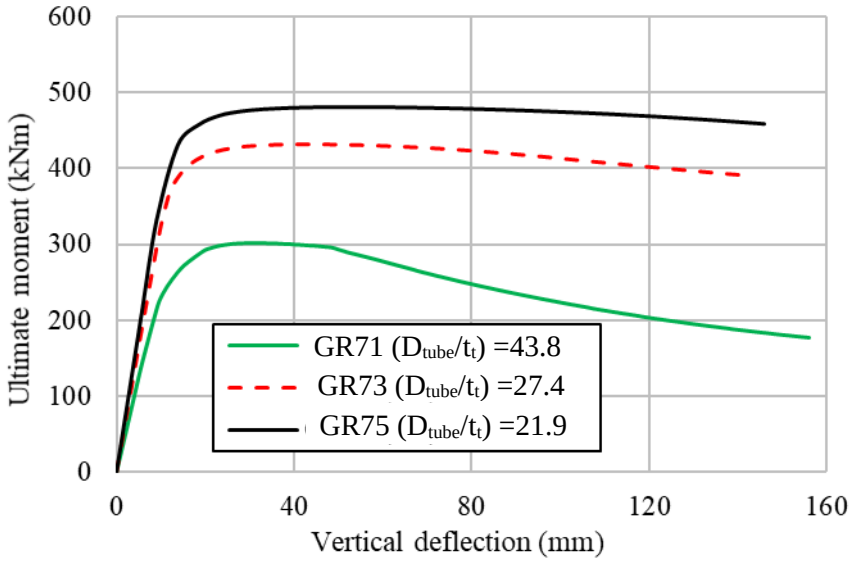

(b)

Fig. 3.15 Ultimate moment versus deflection responses of (a) CCFTFGs (b) STFGs with different D_{tube}/t_t ratios

In order to investigate the effect of plate thickness in the tension region of the cross-section on the behaviour, two different thicknesses of the bottom flange t_f are studied. The moment-deflection curves presented in Fig. 3.16 verify that, as expected, increasing the tensile flange thickness raises the ultimate moment capacity of the section. From a cost perspective (both materials and fabrication), it is important to consider whether the increased volume of steel required in GR64 compared to GR63, for example, is translated into improved moment capacity. These two beams have an ultimate moment capacity of around 1413.2 kNm and 1069.4 kNm, respectively, and a gross cross-sectional area (steel only) of 11901 and 9801 mm^2, respectively. Therefore, a 21% increase in steel volume can result in a 32% improvement in bending moment capacity, for the same stiffener

arrangement. This effect is again examined in this section taking into account the web depth (h_w), which is a key parameter to consider in the design of plate girders. Clearly, decreasing the web depth (h_w) reduces the volume of steel in the section as well as the fabrication costs as less welding is required and the associated risk of weld distortion is lowered. However, it also reduces the bending moment capacity. Therefore, this discussion highlights the importance of a careful consideration of all factors (capacity requirements, flange depth, web depth, welding needs, etc.) when designing a CCFTFG.

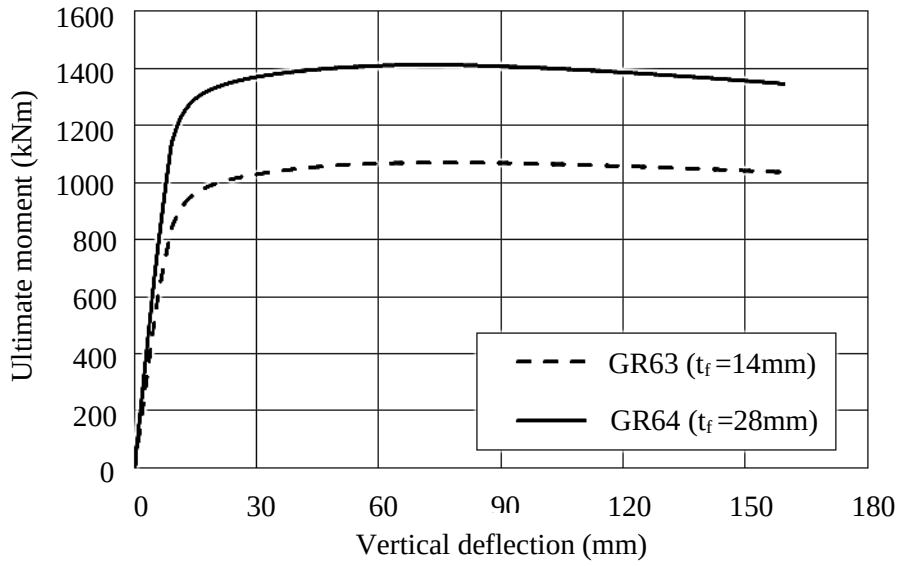

(a)

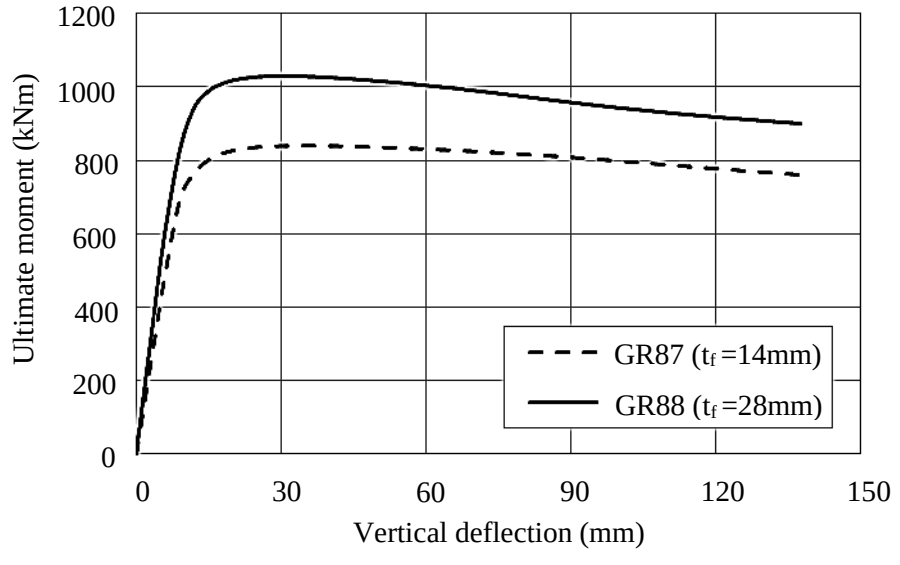

(b)

Fig. 3.16 Ultimate moment versus deflection responses for (a) CCFTFGs (b) STFGs with different bottom flange thicknesses

3.8.2 Effect of web panel aspect ratio

As previously observed in Tables 3.4-3.7, decreasing the aspect ratio of the web panels (a/h_w) for the same girder geometries leads to an increase in the ultimate moment capacity of the tubular flange girders. The ultimate moment-deflection curves for GR13 and GR15 are presented in Fig. 3.17 to illustrate the difference in their general behaviour. After the linear elastic stage, and until reaching the full strength of the girders, the girder with the higher web panel aspect ratio reaches the inelastic stress stage at a lower deflection relative to GR15 and also achieves a significantly higher moment capacity. This is attributed to the fact that GR13 (with the lower a/h_w ratio of these two beams) possesses a larger buckling resistance and also greater web stiffness, compared with GR15.

Fig. 3.18 presents the variation of $M_{u,FE}/M_{u,Calc}$ for different subgroups of CCFTFGs and STFGs. Each subgroup represents girders with the same length and tube diameter, but other parameters such as h_w, t_f and a/h_w are varied. The results indicate the accuracy of the analytical expressions in predicting the ultimate moment as, in all cases, the $M_{u,FE}/M_{u,Calc}$ ratio is between 0.95 and 1.0. Moreover, the figures show that $M_{u,FE}$ and $M_{u,Calc}$ consistently become closer for members with a relatively large tube diameter and also a lower a/h_w ratio thus indicating the analytical expressions are most accurate in these cases. On the other hand, it can be seen that for both CFTFGs and STFGs, increasing the bottom flange thickness t_f results in the $M_{u,FE}/M_{u,Calc}$ ratio becoming closer to unity for all girders, irrespective of the web panel aspect ratio.

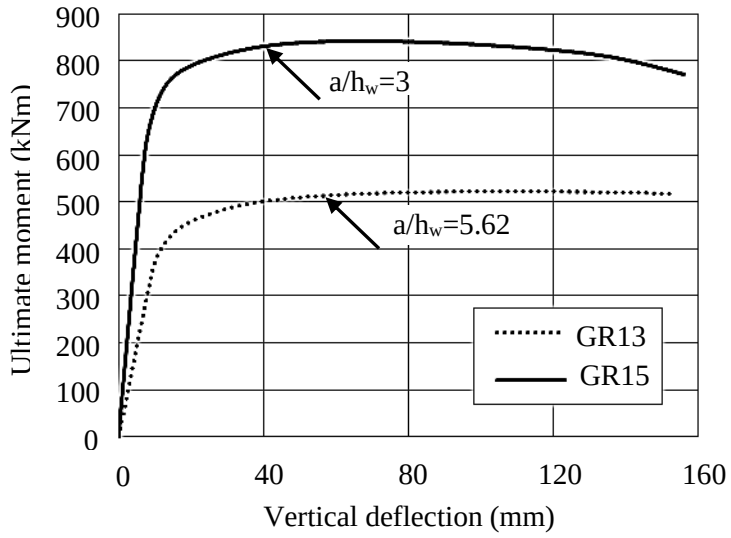

Fig. 3.17 Ultimate moment versus deflection for GR13 and GR15 with difference web panel aspect ratios

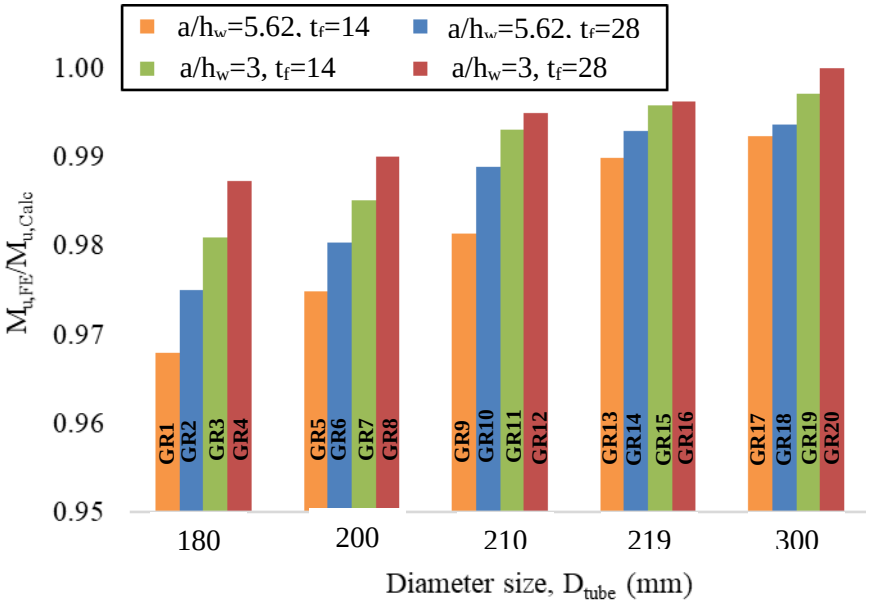

(a)

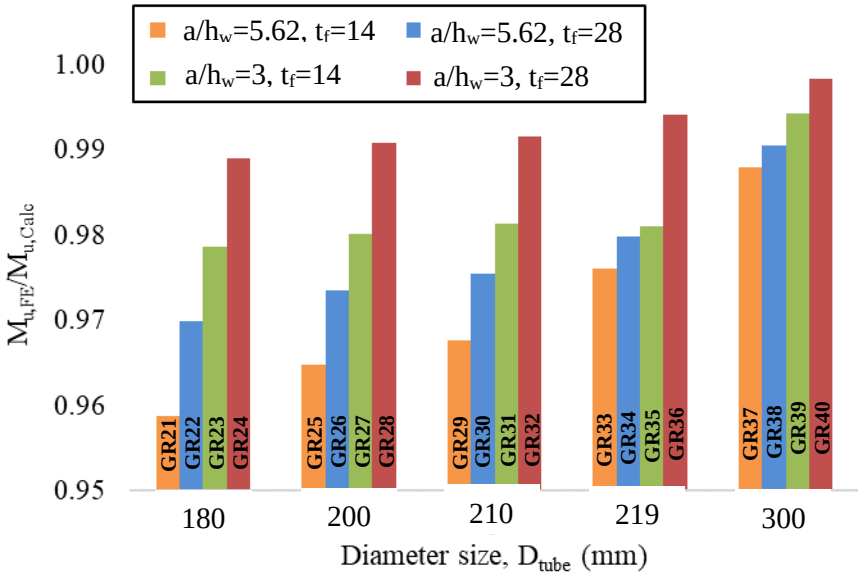

(b)

Fig. 3.18 The relationship between aspect ratio of the web panel (a/h_w) and the $M_{u,FE}/M_{u,Calc}$ ratio for (a) CCFTFGs (b) STFGs

3.8.3 Effect of web plate slenderness

The effect of the web plate slenderness, that is the h_w/t_w ratio, is discussed herein. Fig. 3.19 displays the ultimate moment versus deflection response for (a) CCFTFGs and (b) STFGs, for different web slenderness values. From the figures, together with the data presented in Tables 3.6 and 3.7, it is observed that increasing the web thickness (thereby reducing the h_w/t_w ratio) increases the moment capacity of the CCFTFGs and STFGs, as expected, owing to the increased stiffness of the web plate. This is more pronounced in the concrete filled members (Fig. 3.19(a)) compared with the bare steel flange girders (Fig. 3.19(b)). For example, the ultimate moment of GR55 (h_w/t_w=83.3) is 842.5 kNm whereas the same value for GR61, which is identical apart from the thickness of the web plate (h_w/t_w=50), is 1035.3 kNm. Thus, the increase in web thickness and hence reduction in web plate slenderness for concrete filled members, results in an improved moment capacity of almost 23%. The variation in web thickness from 6 mm to 10 mm increases the cross-sectional area of the section by around 17% (6404 mm^2 for GR55 to 7472 mm^2 for GR 61).

On the other hand, the same values for GR79 and GR85, which are identical to GR55 and GR61 apart from the absence of a concrete infill, are 650.8 and 722.3 kN, respectively, which represents an increase of only 11% for the same variation in web thickness, although the increase in steel volume remains at 17%. For the bare steel sections, although having a thicker web does increase the moment capacity of the section, this is limited to an 11% improvement as failure is likely to be affected by buckling in the top flange before any more capacity can be achieved. However, for the concrete filled members, buckling is extremely unlikely in the top flange owing to the stiffness provided by the concrete core, and therefore the increase in web thickness results in a much more significant improvement in the moment capacity. This illustrates the effect of the concrete infill in terms of overall behaviour and the stiffness provided can be more favourable even than increasing the amount of steel in the section.

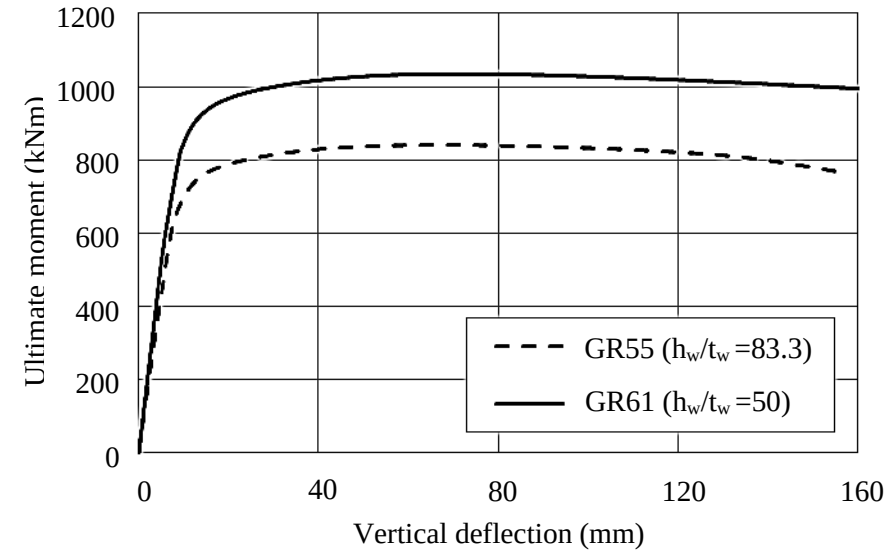

(a)

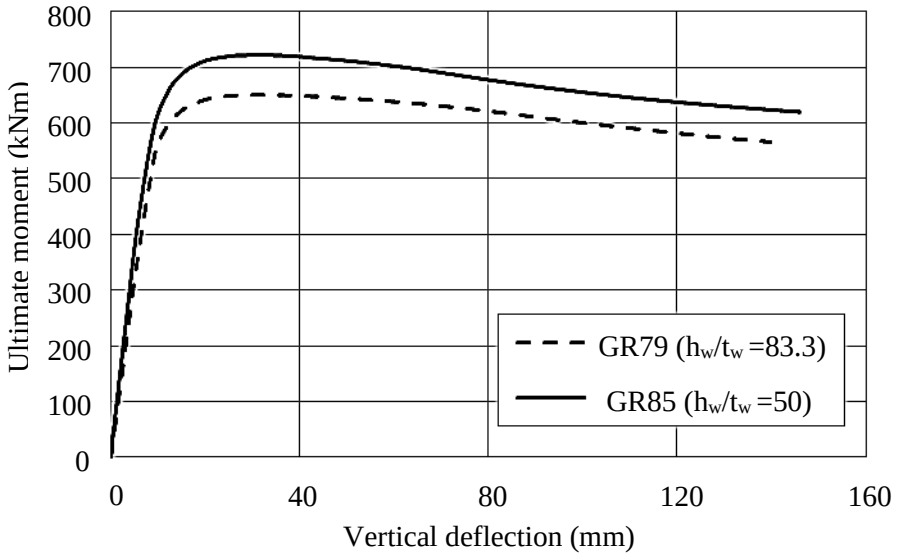

(b)

Fig. 3.19 Ultimate moment versus deflection responses of (a) CCFTFGs (b) STFGs with different web plate slenderness' (h_w/t_w)

3.8.4 Concrete compressive strength

The effect of concrete compressive strength on the response is investigated herein by considering different f_c values ranging from 20 to 70 MPa for specimen GR13, as presented in Table 3.8. The ultimate moment-displacement responses for these members are shown in Fig. 3.20. It can be seen that the value of f_c has a very slight effect on the capacity of the CCFTFGs, which could be ignored. As expected, the moment capacity

increases with greater concrete strengths and the PNA is located at a higher position in the cross-section. From the figure, it is observed that the concrete strength does not have a strong effect on the member rigidity during the elastic stage, where behaviour is controlled by the stiffness rather than strength. From the ratio of $M_{u,FE}$ to $M_{u,Calc}$, as presented in Table 3.8, it is clear that the analytical model provides a more accurate prediction of the moment capacity for relatively low values of f_c, which is expected owing to the diminished contribution made be the concrete in this case. Overall, it can be concluded that the increased strength of the CCFTFGs compared to that of the STFGs is attributed to the availability of a rigid medium in the upper flange rather than the concrete strength, within the range examined herein. Accordingly, it is not necessary to include the compressive strength of the infill concrete in the design strength of the CCFTFGs.

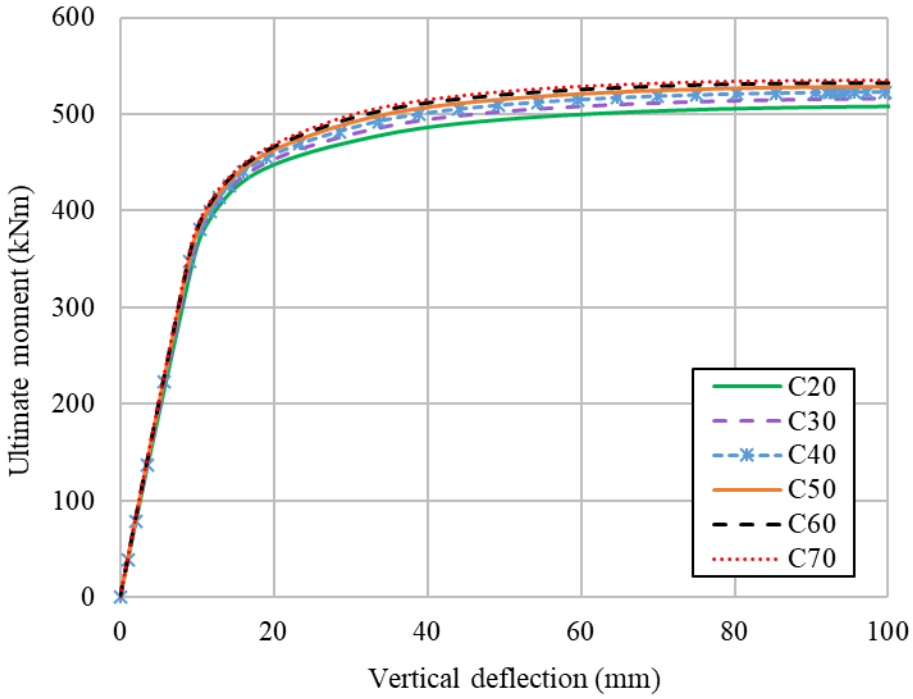

Fig. 3.20 Influence of concrete strength on the behaviour of CCFTFGs

3.8.5 Steel strength

Fig. 3.21 presents the moment-displacement curves for the GR13 CCFTFG but with different yield strengths of steel f_y. The details are also presented in Table 3.8, where it is seen that f_y was varied between 235 to 690 N/mm^2. Fig. 3.21 illustrates that the ultimate bending capacity is proportional to the yield strength of steel, as expected. Also, the steel strength makes almost no contribution to the stiffness of the member in the elastic stage, which is again expected as the Young's modulus value remains constant. The influence

of steel strength on the $M_{u,FE}/M_{u,Calc}$ ratio is also provided in Table 3.8 and it can be seen that the members with higher steel strength also give greater $M_{u,FE}/M_{u,Calc}$ ratios, thus indicating that the analytical model captures the behaviour of these members particularly well.

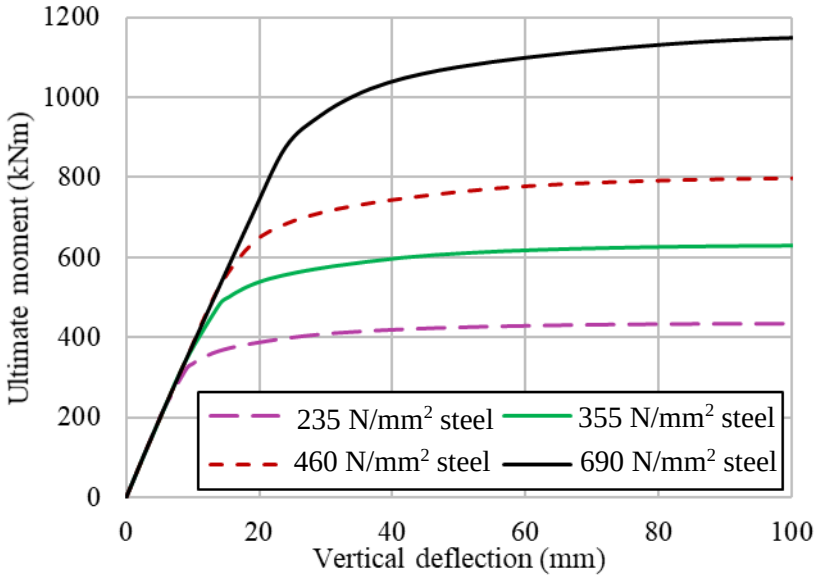

Fig. 3.21 Vertical deflection at mid-span section with different yielding strength of steel

Table 3.8 Influence of f_c and f_y on the capacity of CCFTFG GR13

f_c (MPa)	f_y (N/mm^2)	$M_{u,FE}$ (kNm)	$M_{u,Calc}$ (kNm)	PNA location (mm)	$M_{u,FE}/M_{u,Calc}$
20	287.9	525.5	526.0	168.8	0.999
30	287.9	536.5	539.8	161.2	0.993
38.6	287.9	540.2	544.6	155.9	0.992
40	287.9	545.8	550.9	155.1	0.990
50	287.9	553.1	562.7	150.1	0.983
60	287.9	558.2	569.1	145.9	0.981
70	287.9	561.8	575.6	142.3	0.976
38.6	235	433.7	442.7	154.1	0.978
38.6	355	631.4	638.0	157.6	0.988
38.6	460	799.3	803.1	159.7	0.995
38.6	690	1161.1	1162.4	162.4	0.998

3.9 Concluding remarks

In order to investigate the influence of bridge design parameters such as the size of the tube diameter (D_{tube}), the ratio of the tube diameter to thickness (D_{tube}/t_t), the thickness of the bottom flange (t_f), the web plate slenderness (h_w/t_w), the aspect ratio of the web panel (a/h_w) and also the material strengths. Ultimate moment versus vertical deflection curves and failure modes were obtained from the analyses. Based on this parametric study, the following conclusions can be made:

- The fundamental structural behaviour of CCFTFGs, including the bending moment capacity, plastic neutral axis location (PNA), and yield moment can be accurately estimated using plastic theory of cross-section analyses.
- The lateral displacements of the girders under applied vertical loading are affected by the initial imperfection shapes of both the compression and tension flanges.
- Each pair of CCFTFGs and STFGs with identical properties apart from the presence of concrete were found to have similar buckling shapes with the buckling load of the CFTFGs being higher than that of the corresponding STFGs. This highlights the influence of the infill concrete which increases the stiffness of the upper flange, and hence allows the section to carry additional ultimate moment capacity compared to the STFGs.
- In terms of the geometrical details, it was shown that increasing the bottom flange depth (t_f) is advantageous in terms of moment capacity achieved and also the material costs. This is because the increase in moment capacity achieved is disproportionately large, compared with the increase in the cross-sectional area.
- The concrete compressive strength (f_c) was shown to have almost no effect on the strength and behaviour of CCFTFGs. Hence, the improved strength of CCFTFGs compared to that of equivalent STFGs is attributed to the availability of a rigid concrete medium in the tubular flange. On the other hand, the yield strength of the steel does contribute to the ultimate bending capacity of the girders.

Chapter 4 : Behaviour of concrete filled tubular flange girders under combined loading

4.1 Introduction

Beams in structural frames can often be exposed to combined actions, e.g. continuous or semi-continuous structures, where members are under either positive (sagging) or negative (hogging) bending moments in combination with axial forces. The most efficient use of the materials' strengths occurs when the beam is subjected to positive bending at the mid-span. In this chapter, a finite element (FE) model is described which has been developed using the ABAQUS (Simulia, 2011) software, similar to that described in Chapter 3.

4.2 Research significance and methodology

Large steel beams or girders can be subjected to significant loads and bending moments in practice and failure typically occurs when the applied moment at the critical section exceeds its flexural capacity. Thus, in conventional design, it is important to ensure that the flexural limit state is satisfied before checking other limit states, by examining the flexural capacity and lateral-torsional buckling resistance and also considering the propagation of plastic hinges. For very heavily loaded sections, one of the key causes of premature failure is lateral-torsional buckling, which may occur if the unbraced length of the girder exceeds a given threshold, causing the compression flange to become unstable and buckle laterally prior to reaching the maximum flexural strength. It is desirable to prevent this mode of failure as much as practicably possible and, towards this end, a number of different solutions are available for conventional I-shaped steel girders such as reducing the unbraced length or increasing the flange dimensions. A more recent proposal is to replace the flat compression flange with a hollow tubular flange, which may or may not be filled with concrete to provide additional lateral rigidity (Hassanein and Kharoob, 2013; Hassanein and Silvestre, 2013; Kim and Sause, 2005; Gao et al., 2014).

A concrete-filled tubular flange girder (CFTFG) offers excellent structural characteristics including high strength and stiffness as well as ductility. Fewer stiffeners and diaphragms are needed for CFTFGs to maintain lateral–torsional stability compared to similar I-shaped steel girders, which reduces the fabrication and erection effort required, and also increases the load-carrying capacity (Kim and Sause, 2008). There has been a significant increase in research in this area in recent years, although most of the studies have been limited to hollow tubular flange girders (HTFGs) with fewer investigations into concrete filled members.

Previous studies have investigated the bending resistance of circular CFTFGs and a series of analytical expressions for predicting the location of the plastic neutral axis (PNA) and the ultimate bending capacity (M_u) were proposed (Al-Dujele et al., 2018; Al-Dujele and Cashell, 2019). However, the behaviour of CFTFGs under combined loading has not been previously considered. This is a scenario which occurs frequently in practice such as in continuous or semi-continuous members or, in extreme cases, if a support is removed and the beams are required to withstand high tensile loads to avoid progressive collapse. Full-scale experiments of large circular CFTFGs are extremely challenging and expensive to conduct and therefore a finite element model is developed to investigate the behaviour and is described in the following section.

4.3 Development of the numerical model

A finite element (FE) model has been developed using the commercial software package ABAQUS, which is capable of achieving numerical convergence for complex structural systems such as circular CFTFGs despite the geometric and material nonlinearities of the behaviour. This model is a further advancement of the previous version which was employed to assess CCFTFGs under bending (Al-Dujele et al.,2018) and validated against available test data (Wang et al., 2008).

As stated previously, there is no experimental data available in the literature for CCFTFGs under combined loading. Therefore, the FE model is developed and validated in two stages. First, the traditional composite beam shown in Fig. 4.1 which was subjected to combine bending moments and axial tension in tests conducted and discussed by Vasdravellis et al. (2012a), is analysed to validate the simulation of combined loading conditions. The loading conditions in this study are identical to those under investigation in the current study. Secondly, the modelling of CCFTFGs is validated using the tests completed by Wang et al. (2008) which examined simply supported members under bending only.

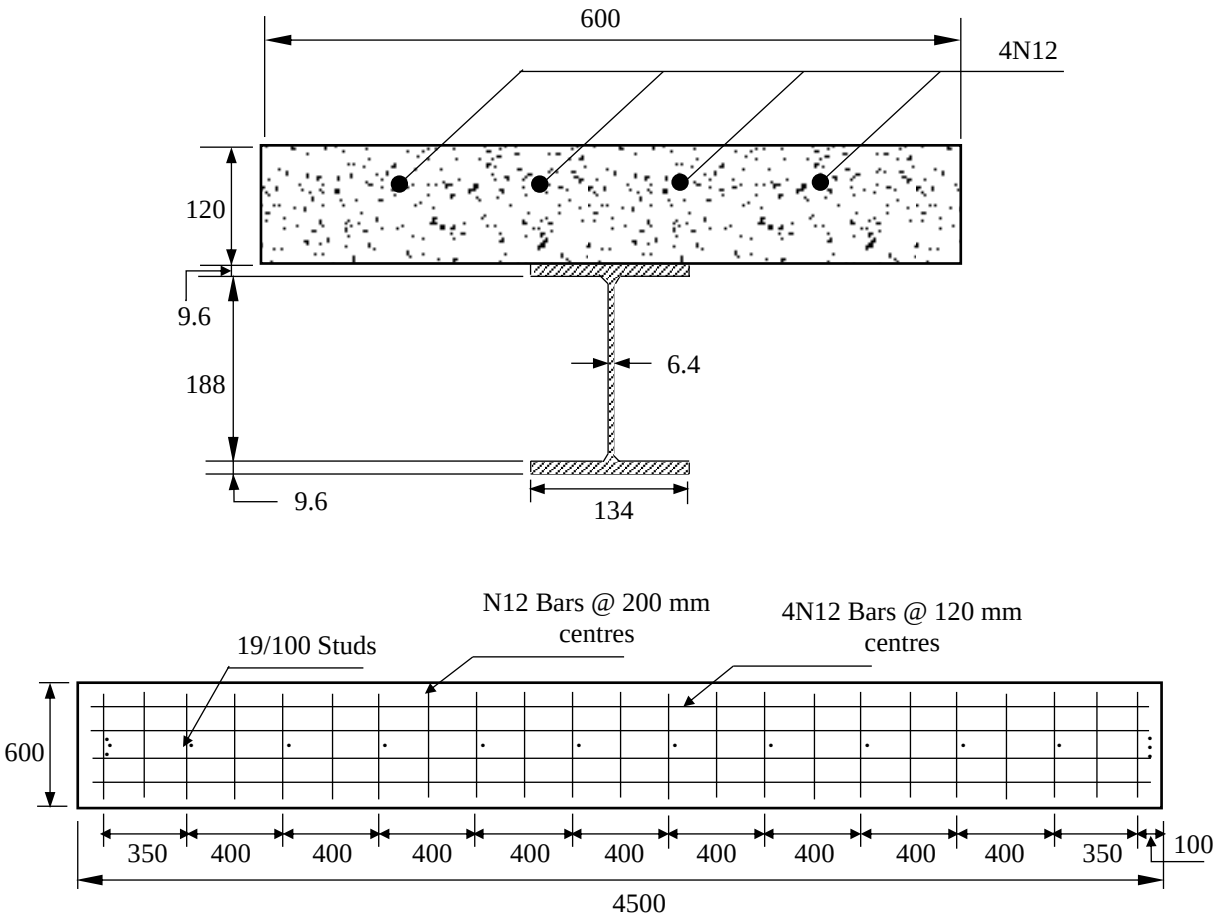

Fig. 4.1 Composite beam cross-section and plan view of slab reinforcement and shear stud layout (all dimensions in mm)

4.3.1 Combined loading

In this sub-section, two of the test specimens examined by Vasdravellis et al. (2012a), which focussed on the behaviour of composite beams under combined bending and axial tension, are employed to validate the numerical approach for these loading conditions. This test programme included four other tests under different loading conditions which are not relevant to the current work. As shown in the schematic presented in Fig. 4.1 and the data given in Table 4.1, the two composite beams were 600 mm in width and comprised a concrete slab which was 120 mm in depth. The slab was connected to the steel section using shear studs which were 19 mm in diameter and 100 mm in length and welded along the centre single line of the top flange of the steel beam. The compressive strength of the concrete was 25 MPa. The results from these experiments are presented in Table 4.2, including the axial and vertical applied loads and the combined bending moment achieved. The following sections provide a detailed description of the geometry of the model, element types, materials and the solution method.

Table 4.1 Specimen details (Vasdravellis et al., 2012a)

Details	Specimens CB1 and CB2
Slab size	4500×600×120 mm
Longitudinal reinforcement	4N12×4450 mm
Transversal reinforcement	550 mm N12 at 400
Shear connectors	19 mm headed studs, 100 mm pre-welded length
Number of studs per beam	12 at 400 mm centres

Table 4.2 Experimental load values, comparison experimental and FE combined bending moment for the tested specimens

Specimen	Experimental values (Vasdravellis et al., 2012a)			FE values
	Axial load, N (kN)	Vertical load, P_v (kN)	Combined bending moment, M_{Exp} (kNm)	Combined bending moment, M_{FE} (kNm)
CB1	−760.5 (51%)*	337	180	185
CB2	−1400 (93%)*	48	47	50

* Percentage of experimental axial force to ultimate axial capacity of beam.

4.3.1.1 Concrete behaviour

The concrete slab is represented using the concrete damaged plasticity (CDP) model, available in the ABAQUS library. This approach offers general analysing capabilities for concrete structures under static, dynamic, monotonic or cyclical loading using the algorithm of damaged plasticity. The material behaviour is defined in terms of the elastic, plastic, compressive and tensile characteristics and assumes that the concrete will either fail in compression, through crushing, or tension by cracking. In the present study, the Poisson's ratio and density of concrete are taken as 0.2 and 2400 kg/m^2, respectively. A number of other parameters, including the dilation angle, flow potential eccentricity and viscosity parameter are required in the CDP model, in addition to the compressive and tensile relationships, and these are assigned values of 36˚, 0.1, and 0, respectively, as used by other researchers for similar work (e.g. Kmiecik and Kamiński, 2011).

In the current analysis, the ratio of the strength in the biaxial state to the strength in the uniaxial state, f_{b0}/f_c, is taken as 1.16 while the ratio of the second stress invariant on the tensile meridian (K) is given as 0.667. The concrete in compression and tension is represented by the models indicated in Eurocode 2 (EN 1992-1-1, 2004), as shown in Fig. 4.2. Accordingly, the compression relationship stress-strain for the concrete (i.e. the σ_c–ε_c relationship) in compression is given as:

$$\sigma_c = \left(\frac{k\propto-\propto^2}{1+(k-2)\propto}\right) f_c, \qquad 0 \le \varepsilon_c \le \varepsilon_{cu1} \tag{4.1}$$

In this expression, σ_c is the compressive stress, ε_{cu1} is the ultimate compressive strain and f_c is compressive strength of concrete. The parameters k and α are given by Eqs. (4.2) and (4.3), respectively, in which ε_{c1} is the strain at the peak stress and E_c is the elastic modulus for concrete:

$$\propto = \frac{\varepsilon_c}{\varepsilon_{c1}} \tag{4.2}$$

$$k = 1.05E_c\frac{\varepsilon_{c1}}{f_c} \tag{4.3}$$

In Eq. (4.3), ε_{c1} (as a percentage) is determined as:

$$\varepsilon_{c1} = 0.7(fc)^{0.31} \leq 2.8 \tag{4.4}$$

The ultimate compressive strain (ε_{cu1}), as a percentage, is given by:

$$\varepsilon_{cu1} = 2.8 + 27[(98 - f_c)/100]^4 \quad \text{for } f_c \geq 50 \text{ N/mm}^2\text{, otherwise } 3.5 \tag{4.5}$$

In addition, at each level of the inelastic stress, the damaged compressive parameter (d_c) must be defined. It varies from zero, for undamaged material, to unit when the material is unable to withstand a load anymore. The value for d_c is obtained only as follows for the descending branch of the compression concrete stress- strain curve, as follows:

$$d_c = \frac{f_c - \sigma_c}{f_c} \qquad \text{when } \varepsilon_c \geq \varepsilon_{c1} \tag{4.6}$$

Tension stiffening refers to the phenomenon that, even after a cracking, concrete carries on some tensile load, although the tensile strength decreases gradually as the tensile strain increases. In this analysis the interaction between the steel reinforcement and the surrounding cement (i.e. bonding) is effectively simulated. In current study, the tensile strength is assumed to decrease linearly to reach zero stress at a strain of 0.01 once the tensile strength of concrete is achieved. Other researchers have used this value (Ban and Bradford, 2013) and allows the analysis to work without any significant number difficulties and without compromising the results ' accuracy. The tensile strength of concrete f_t is taken from Eqs (4.7) and (4.8) in accordance with Eurocode 2 (EN 1992-1-1, 2004).

$$f_t = 0.3 f_c^{\,2/3} \quad \text{for} \quad f_c \leq 50\ \text{N/mm} \tag{4.7}$$

$$f_t = 2.12 \ln(1 + 0.1 f_c) \quad \text{for} \quad f_c > 50\ \text{N/mm}^2 \tag{4.8}$$

Like the simulation of concrete in compression in the CDP model, the tensile damage parameter d_t is defined at each increment of cracking strain, as outlined by Eqs (4.9) and (4.10). The parameter d_t is valid only in the descending branch of the stress-strain curve for concrete in tension.

$$d_t = 0 \quad \text{for} \quad \varepsilon_t < \varepsilon_{cr} \tag{4.9}$$

$$d_t = \frac{f_t - \sigma_t}{f_t} \quad \text{for} \quad \varepsilon_t \geq \varepsilon_{cr} \tag{4.10}$$

4.3.1.2 Steel

A multilinear stress-strain relationship is modelling the steel beam in the composite member, as shown in Fig. 4.3. This relation is defined using the Young's modulus (E), yield stress (f_y), yield strain (ε_y), strain at the onset of hardening (ε_{st}), ultimate stress (f_u) and corresponding ultimate strain (ε_u). The Young's modulus used for the steel was 200 GPa and the yield stress value of 547 was used for the reinforcement. For the steel beam, the yield stress with values 352 and 387 Mpa were used for flange and web, respectively. The ultimate tensile stress of 529, 537, and 641 were used for flange, web and reinforcement, respectively (Vasdravellis et al., 2012a). In order to consider the effects of the decreased section during the tensile test, the stress-train curves included in the FE model are converted into true stress-strain relationships. ABAQUS needs the true stress–strain (σ_{true}-ε_{true}) response which is calculated from the engineering stress-strain (σ_{eng}-ε_{eng}) relationship as follows:

$$\varepsilon_{true} = \ln(1 + \varepsilon_{eng}) \tag{4.11}$$

$$\sigma_{true} = \sigma_{eng}(1 + \varepsilon_{eng}) \tag{4.12}$$

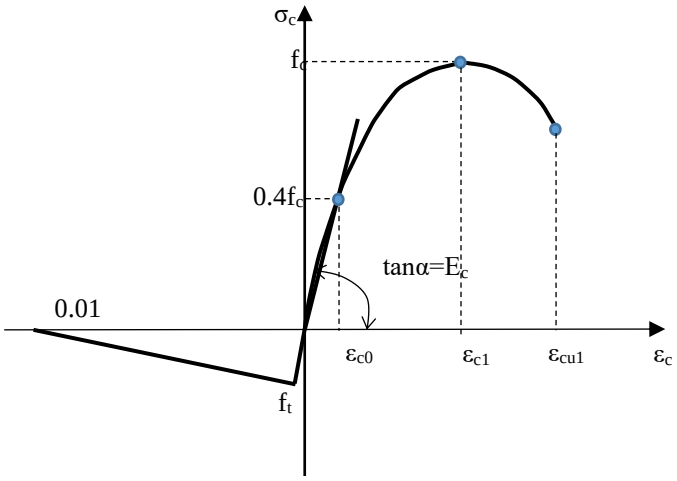

Fig. 4.2 Stress-strain relationship for concrete in compression and tension used for structural analysis, as given in Eurocode 2 (EN 1992-1-1, 2004)

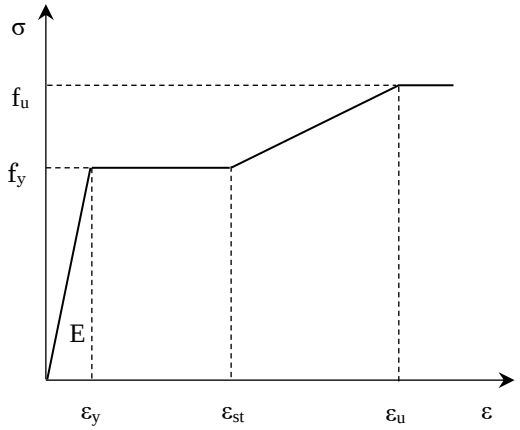

Fig. 4.3 Stress–strain curve of steel beam (reproduced from Ban and Bradford, 2013)

4.3.2 Geometry and element types

In this context, an experimental data point (Vasdravellis et al., 2012a) is used for modelling a three-dimensional FE composite beam with 4500 mm length. The steel beam section as well as the stiffeners are modelled using reduced integration shell element, namely the S4R element in ABAQUS (Simulia, 2011). The reduced integration allows for more efficient computation without compromising results ' accuracy. This element is widely used for construction purposes because as shown in Fig. 4.4 it is suitable for thin and thick shells. In ABAQUS software, the steel reinforcement in the concrete slab is modelled using the rebar layer which is defined by the cross-sectional area of the steel reinforcement, the spacing of the bars as well as the position of the centroid of the reinforcing bars within the depths of the slab and the direction of the bars in the concrete

slab. The concrete slabs are modelled using eight-node solid elements with reduced integration, named C3D8R, while the steel reinforcement is modelled as two-node three-dimensional linear truss elements (namely T3D2 in the ABAQUS library) which are embedded in the slab elements. To represent this variable slab thickness with solid elements are used.

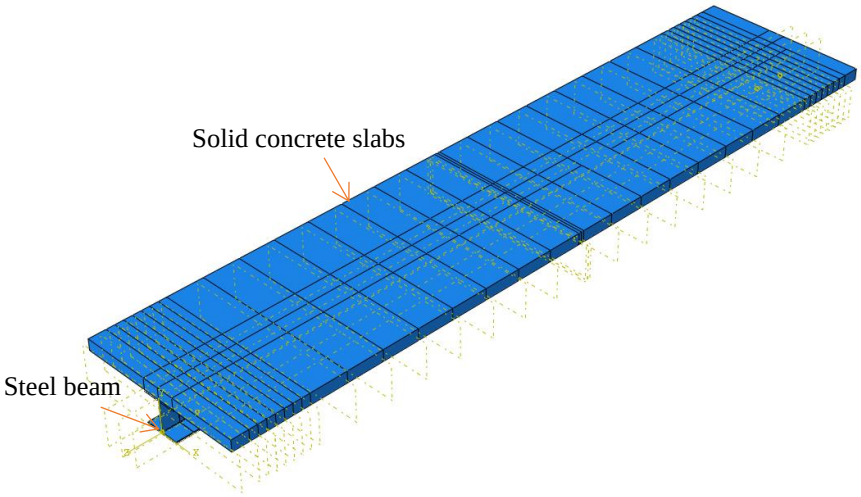

Fig. 4.4 Finite element mesh of the composite beam with solid concrete slab

4.3.3 Modelling of the shear connectors

The shear studs have to be modelled using the ABAQUS library Cartesian connector element as other researchers report (e.g. Kmiecik and Kamiński, 2011; Kwon et al., 2010). These elements connect the node in the flange of the beam with a coincident node in the slab at the connector position. In shear as well as in axial directions the nonlinear behaviour of the connector element is defined. Connector failure is governed by the relative element displacements exceeding a limited slip capacity defined by the user (Δ_u).

The shear connectors ' load-slip relationship is modelled according to the relationship presented by Ollgaard et al., (1971), given as:

$$Q = Q_u(1 - e^{-0.71\Delta})^{2/5} \tag{4.13}$$

where Q is the shear force on the shear stud, Q_u is the ultimate capacity of the shear stud and Δ is the slip in millimetres (see Fig. 4.5). The formula of analysis in Eq. (4.13) are based on the pushout test results performed for the purposes of obtaining the shear connector load-slip curve embedded in a solid concrete slab.

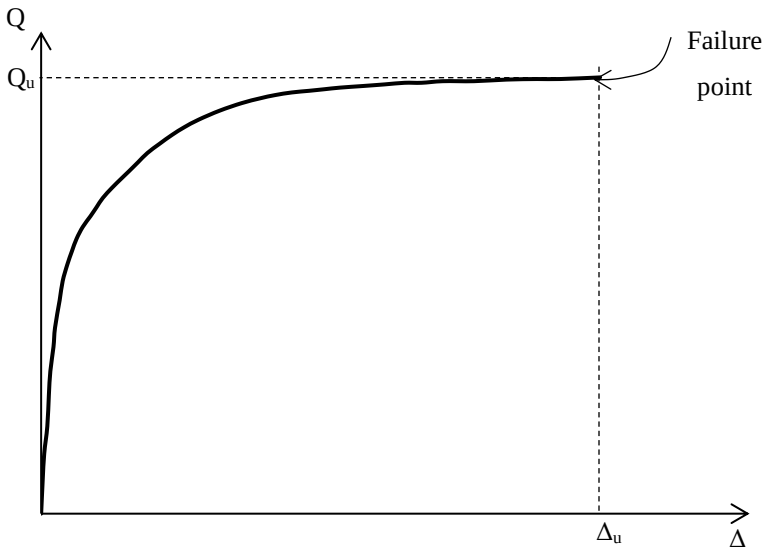

Fig. 4.5 Load-slip relationship of shear connectors

4.3.4 Boundary and loading conditions

In the composite beams, the same loading process as for the experimental beam was applied to simultaneous axial tension and positive bending. Loads are generally applied through concentrated point loads in the model. Simply supported with concentrated point vertical load (P_v) applied at mid-span, operated in displacement-control, in locations along the member which are defined by the user while the tensile load is applied at a reference point in the centre of gravity of the end rigid body steel beam. The contact position is defined as being the boundary between the bottom of the slab and the top surface of the steel beam. A hard friction contact is defined as the property of the contact. Eurocode 4 (EN1994-1-1, 2004) recommends the value 0.5 for the coefficient of friction between steel and concrete in composite members for steel sections without painting; however, the more conservative value 0.4 is assumed. Between the surface of the steel section and the edges of the stiffeners a tie contact is defined. In each direction, the element size of the numerical model is 20 mm.

4.3.5 Solution method

The ABAQUS software provides a range of structural problem solution strategies. An implicate time integration scheme is used by the implicit dynamic solution to calculate the dynamic or quasi-static transitional response of a system. It can be used in quasi-static applications through introducing an inertia effect, which regularizes unstable behaviour

in analyses when the primary focus is a final static response (Simulia, 2011). The resulting moment is calculated taking into account the equilibrium of the external forces acting on the beam. In order to calculate the final bending moment the following equation was used:

$$M = \frac{P_v L}{4} + Ne \tag{4.14}$$

where P_v is the vertical force applied at the centre of the beam, N is the horizontal force applied at reference point, and e is the eccentricity between the location of the horizontal load (N) and the plastic neutral axis of the composite beam.

4.3.6 Validation of the finite element model

The FE model described in the previous section has been validated using available test data (Vasdravellis et al., 2012a). Of this test programme, the test specimen was made using steel beam with solid concrete slab and full details on this test programme is available in publication. It is noteworthy that stiffeners were used in the tested beam at the support and loading positions. The ultimate values of positive combined bending moment versus the corresponding axial tension loads for ABAQUS model are plotted in the interaction diagram of Fig. 4.6. From FE results and the available experimental data points it is observed that the combined moment capacity of the simulated composite beams is in good agreement with the corresponding experimental value. Moreover, the failure modes observed experimentally are well predicted by the FE model including specimens failed by failure of the shear connectors. It is noteworthy that the FE model captures the overall combined moment capacity and failure mode of the test specimen with reasonable accuracy, see Table 4.2.

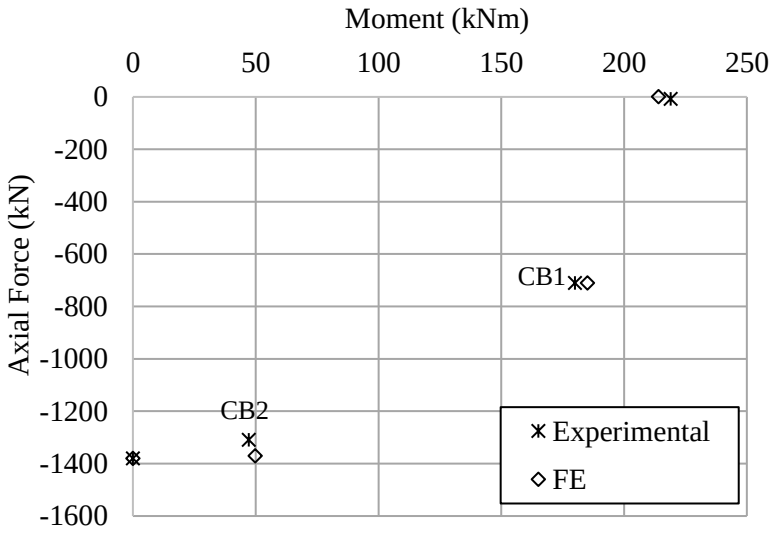

Fig. 4.6 Comparison between bending moment-axial force interaction diagram resulting from the experimental and the FE model

4.4 FE modelling of CCFTFGs

Regarding the good agreement validation result of traditional composite beam, circular concrete filled tubular flange girders (CCFTFGs) are validated herein with the testing carried out by Wang et al. (2008), which examined only bending. Accordingly, the simulated girder is 0.5 m in height and 4.3 m in length, as shown in Fig. 4.7, and is subjected to two concentrated loads (P) in the vertical direction. It is made using Q235 steel and the concrete infill has a compressive strength of 38.6 MPa. The load is applied incrementally and the nonlinear geometry parameter (*NLGEOM, in the ABAQUS library) is included to allow for changes in the geometry under load. The distance between the loading points is 1 m. There are four stiffeners across the span, including one at each of the supports and also at the two loading points, to prevent local instability of the web at these locations. The steel beam and stiffeners are both modelled using the four-noded, three-dimensional shell element with reduced integration (S4R in the ABAQUS library) whereas the concrete infill is represented using 8-noded brick elements with reduced integration, known as C3D8R solid element in the ABAQUS library. The reduced integration enables more efficient computation without compromising the accuracy of the results. A tie contact is defined between the surface of the steel section and the edges of the stiffeners. Following a mesh sensitivity study, it has been found that an element size of 30×30 mm provides the best combination of accuracy and computational efficiency

and therefore is applied to all elements in the model. A briefly description of CCFTFGs modelling can be found in chapter 3 section 3.2.

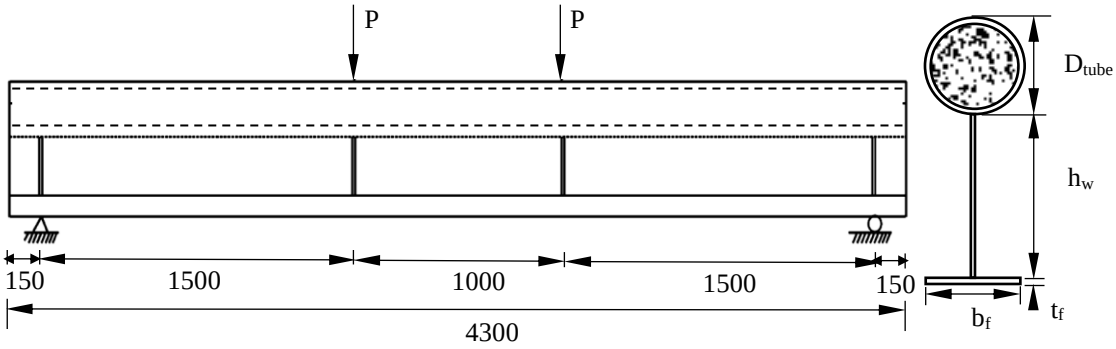

Fig. 4.7 Schematic of the simply supported beam (all units in mm)

4.5 Support and loading conditions

For the validation study, simply supported boundary conditions are considered as was the case in the experiments that are being used for validation (Wang et al., 2008). The geometry and loading conditions are symmetrical about the mid-span and therefore only half the girder length is explicitly modelled, and appropriate boundary conditions are applied at the plane of symmetry. Accordingly, simply supported boundary conditions are applied to the end of the girder whilst the other end has symmetrical boundary conditions, as shown in Fig. 4.8, in which u_x, u_y, u_z, φ_x, φ_y, and φ_z are the displacements and the rotations about the global x, y and z axes, respectively. The y-z plane is considered to be in-plane whilst the x-z and x-y planes are out-of-plane. At the end of the beam (i.e. at the support), the vertical (u_y) and lateral displacements (u_x) of all nodes along the y-axis (i.e., when x = 0), and the twist rotations about z and y-axes (φ_z and φ_y) are restrained against movement and therefore assigned values equal to zero. In addition, the end of the beam is modelled as a rigid body and the whole depth of the cross-section is subjected to identical tensile stresses. The tensile load is applied at a reference point which is selected in the current work to coincide with the centre of gravity of the steel section. At the mid-span of the girder, the longitudinal displacements (u_z) and rotations about the x- and y-axes (φ_x and φ_y) are also restrained against all movement. The vertical load is applied on the top of the member as an imposed displacement through two concentrated loads along the full length of the beam or one loading point when half the span is considered.

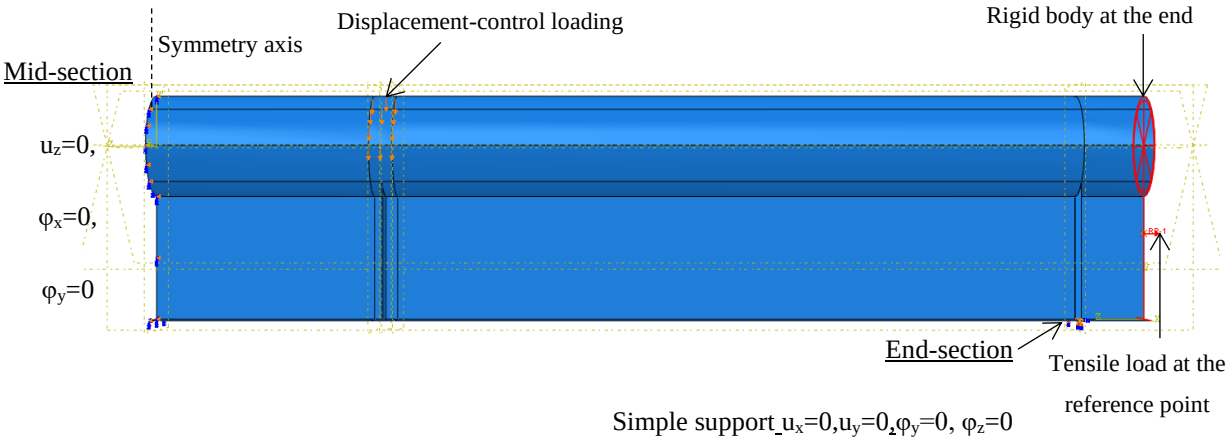

Fig. 4.8 Support and loading conditions of FE model for the circular CFTFG

4.6 Failure criteria

In order to determine when the circular CFTFG has failed, a number of failure criteria have been defined and these are closely monitored during simulation. The possible failure modes of a CCFTFG subjected to positive bending and axial tension are as follows:

- Local buckling: a tubular flange should not buckle locally before yielding in compression. Therefore, the local buckling requirement provided by the AASHTO design specifications (1998) for circular tube compression members has been checked for all specimens examined in this study, in accordance to:

$$\frac{D_{tube}}{t_t} \leq 2.8\sqrt{\frac{E_s}{f_y}} \tag{4.15}$$

  Eq. 4.15 was originally developed based on an unfilled tube although the AASHTO specification recommends using the expression for concrete-filled tubes also.

- Excessive yielding of the steel beam: the spread of yielding from the bottom surface of the girder, at the mid-span. A tensile yielding strain (ε_s) of 0.2 is employed in the current study as the limiting acceptable value. This failure mode is clearly dependent on the level of vertical and axial loading that is applied.
- Deflection limit: the maximum level of mid-span deflection that can be tolerated in the girder, depending on the application. Here, it is suggested that the maximum

acceptable limit of allowable deflection is L/120, where L is the member length, in accordance with AISC standard (2005).

4.7 Solution method

The implicit dynamic analysis method in ABAQUS with adaptive stabilisation is employed to simulate the nonlinear response of the CCFTFG. Finite element analysis with concrete elements in tension may result in convergence problems. In order to avoid these, the discontinuous analysis option is also employed in the general solution control options of the programme. The applied moment acting on the girder comprises two components, (1) the direct moment due to the applied vertical load, and (2) the second-order moment created by the eccentricity of the applied axial load relative to the plastic centroid of the section. Thus, the moment equilibrium equation is given as:

$$M = Pa + Ne \tag{4.16}$$

where P is the vertical force applied on the beam, a is the distance between the simple support and the vertical force, N is the horizontal axial force applied placed through a reference point in the steel web, and e is the eccentricity between the location of the axial load and the plastic neutral axis (PNA) of the circular CFTFG.

4.8 Validation of the FE model

There are no available test results for circular CFTFGs under combined loading conditions available in the literature. Therefore, the model is validated using the only available test results which focussed on the behaviour of CCFTFGs under pure bending conditions (Wang et al., 2008). The load-displacement response of the CFTFG from both the FE model and the experimental programme is presented in Fig. 3.7, see chapter 3 section 3.5. It is clear that the FE model is capable of providing a good representation of the general response and also offers an excellent prediction of the ultimate load of the circular CFTFG. The failure mode observed in both the FE model and the experiment, is a combination of steel yielding and torsional buckling. Overall, the simulated load-deformation curves reflect the experimental behaviour very well and it is concluded that the FE model is capable of predicting the behaviour and strength of that member well and is suitable for conducting further parametric studies on CCFTFGs under positive bending and axial tension.

4.9 Behaviour of CCFTFGs under combined loading

4.9.1 General

In this section, the FE model is used to study the interaction of bending moment and axial tension for circular CFTFGs with different properties. In order to specify a reliable moment-axial force (M–N) interaction diagram, a parametric study is conducted using a series of beams with different material and geometric design parameters. The beams studied are all 4300 mm in length (L) and are transversally stiffened with double-sided flat plate stiffeners which are 12 mm in thickness ($t_{stiffener}$) and located at the support and loading locations. A total of 44 different arrangements are considered in this study, as presented in Tables 4.3 and 4.4. For clarity, in the current section, the results are presented in two general categories: (i) members with different tube diameters (D_{tube}) (Table 4.3) and (ii) beams with various tube (t_t) and web thicknesses (t_w) (Table 4.4). All specimens contain concrete infill with a compressive strength of 38.6 MPa.

In the specimens listed in Table 4.3, models with five different tube diameters (D_{tube} = 180, 200, 210, 219 and 300 mm) are considered. For each model, two web heights (h_w = 267 and 500 mm) and two flange thicknesses (t_f = 14 and 28 mm) are investigated. The tube and web thicknesses are fixed at 8 mm and 6 mm, respectively. For the specimens listed in Table 4.4, models with three different tube thicknesses (t_t = 5, 8 and 10 mm) are considered and for each model, two different web heights (h_w = 267 and 500 mm), two different web thicknesses (t_w = 6 and 10 mm) and two flange thicknesses (t_f = 14 and 28 mm) are studied. The tube diameter is fixed at 219 mm for all of the cases in Table 4.4. All of the beams included in the parametric study are subjected to positive (sagging) bending through the application of vertical loads in combination with axial tension. The vertical loads (P) are kept constant whilst various levels of axial tension are applied, ranging from 10% to 80% of the ultimate axial strength (N_u) of the steel section. This is a similar approach to that taken by other researchers (e.g. Vasdravellis et al., 2012a, 2012b, 2015)).

For illustration, Fig. 4.9(a) shows the various responses for the beam GR1, as defined in Table 4.3, in terms of vertical load versus deflection for each of the applied axial load levels. Fig. 4.9(b) presents the Von Mises stress contour illustrating the progression of yielding in the steel beam in the elastic range. For this beam, yielding first occurs in the bottom flange when the applied axials loads and bending moments are 231 kN and 455.6 kNm, respectively, as shown in Fig. 4.9(b). The responses presented in Fig. 4.9(a) show

that at a particular load level, the beams with a greater degree of axial load applied demonstrate a relatively stiffer behaviour compared with beams with lower axial loads applied. The analysis continues until one of the failure criteria described in Section 4.6 is satisfied or the ultimate load level is reached. The data in this figure clearly demonstrates that increasing levels of axial load have the effect of reducing the capacity of the girder to carry vertical loads.

The axial capacities of the CCFTFGs examined herein are presented in Tables 4.3 and 4.4 and these values are defined with reasonable accuracy as the axial capacity of the steel section (N_u), which is the sum of the tensile strengths of the loaded steel areas:

$$N_u = A_S f_y \tag{4.17}$$

where A_s and f_y are the cross-sectional area and yield strength of the steel, respectively. Also included in the tables are the ultimate moment of the girders (M_u) which is defined later, as well as 40% of N_u (N_{40}) for each girder with the corresponding moment which acted on the member in that condition (M_{40}). This is to facilitate analysis of the results later in this chapter.

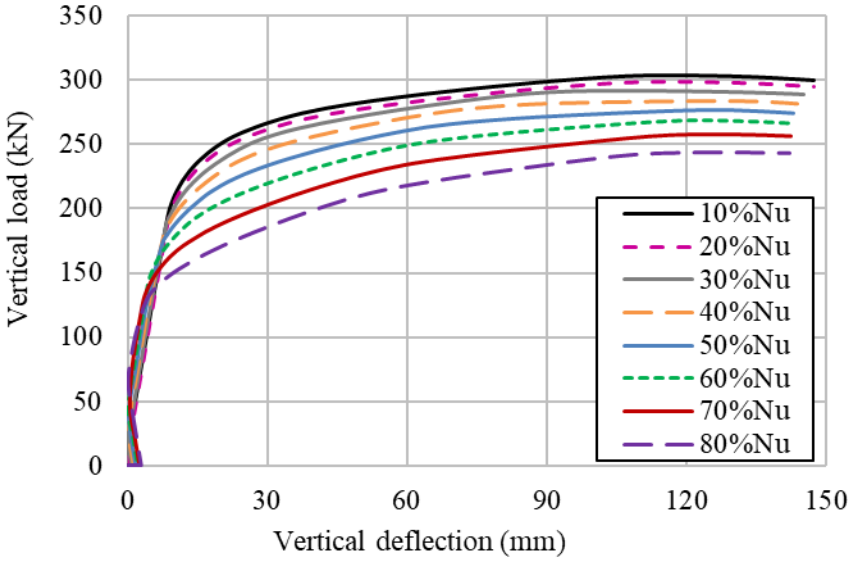

(a)

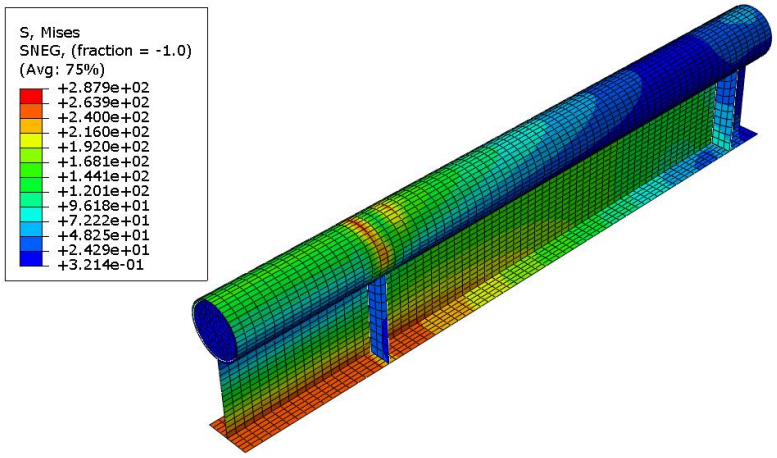

(b)

Fig. 4.9 (a) Load–deflection responses for CFTFG GR1 with various levels of axial tension and (b) the progression of yielding in the elastic range for the steel beam for beam GR1 at an axial load equal to 231 kN and a simultaneously applied bending moment of 455.6 kNm

Table 4.3 Details and FE ultimate of both axial load and bending moment of CCFTFGs

CCFTFG Group	Specimen	Geometric details				N_u (kN)	M_u (Al-dujele et al., 2018) (kNm)	N_{40} (kN)	$M_{40,FE}$ (kNm)	$(\frac{M_{40,FE}}{M_u})$ %	$M_{40,des}$ (kNm)
		L (mm)	D_{tube} (mm)	h_w (mm)	t_f (mm)						
G1	GR1	4300	180	267	14	-2310.5	454.3	-924.2	378.9	83.4	345.3
	GR2				28	-2915.3	667.2	-1166.1	587.7	88.0	507.1
	GR3			500	14	-2713.1	758.4	-1085.2	572.9	75.5	576.4
	GR4				28	-3317.9	1023.7	-1327.1	833.1	81.3	778.0
G2	GR5		200	267	14	-2455.2	494.6	-982.0	400.3	80.9	376.0
	GR6				28	-3060.0	717.2	-1224.0	620.9	86.6	545.1
	GR7			500	14	-2857.8	805.4	-1143.1	588.5	73.0	612.1
	GR8				28	-3462.6	1073.5	-1385.0	840.2	78.2	815.9
G3	GR9		210	267	14	-2527.6	513.6	-1011.0	408.4	79.5	390.4
	GR10				28	-3132.4	738.1	-1252.9	630.3	85.3	561.0
	GR11			500	14	-2930.2	824.5	-1172.0	593.4	71.9	626.6
	GR12				28	-3534.9	1094.9	-1413.9	851.8	77.7	832.2
G4	GR13		219	267	14	-2592.7	544.6	-1037.0	425.6	78.1	414.0
	GR14				28	-3197.5	760.3	-1278.9	640.8	84.2	577.8
	GR15			500	14	-2995.3	845.9	-1198.1	598.1	70.7	642.0
	GR16				28	-3600.1	1121.2	-1440.0	860.6	76.8	852.1
G5	GR17		300	267	14	-3178.7	735.8	-1271.4	505.3	68.6	559.2
	GR18				28	-3783.5	1008.7	-1513.3	714.4	70.8	766.6
	GR19			500	14	-3581.3	1082.4	-1432.5	720.5	66.5	822.0
	GR20				28	-4186.1	1363.7	-1674.4	925.2	67.8	1036.4

Table 4.4 Details and FE ultimate of both axial load and bending moment of CCFTFGs

CCFTFG Group	Specimen	Geometric details						N_u (kN)	M_u (Al-dujele et al., 2018) (kNm)	N_{40} (kN)	$M_{40,FE}$ (kNm)	$(\frac{M_{40,FE}}{M_u})$ %	$M_{40,des}$ (kNm)
		L (mm)	D_{tube} (mm)	h_w (mm)	t_w (mm)	t_t (mm)	t_f (mm)						
G6	GR21	4300	219	267	6	5	14	-2033.8	477.3	-813.5	413.4	86.6	362.8
	GR22						28	-2638.6	707.7	-1055.4	619.1	87.5	538.0
	GR23					8	14	-2592.7	544.6	-1037.1	425.6	78.1	414.0
	GR24						28	-3197.5	760.3	-1278.9	640.8	84.2	577.8
	GR25					10	14	-2956.2	560.7	-1182.5	390.1	69.5	426.2
	GR26						28	-3561.0	793.7	-1424.4	603.1	75.9	603.2
G7	GR27				10	5	14	-2341.4	552.7	-936.6	474.4	85.8	420.1
	GR28						28	-2946.2	769.3	-1178.5	666.9	86.6	584.7
	GR29					8	14	-2900.3	603.2	-1160.1	488.7	81.0	458.5
	GR30						28	-3505.1	828.9	-1402.0	766.9	92.5	630.0
	GR31					10	14	-3263.8	638.3	-1305.5	479.7	75.1	485.1
	GR32						28	-3868.6	863.4	-1547.4	800.1	92.6	656.2
G8	GR33			500	6	5	14	-2436.4	800.8	-974.6	591.7	73.8	608.6
	GR34						28	-3041.2	1069.3	-1216.5	840.2	78.5	812.7
	GR35					8	14	-2995.3	845.9	-1198.1	598.1	70.7	642.9
	GR36						28	-3600.1	1121.2	-1440.0	867.6	77.3	852.1
	GR37					10	14	-3358.8	878.7	-1343.5	608.0	69.2	667.8
	GR38						28	-3963.6	1157.3	-1585.5	874.4	75.6	879.6
G9	GR39				10	5	14	-3012.4	985.2	-1205.0	819.3	83.2	748.7
	GR40						28	-3617.2	1312.6	-1446.9	1191.6	90.7	997.6
	GR41					8	14	-3571.3	1039.0	-1428.5	881.2	84.8	789.6
	GR42						28	-4176.1	1381.1	-1670.4	1207.0	87.3	1049.6
	GR43					10	14	-3934.8	1074.5	-1573.9	888.9	82.7	816.6
	GR44						28	-4539.6	1417.7	-1815.9	1222.5	86.2	1077.5

4.9.2 Interaction curves

The moment-axial load interaction curves generated from the parametric study are presented in Figs. 4.10-4.14. In general, all of the CCFTFGs behaved well and there was no sudden collapse of any structural component during the simulations. A general conclusion is that the interaction diagram for all beams follows a similar pattern and the moment capacity of each is reduced with an increase in axial tensile force acting in the steel beam section. Fig. 4.10(a)-(d) presents the moment versus axial load interaction diagrams obtained from the ABAQUS model for girders with different tube diameters (D_{tube}) (as given in Table 4.3). For ease of visualisation and analysis, the results are grouped into four different images. Girders with a web height (h_w) of 267 mm and different tube sizes (D_{tube}) are plotted in Figs. 4.10(a) and (b) for flange thicknesses of 14 and 28 mm, respectively, whilst the equivalent images for members with a web height of 500 mm are presented in Figs. 4.10(c) and (d). With reference to these figures, the following observations are made:

- Firstly, Fig. 4.10(a) shows that for a given level of applied axial load (40% of the ultimate axial strength, for example, as presented in Table 4.3 and 4.4, N_{40}), the reduction in bending moment carried by each girder is 83.4%, 80.9%, 79.5%, 78.1% and 68.6% for GR1, GR5, GR9, GR13 and GR17, respectively, compared with their ultimate moment capacity, M_u (i.e. the moment that can be achieved when no axial load is applied). Similarly, these values from Fig. 4.10(b) are 88.0%, 86.6%, 85.3%, 84.2% and 70.8% for GR2, GR6, GR10, GR14 and GR18, respectively; from Fig. 4.10(c) are 75.5, 73.0, 71.9, 70.7 and 66.5 for GR3, GR7, GR11, GR15 and GR19, respectively, and; (iii) from Fig. 4.10(d) are 81.3, 78.2, 77.7, 76.8 and 67.8 for GR4, GR8, GR12, GR16 and GR20, respectively. This can be seen by referring to the $M_{40,FE}/M_u$ ratios presented in Table 4.3.
- It is clear that the circular concrete filled tubular flange girders (CCFTFGs) with a relatively small tubular flange (D_{tube}) experience a greater reduction in their moment-carrying capability as a result of increasing the applied axial compared with member with a larger diameter top tube (in Fig. 4.10(a), for example, GR1 has the smallest tubular flange, followed by GR5, GR9, GR13 and GR17, respectively). This is attributed to the concrete contribution being less significant for the sections with a relatively small diameter tubular flange.
- CCFTFGs with relatively thin bottom flanges (t_f) experience a more significant reduction in moment-carrying capability, relative to their ultimate moment

capacity, when axial tension is also applied to the section (e.g. GR1 compared with GR2 or GR5 compared with GR6, etc.). The reduction in bending moment carried by each girder is 83.4% and 88.0% for GR1 and GR2, respectively, compared with their ultimate moment capacity, M_u (i.e. the value that can be achieved when no axial load is applied). As the amount of axial load introduced in the steel beam increases, the moment resistance decreases considerably, as shown in the percentage ratio values presented in Table 4.3.

- The influence of web height is examined by comparing GR1 in Fig. 4.10(a) and GR3 in Fig. 4.10(c) which have identical properties apart from h_w which is 267 and 500 mm, respectively. The reduction in moment for GR1, relative to its moment capacity without any axial load, is just 83.4% whereas the equivalent value for GR3 is about 75.5%. The same observation can be made by comparing the other interaction curves in Fig. 4.10(a) and (c), and indeed Fig. 4.10(b) and (d) when h_w=267 mm and t_f=28 mm.
- The effect of thickness of the tube (t_t) and web (t_w) on the response is observed by comparing the data in Table 4.4. A relative increase in tube thickness leads to a reduction of the of the moment carrying capacity. For instance, as can be seen in the $M_{40,FE}/M_u$ ratios given in Table 4.4, the moment capacity is reduced by 86.0%, 84.2% and 75.9% for GR22, GR24 and GR26, respectively at 40% of ultimate axial load. On the other hand, the $M_{40,FE}/M_u$ ratios increase when the web thickness increases. As can be seen in the Table 4.4, the moment is reduced by 73.8% and 83.2% for GR33 and GR39, respectively.

From the interaction diagrams and the data presented in Tables 4.3 and 4.4 it can be concluded that the flexural capacity of circular CFTFGs under combined tension and bending moments is not affected when the level of the axial force is relatively low (i.e. around 20% of N_u). Nevertheless, a general conclusion is that the moment capacity is reduced with the presence of applied axial tensile force acting on the steel section.

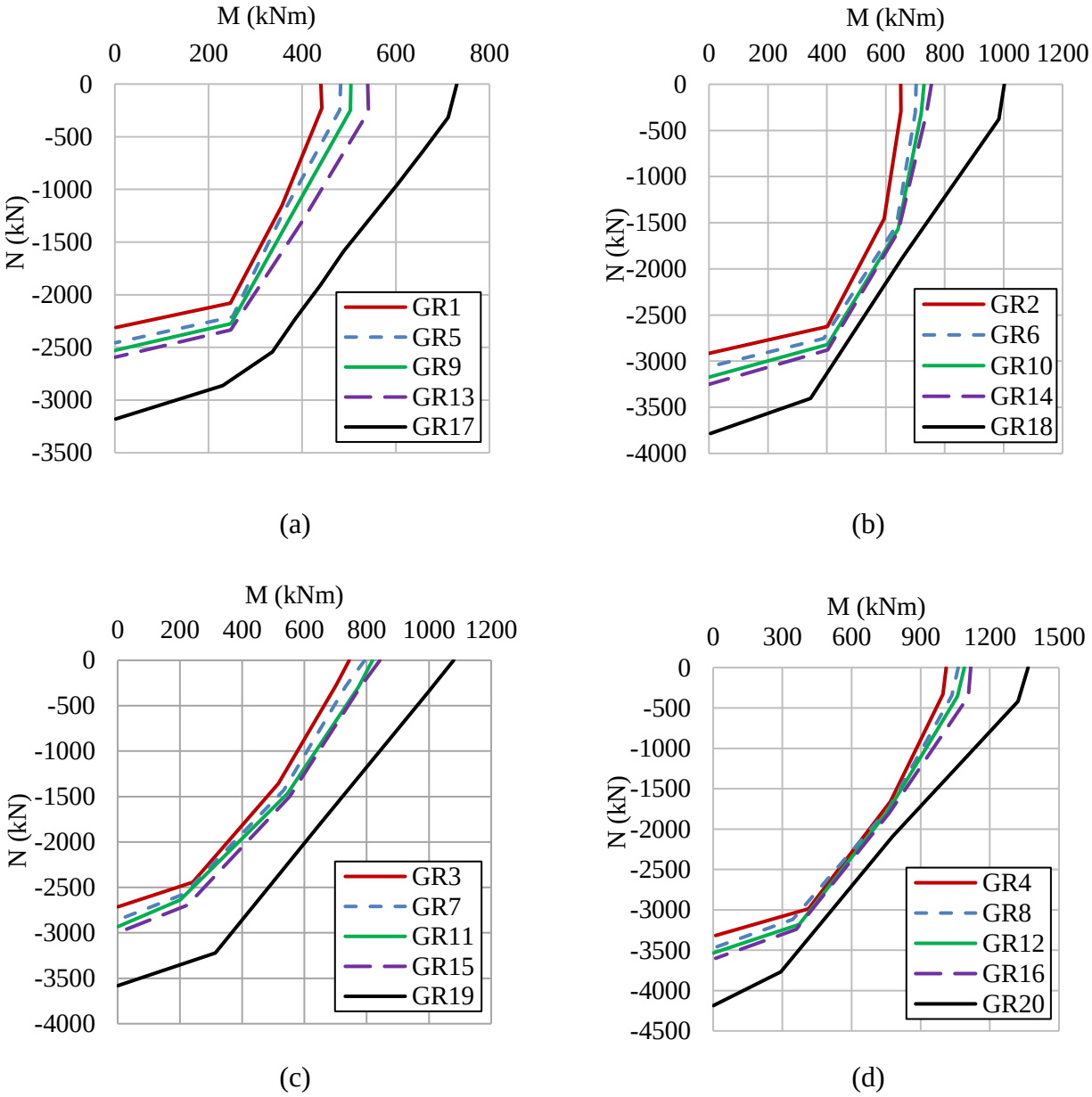

Fig. 4.10 Moment–axial force interaction diagram for CCFTFGs

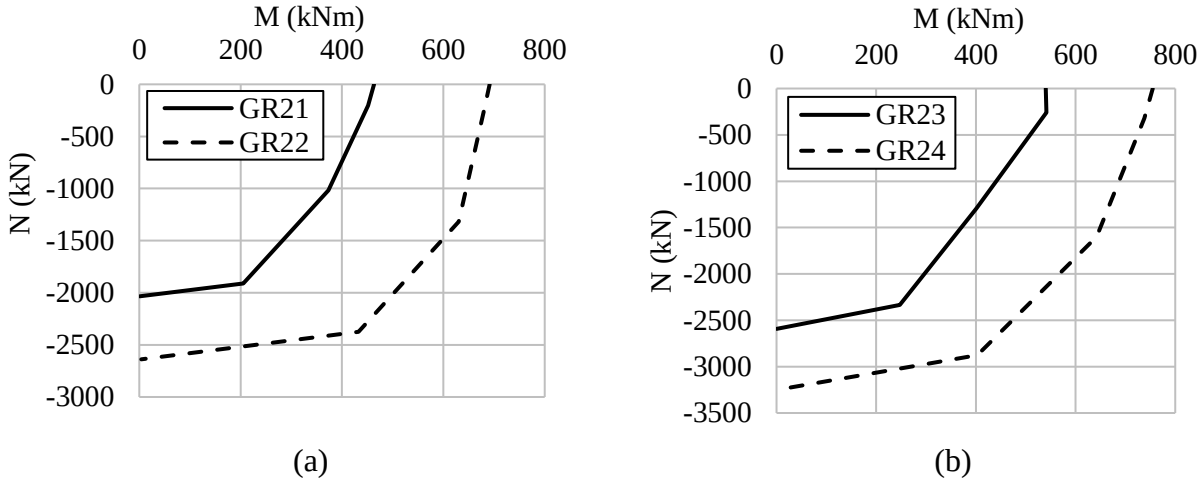

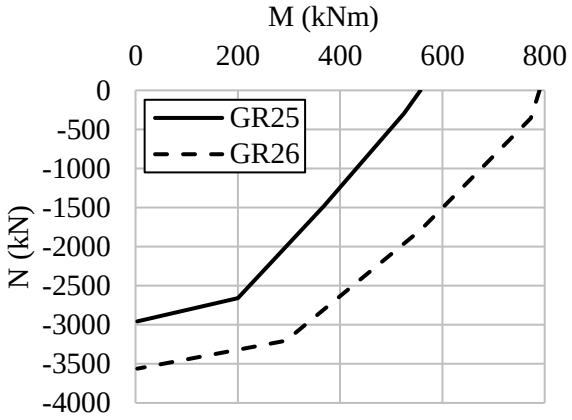

(c)

Fig. 4.11 Moment–axial force interaction diagram for the group G6

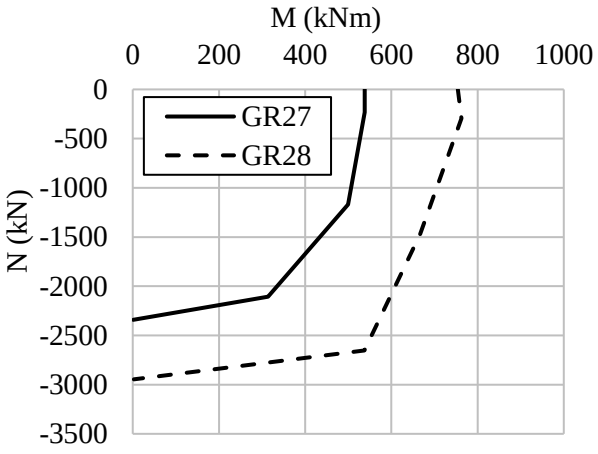

(a)

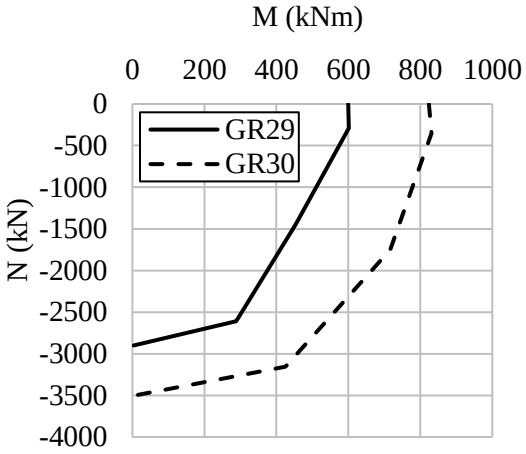

(b)

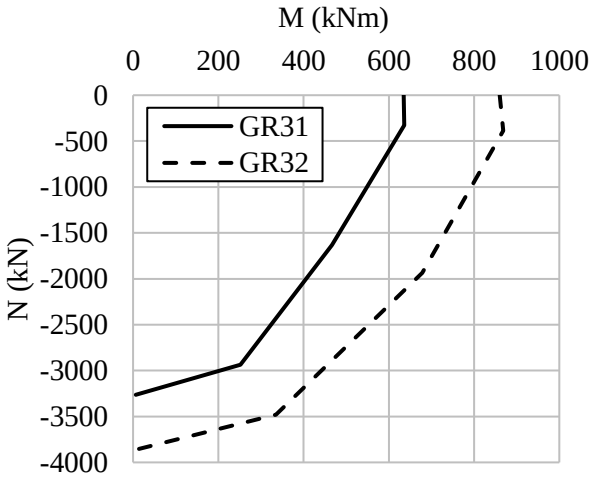

(c)

Fig. 4.12 Moment–axial force interaction diagram for the group G7

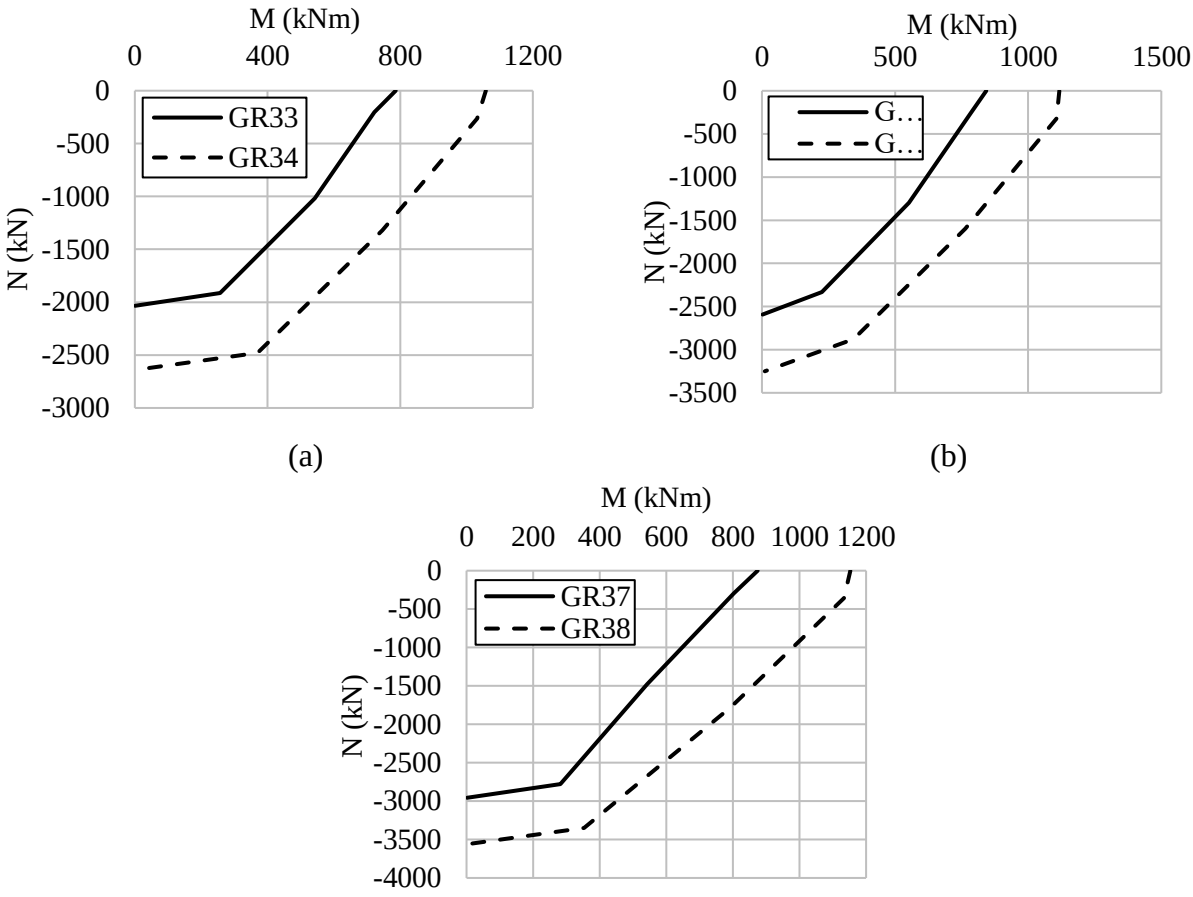

Fig. 4.13 Moment–axial force interaction diagram for the group G8

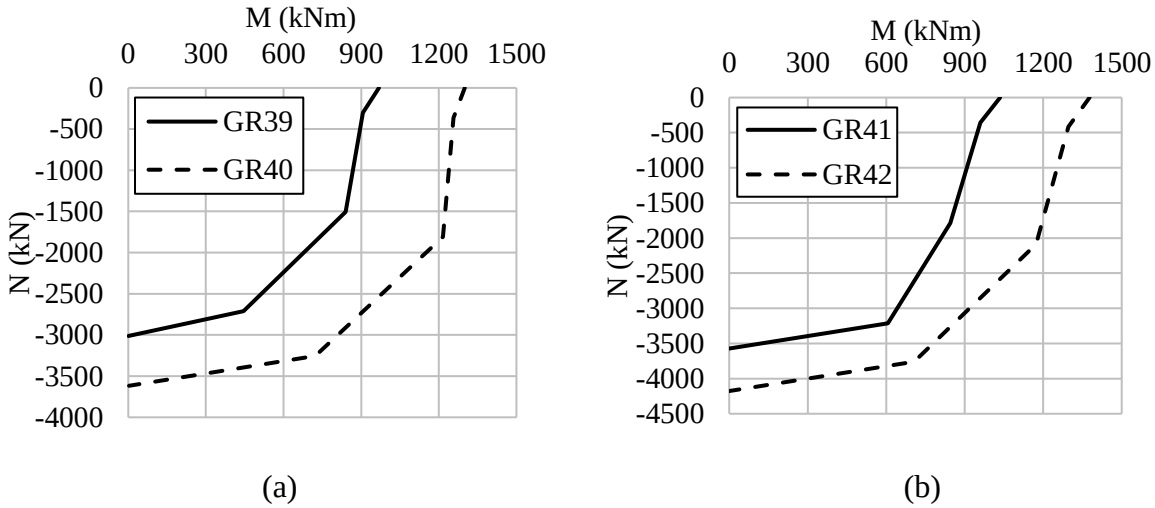

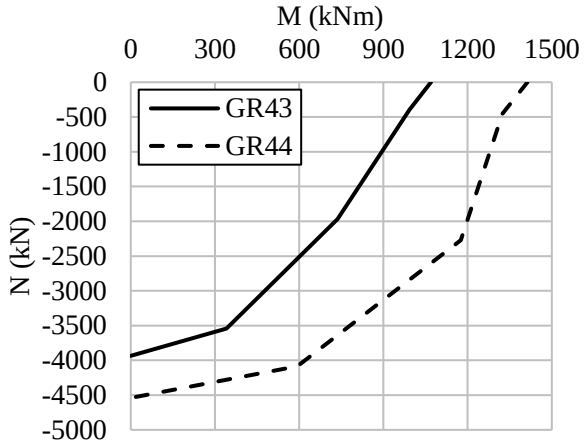

(c)

Fig. 4.14 Moment–axial force interaction diagram for the group G9

4.10 Design of CCFTFGs under combined loading

In this section, a simplified analytical approach for assessing the capacity of circular concrete filled tubular flange girders (CCFTFGs) under combined loading is presented, based on the observations from the FE simulations as well as a fundamental review of the behaviour. Firstly, it is necessary to assess the cross-sectional behaviour for a section under pure bending, before extending the study to allow for axial load also.

4.10.1 Moment capacity of a CCFTFG (M_u)

The ultimate bending capacity (M_u) of a CCFTFG in pure flexure can be derived based on the equilibrium of internal forces in the cross-section. Previously, a series of analytical expressions for predicting the location of the PNA (y_1 from the top of the girder) and M_u was presented by Al-Dujele et al. (2018). A briefly description of the ultimate bending capacity of a CCFTFGs in pure flexure can be fond in chapter 3 section 3.6.

4.10.2 CCFTFGs under combined loading

Based on the FE results and the parametric study, a simple design model for circular CFTFGs under combined sagging moments and axial tension is proposed in this section. For this purpose, the interaction data points presented before are given in non-dimensional form in Fig. 4.15 for each of the CCFTFGs included in the parametric study. In these figures, the axial force and bending moment acting on the beams simultaneously are normalised by the axial capacity (N_u) and moment capacity (M_u), respectively. Using

the data from the parametric study, it is proposed that for the design of CCFTFGs subjected to combined axial load and bending moment, the following interaction expression should be satisfied:

$$N = N_u \quad \text{for} \quad M \leq 0.4M_u$$

$$\frac{M}{M_u} + 0.6\frac{N}{N_u} \leq 1.0 \quad \text{for} \quad M > 0.4M_u \tag{4.18}$$

This proposed design expression is the same for all beams included in the current study and is presented in Fig. 4.15, denoted as 'Design'. According to Eq. 4.18, the moment capacity of a CCFTFG reduces linearly from 100% of the ultimate value when there is no axial load present to around 40% of M_u when the axial load applied equals N_u. It is noteworthy however, that in practice it is very rare for a beam to be subjected to tensile axial forces greater than the 30 to 40% of its axial capacity (Vasdravellis et al., 2012a; Kirkland, 2014). Nevertheless, this study has considered the full range of axial force possibilities in order to complete the interaction diagram and gain a complete understanding of the behaviour of CCFTFGs under combined loading.

Tables 4.3 and 4.4 present a comparison between the bending strength predicted by the FEM ($M_{40,FEM}$) and the design moment capacity ($M_{40,des}$) calculated by Eq. 4.18 for a selection of girders, as well as the associated error. A positive value for the error indicates an unconservative prediction. The results are not presented for all girders in the study for brevity but similar analaysis has been completed for all of the CCFTFGs presented in Tables 4.3 and 4.4. Based on the images presented in Fig. 4.15 and the data in Tables 4.3 and 4.4, it is clear that the proposed equation provides a conservative estimation of the interaction behaviour of the majority of CCFTFGs. The error is small when the level of axial load is relatively low (i.e. up to and including 60% of the axial capacity, which is the most realistic scenario for CCFTFGs under combined loading) and becomes slightly greater as the axial load increases to 80% of N_u.

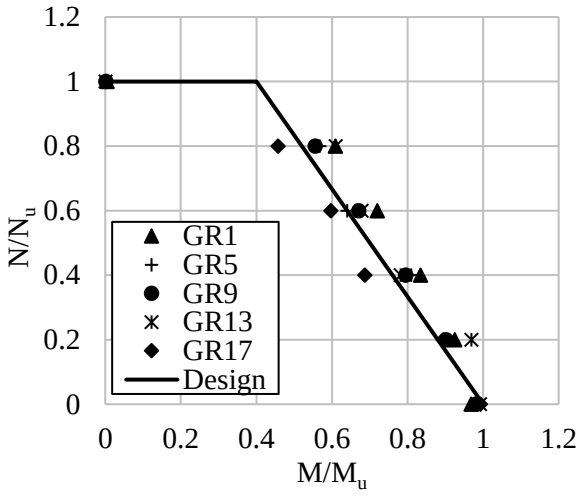
1.2
1
0.8
0.6
0.4
0.2
0
N/Nu
0 0.2 0.4 0.6 0.8 1 1.2
M/Mu
GR1
GR5
GR9
GR13
GR17
Design

(a)

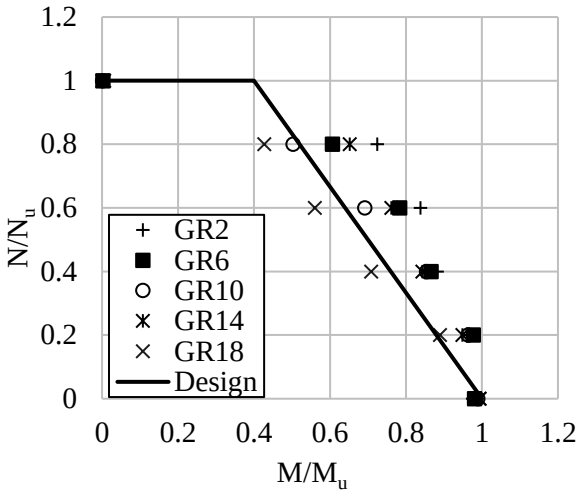
1.2
1
0.8
0.6
0.4
0.2
0
N/Nu
0 0.2 0.4 0.6 0.8 1 1.2
M/Mu
GR2
GR6
GR10
GR14
GR18
Design

(b)

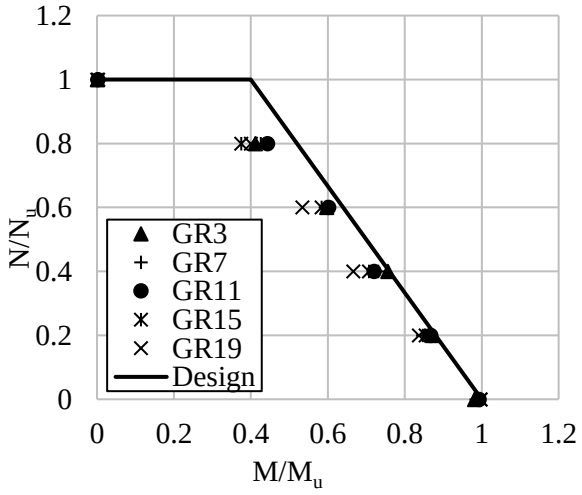
1.2
1
0.8
0.6
0.4
0.2
0
N/Nu
0 0.2 0.4 0.6 0.8 1 1.2
M/Mu
GR3
GR7
GR11
GR15
GR19
Design

(c)

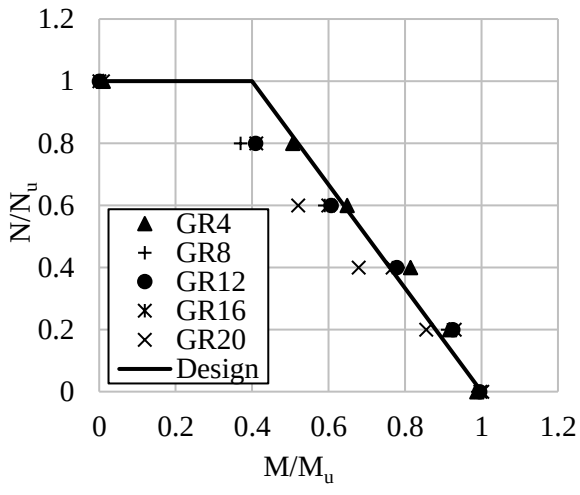
1.2
1
0.8
0.6
0.4
0.2
0
N/Nu
0 0.2 0.4 0.6 0.8 1 1.2
M/Mu
GR4
GR8
GR12
GR16
GR20
Design

(d)

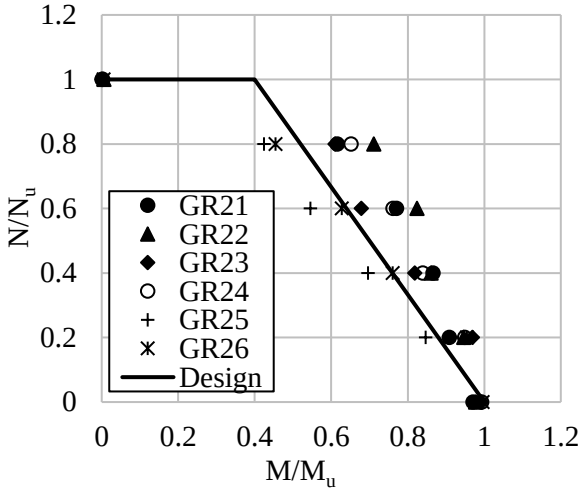
1.2
1
0.8
0.6
0.4
0.2
0
N/Nu
0 0.2 0.4 0.6 0.8 1 1.2
M/Mu
GR21
GR22
GR23
GR24
GR25
GR26
Design

(e)

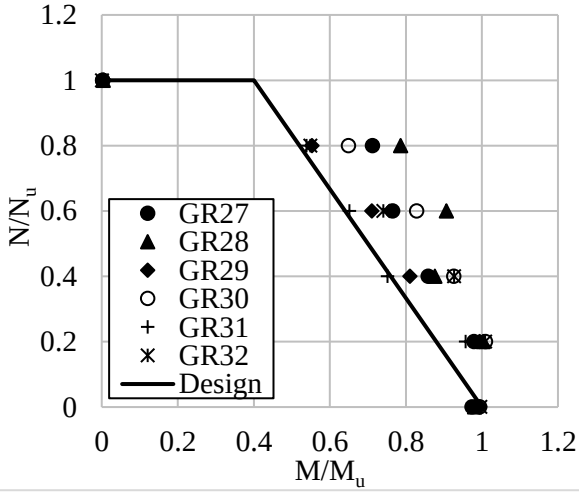
1.2
1
0.8
0.6
0.4
0.2
0
N/Nu
0 0.2 0.4 0.6 0.8 1 1.2
M/Mu
GR27
GR28
GR29
GR30
GR31
GR32
Design

(f)

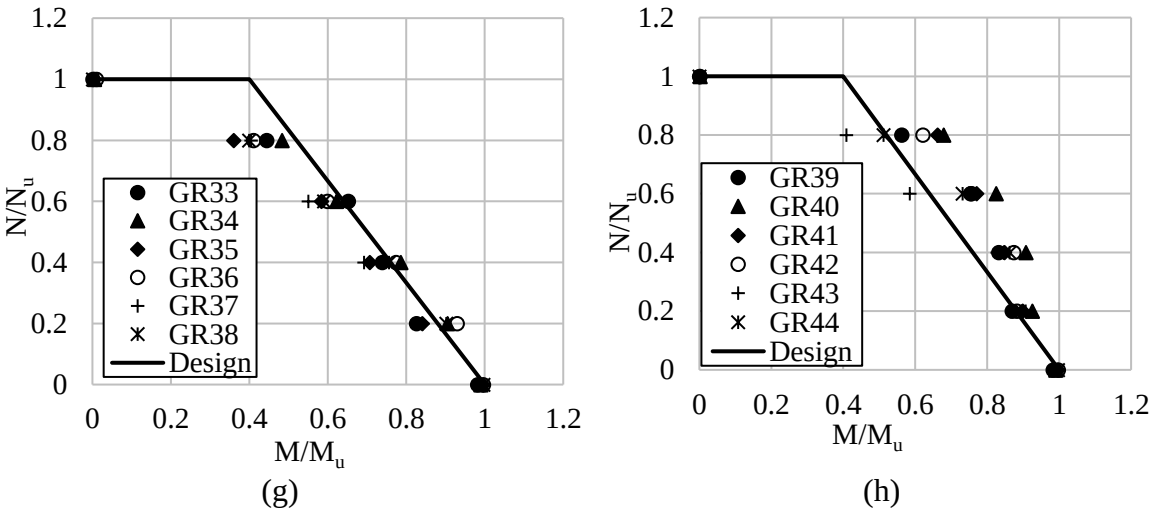

Fig. 4.15 Results from the parametric study and proposed design equation

4.11 The influence of yielding strength of steel

In this section, the CCFTFG GR13 (as described in Table 4.3) is modelled using different grades of structural steel, ranging from S235 to S690, to assess the influence of this parameter on the behaviour. The details and results from this parametric study are presented in Table 4.5. Fig. 4.16 presents (a) the moment–axial force interaction diagrams for these beams and (b) the proposed design equation for these CCFTFGs under combined bending moment and axial tension. In Fig. 4.16(a), it is notable that all the predicted responses are of a similar shape. When the applied axial load is 40% of the ultimate axial capacity, an increase in the yield strength of the steel section leads to a reduction in the combined moment compared with ultimate moment. For example, when the steel section is made from S235 steel, $M_{40,FE}$=290.51 kNm while M_u=442.7 kNm, giving a ratio of $M_{40,FE}$ to M_u of 65.6%. On the other hand, if the same CFTFG is made using S355 steel, these values change to $M_{40,FE}$=462.50 kNm and M_u=637.9 kNm, with the corresponding ratio being 72.5%. So, the moment which can be carried by the section when the applied axial load is 40% of N_u increases when a higher grade of steel is used. In addition as can see by the $M_{40,FE}/M_u$ ratio in Table 4.5, the reduction ratio of moment relative to M_u increase with increase the steel yielding 65.62%, 72.50%, 77.62% and 80.39% for S235, S355, S460 and S690, respectively. As expected, the axial load and bending moment capacity increases in accordance with the yield strength.

Table 4.5 Details and FE strengths of GR13 used to investigate the effect of f_y

Beam	f_y (N/mm^2)	N_u (kN)	M_u (Al-dujele et al., 2018) (kNm)	N_{40} (kN)	$M_{40,FE}$ (kNm)	$(\frac{M_{40,FE}}{M_u})\%$	$M_{40,des}$ (kNm)
GR13	235	-2115.6	442.7	-846.2	290.5	65.6	336.5
	355	-3195.8	637.9	-1278.3	462.5	72.5	484.9
	460	-4141.1	803.0	-1656.4	623.3	77.6	610.4
	690	-6211.6	1162.4	-2484.6	934.4	80.4	883.4

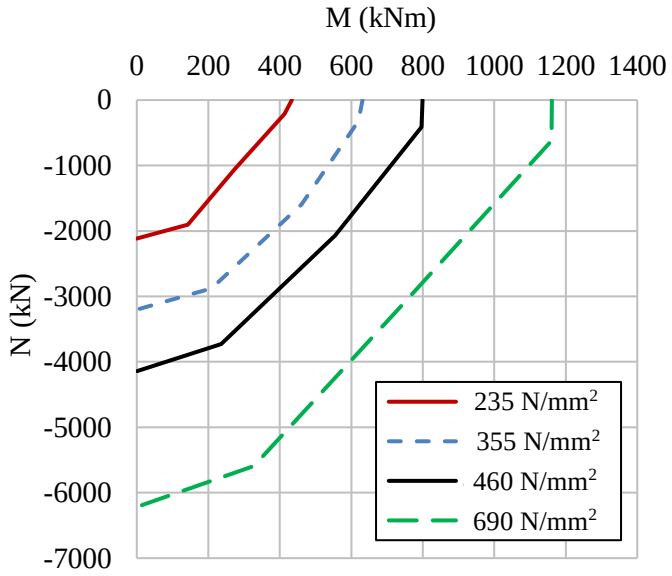

(a)

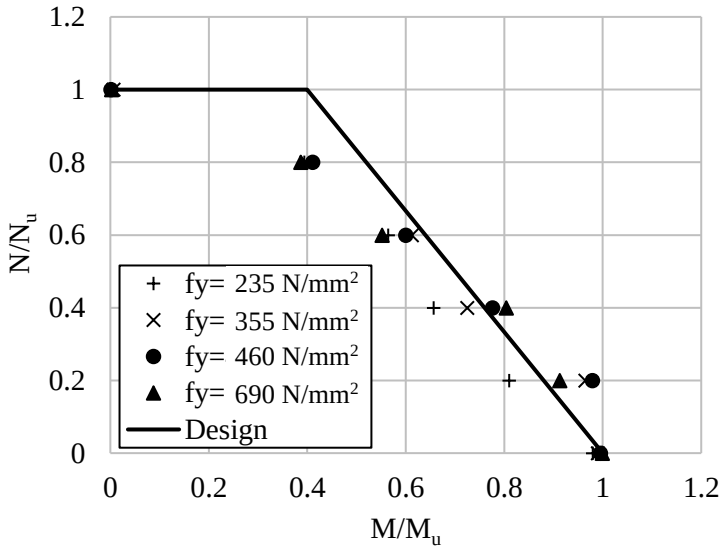

(b)

Fig. 4.16 Model GR13 (a) Moment–axial force interaction diagram with different yielding strength of steel (b) Proposed design equation for CCFTFGs under combined action with different yielding strength of steel

4.12 Concluding remarks

The main conclusion is that the moment capacity of a CCFTFG is reduced under the presence of an axial tensile force acting in the steel beam section but this is not a major issue within the realistic range of applied axial loads (up to 50% of N_u). In addition, the analysis demonstrates that the axial tensile force that the CCFTFG section can sustain is limited and the design axial tensile resistance should be taken equal to the plastic axial capacity of the steel beam alone. Based on the numerical results presented herein the following conclusions are drawn:

- Extremely large deflections and vertical loads are achieved when axial tension is introduced due to the ductile nature and large tensile strength of the steel beam.
- The bending moment capacity of a CCFTFG deteriorates under the simultaneous action of a relatively high axial tensile force with bending moments. However, the reduction is less or even negligible under a low to moderate axial force in most practical cases.
- The numerical simulations demonstrated that it is important to account for the axial force in the design of CFTFGs which are subjected to combined loading.
- An increase in tube thickness or bottom flange thickness leads to an increase in the reduction ratio of applied moment relative to M_u.
- The finite element analysis has confirmed the interaction curve shape for beams for a broad range of steel sections with varying geometric and material properties.

Chapter 5 : A study into the flexural behaviour of rectangular concrete filled tubular flange girders (RCFTFGs)

5.1 Introduction

The current chapter builds on the research in the previous chapters and studies the response of rectangular concrete filled tubular flange girders (RCFTFGs) and steel rectangular flange girders (SRFGs). As in earlier work, a finite element model is developed using the ABAQUS software to facilitate the study. The most influential parameters are examined, and design expressions are proposed, based on the outcomes of the study. This chapter proceeds with a detailed description of the FE model.

5.2 Finite element (FE) model

A finite element (FE) model has been developed using the ABAQUS software (Simulia, 2011) to simulate the behaviour of RCFTFG's in bending, and includes the material and geometric nonlinearities present in the response. The model has been developed and validated based on the experiments conducted by Muteb and Ali (2016). This programme included four simply supported specimens, two of which had concrete in the tubular flange (RCFTFG1 and RCFTFG2) and two which were left hollow (SRFG1 and SRFG2). The key dimensions of the test specimens are presented in Table 5.1 and also in shown in Fig. 5.1, including B_{Tf}, D_f, t_t, h_w, t_w, B_{Bf}, t_f, and $t_{stiffener}$ which represent the width, depth and thickness of the tube, the web depth and thickness, and the width and thickness of the bottom flange, respectively. Two different tubular flange depths were examined (40 mm and 20 mm) whilst all specimens had the same flange width (80 mm), cross-sectional height (0.17 m) and overall length (2.02 m). The beams were subjected to two concentrated loads in the vertical direction and the distance between the loading points was 0.64 m. There were six stiffeners along the length of the beam and each was 2.85 mm in thickness. These were located at the supports and loading points to prevent local instability of the web at these locations. Simply supported boundary conditions are simulated in the FE model by restraining suitable displacement and rotational degrees of freedom at the beam ends, replicating the experimental arrangement. Furthermore, bearing plates with dimensions 90×80×10 mm are included under each point load to prevent any local buckling in the steel section. The material properties incorporated in the model are presented in Table 5.2 including the yield strength (f_y), ultimate strength (f_u), Young's modulus (E_s) and Poisson's ratio of the steel as well as the compressive strength (f_c) and Poisson's ratio of the concrete (Muteb and Ali, 2016).

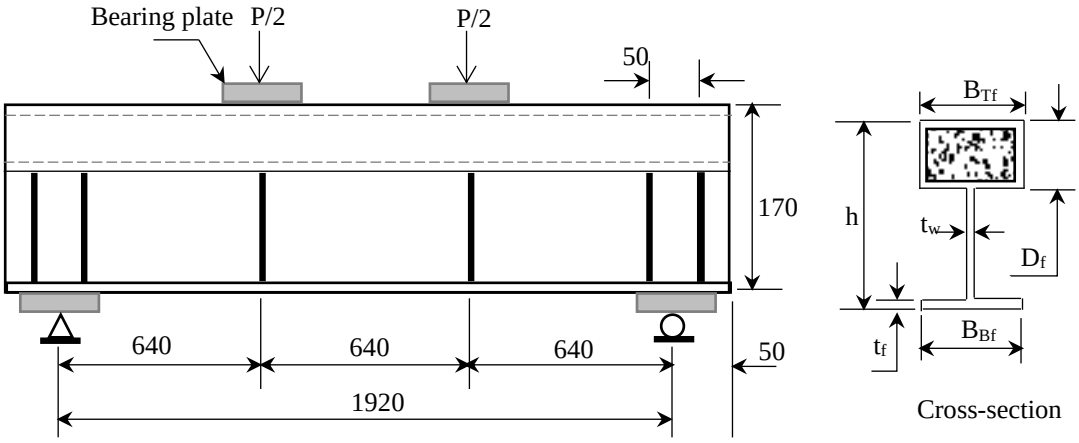

Fig. 5.1 Schematic of the concrete filled rectangular flange girder and cross-section (all units in mm)

Table 5.1 Dimensions of the RCFTFG cross-section

Specimen	B_{Tf} (mm)	D_f (mm)	t_t (mm)	h_w (mm)	t_w (mm)	B_{Bf} (mm)	t_f (mm)	$t_{stiffener}$ (mm)	$P_{u,Exp}$ (kN)	$P_{u,FE}$ (kN)	$P_{u,FE}/P_{u,Exp}$
RCFTFG1	80	20	2.85	147.15	2.85	80	2.85	2.85	73.5	74.2	1.010
RCFTFG2	80	40	2.85	127.15	2.85	80	2.85	2.85	71.0	71.4	1.006
SRFG1	80	20	2.85	147.15	2.85	80	2.85	2.85	61.1	61.4	1.005
SRFG2	80	40	2.85	127.15	2.85	80	2.85	2.85	58.0	59.7	1.029

Table 5.2 Details of the material properties (Muteb and Ali, 2016)

Steel				Concrete	
f_y (N/mm^2)	f_u (N/mm^2)	E_s (N/mm^2)	Poisson's ratio	f_c (MPa)	Poisson's ratio
236.8	377.2	200000	0.3	42.5	0.2

5.3 Material modelling

5.3.1 Steel

The stress-strain response of the structural steel is modelled as a bilinear, elastic-linear strain hardening relationship (Muteb and Ali, 2016), as shown in Fig. 5.2, where f_y and ε_{st} are the yield stress and strain at the onset of strain hardening, and f_u and ε_u are the ultimate tensile stress and strain at ultimate tensile stress, respectively. As given in Table 5.2, Young's modulus (E_s) and Poisson's ratio are 200×10^3 N/mm^2 and 0.3, respectively, whilst the yield and ultimate strength values for the flanges, web and stiffeners are 236.8 N/mm^2 and 377.2 N/mm^2, respectively. The strain at the onset of strain hardening

(ε_{st}) and the strain at the ultimate tensile stress (ε_u) are taken as 0.025 and 0.2, respectively (Ban and Bradford, 2013). The engineering stress–strain (σ_{eng}-ε_{eng}) curve is converted to true stress–strain (σ_{true}-ε_{true}) curve for the ABAQUS model using Eqs (5.1) and (5.2):

$$\varepsilon_{true} = \ln(1 + \varepsilon_{eng}) \tag{5.1}$$

$$\sigma_{true} = \sigma_{eng}(1 + \varepsilon_{eng}) \tag{5.2}$$

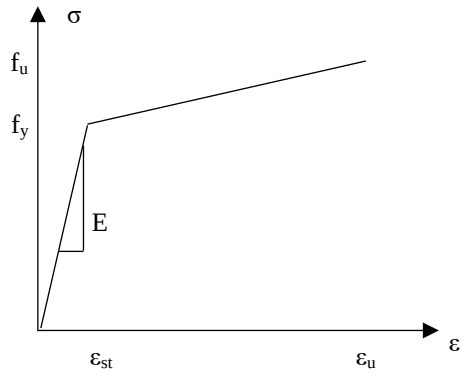

Fig. 5.2 Bilinear stress–strain curve adopted for steel elements

The steel section is represented using four-noded, three-dimensional shell elements with reduced integration (called S4R in the ABAQUS library (Simulia, 2011)), as presented in Fig. 5.3. Simpsons rule with seven integration points is used through the element thickness to determine the response through the section. The S4R element has six active degrees of freedom per node, including three displacements and three rotations. A tie contact is defined between the surface of the steel section and the edges of the stiffeners. Following a mesh sensitivity study, it was determined that an element size of 10×10 mm provides the best combination of accuracy and computational efficiency and therefore is applied to all elements in the model.

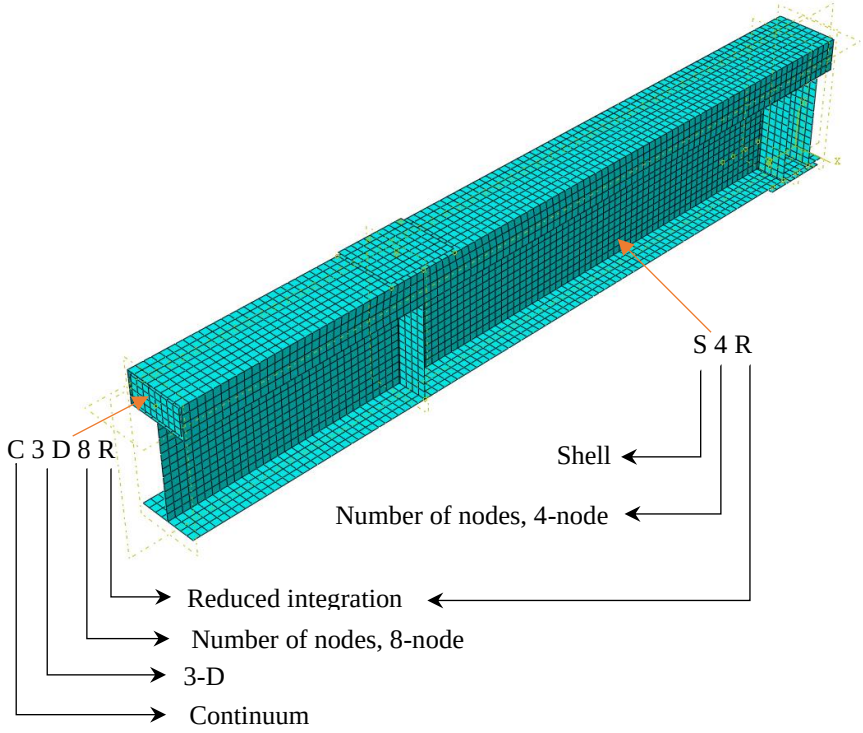

Fig. 5.3 Finite element mesh for a typical RCFTFG

5.3.2 Concrete

The concrete in the tubular flange acts mainly in compression although may be subjected to some degree of transverse loading also, as will be discussed later. Hence, the material relationship for confined concrete in rectangular CFST columns (Liang, 2009), as shown in Fig. 5.4, is used. The stress-strain response can be divided into ascending (O-A), constant (A-B), linearly descending (B-C) and constant (C-D) sections. The compressive stress for the ascending part O-A is calculated based on the equations given by Mander et al. (1988):

$$\sigma_c = \frac{f_{cc}\,\lambda\,(\varepsilon_c/\varepsilon_{cc})}{\lambda - 1 + (\varepsilon_c/\varepsilon_{cc})^{\lambda}} \tag{5.3}$$

$$\lambda = \frac{E_c}{E_c - (f_{cc}/\varepsilon_{cc})} \tag{5.4}$$

$$\varepsilon_{cc} = \varepsilon_c\left[1 + 5\left(\frac{f_{cc}}{f_c} - 1\right)\right] \tag{5.5}$$

where σ_c is the compressive stress, f_{cc} is the effective compressive strength of confined concrete, ε_c is the compressive concrete strain, ε_{cc} is the strain at f_{cc} and E_c is the Young's

modulus of concrete which is given by the empirical formulation provided in Eurocode 2 (EN 1992-1-1, 2004) and given in Eq. (5.6):

$$E_c = 22 \times (f_c/10)^{0.3} \tag{5.6}$$

In this expression, f_c is the unconfined cylinder compressive strength of the concrete and ε_c is the corresponding strain which is determined in accordance with Eurocode 2 Part 1-1 (EN 1992-1-1, 2004), as:

$$\varepsilon_c = 0.7(f_c)^{0.31} \leq 2.8 \tag{5.7}$$

When the concrete filled steel tube is exposed to axial compression, a gap occurs between the steel tube and the concrete core in the elastic range because the Poisson's ratio for concrete is less than that of steel. Beyond the elastic range, the inner concrete dilates (strains transversely) at a higher or faster rate than the steel tube, and contact develops again between the steel tube and the concrete. As the axial compressive stress increases further, continued dilation of the concrete core is restricted by the steel tube, generating a variable confining pressure in the concrete in the transverse direction. This confining pressure effectively increases the compressive strength of the concrete core. In a RCFTFG, the concrete is confined by the rectangular steel tube section, which results in increased ductility and strength of the concrete core, compared to unconfined concrete.

In the current study, the effective compressive strength of confined concrete (f_{cc}) is influenced mainly by the tube size, the quality of concrete and the loading rates. Hence, the value of f_{cc} is taken as $\gamma_c \times f_c$, where γ_c is the strength reduction factor proposed by Liang (2009) and expressed as:

$$\gamma_c = 1.85 D_c^{-0.135} \quad (0.85 \leq \gamma_c \leq 1.0) \tag{5.8}$$

where D_c is taken as the larger of $B_{Tf} - 2t_t$ and $D_f - 2t_t$ for a rectangular cross-section.

The other regions of the stress–strain curve (i.e. A-B, B-C and C-D in Fig. 5.4) for confined concrete are defined by the following equations given by Liang (2009):

$$\sigma_c = \begin{cases} f_{cc} & \text{for} \quad \varepsilon_{cc} < \varepsilon_c \leq 0.005 \\ \beta_c f_{cc} + 100(0.015 - \varepsilon_c)(f_{cc} - \beta_c f_{cc}) & \text{for } 0.005 < \varepsilon_c \leq 0.015 \\ \beta_c f_{cc} & \text{for } \varepsilon_c > 0.015 \end{cases} \tag{5.9}$$

In these expressions, β_c is a constant which accounts for the confinement effect on the concrete ductility and depends on the width-to-thickness ratio (B_s/t_t) of the concrete filled

rectangular flange. B_s is taken as the larger of B_{Tf} and D_f for the rectangular flange cross-section. Based on the experimental results presented by Tomii and Sakino (1979), βc is proposed by Liang (2009) to be taken as:

$$\beta_c = \begin{cases} 1.0 & \text{for } B_s/t_t \le 24 \\ 1.5 - (1/48)(B_s/t_t) & \text{for } 24 < B_s/t_t \le 48 \\ 0.5 & \text{for } B_s/t_t > 48 \end{cases} \quad (5.10)$$

The softening behaviour of concrete in the post-yield stage is determined by the β_c parameter and the concrete strain (ε_{cu}). The values of β_c determined using Eq. (5.10) account for the effect of the B_s/t_t ratio of the steel tube on the softening of the concrete.

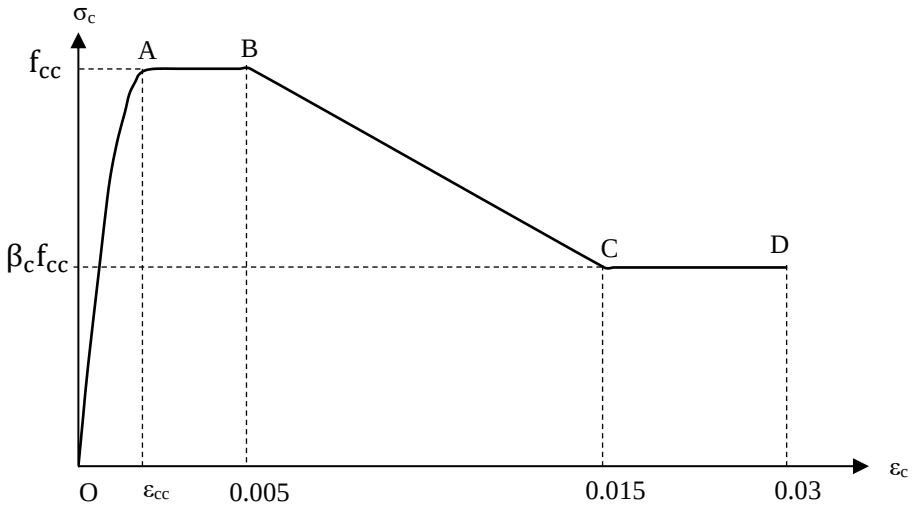

Fig. 5.4 Stress–strain curve for the confined concrete in RCFTFGs

The concrete infill is represented using 8-noded solid elements with reduced integration, known as C3D8R in the ABAQUS library, as shown in Fig. 5.3. The concrete damaged plasticity (CDP) model is employed to describe the constitutive behaviour of the material. To represent the inelastic behaviour, the CDP model uses the concept of isotropic damaged elasticity, in combination with isotropic tensile and compressive plasticity. It is assumed that the uniaxial tensile and compressive behaviours are characterized by damaged plasticity. The plasticity parameters required by the CDP model are the dilation angle, eccentricity, ratio of the strength in the triaxial state to that in the uniaxial state and the K parameter and these are taken as 36°, 0.1, 1.16 and 0.667, respectively, in the current work (Kmiecik and Kamiński, 2011).

In addition, the compressive damage parameter d_c needs to be defined at each inelastic strain level. It ranges from zero, for undamaged material, to unity, when the material can

no longer sustain any load. The value for d_c is found only for the descending branch of the stress-strain curve of concrete in compression, as given by Eqs (5.11) and (5.12):

$$d_c = 0 \qquad \text{when} \quad \varepsilon_c < \varepsilon_{cc} \tag{5.11}$$

$$d_c = \frac{f_{cc} - \sigma_c}{f_{cc}} \qquad \text{when} \quad \varepsilon_c \geq \varepsilon_{cc} \tag{5.12}$$

The tensile strength of concrete f_t is taken as 4.5 MPa (Muteb and Ali, 2016), similar to the simulation of concrete in compression in the CDP model, and the tensile damage parameter d_t, which is valid only in the descending branch of the stress-strain curve for concrete in tension, is defined at each increment of cracking strain, as described by Eqs (5.13) and (5.14):

$$d_t = 0 \qquad \text{for} \quad \varepsilon_t < \varepsilon_{cr} \tag{5.13}$$

$$d_t = \frac{f_t - \sigma_t}{f_t} \qquad \text{for} \quad \varepsilon_t \geq \varepsilon_{cr} \tag{5.14}$$

5.4 Boundary conditions, load application and solution procedure

Simply supported boundary conditions are implemented both in-plane and out-of-plane at the beam ends in the finite element model. For in-plane displacements, the vertical translations of both end sections and the longitudinal movement of one end section are restrained, but the rotations of both end sections about the major axis are unrestrained. On the other hand, out-of-plane, the lateral displacements and twist rotations of both end sections are restrained, but rotation about the minor axis and the warping displacements are unrestrained at both end sections. Owing to symmetry of the geometry and loading conditions about the mid-span, only half the girder is modelled in ABAQUS. Therefore, one end section of the model has simply supported boundary conditions and the other end section, representing the mid-span, has symmetrical boundary conditions. The boundary conditions used for the half-length FE models are shown in Fig. 5.5, in which u_x, u_y, u_z, θ_x, θ_y, and θ_z are the displacements and the rotations about the global x, y and z axes, respectively. The y-z plane is considered to be in-plane whereas the x-z and x-y planes are out-of-plane.

The implicit dynamic analysis method is employed to simulate the response, accounting for the geometric and material nonlinearities. The load is applied incrementally and the nonlinear geometry parameter (NLGEOM) is included for the large displacement analysis. This nonlinear dynamic analysis method uses an implicit time integration

scheme to calculate the transient dynamic or quasi-static response of a system, which is found in the current study to provide the best convergence behaviour owing to the high energy dissipation associated with quasi-static applications during certain stages of the loading history. Table 5.3 presents the rotation (θ) and displacement (u) constraints along the length of the girders. In this table, the symbol ● represents that measure being restrained against movement whilst ○ symbolises unrestrained. At the end of the beam (i.e. at the support), the vertical and lateral displacements (u_y and u_x, respectively) of all nodes along the y-axis (i.e., when x = 0), and the twist rotations about z and y-axes (θ_z and θ_y) are restrained against movement and therefore assigned values equal to zero. At the middle of the beam, the longitudinal displacements u_z and rotations about the x and y-axes (θ_x and θ_y) are also restrained against all movement. The loading is applied to the top surface of the beam in displacement control through two concentrated loads along the full length or one loading point when half the span is considered.

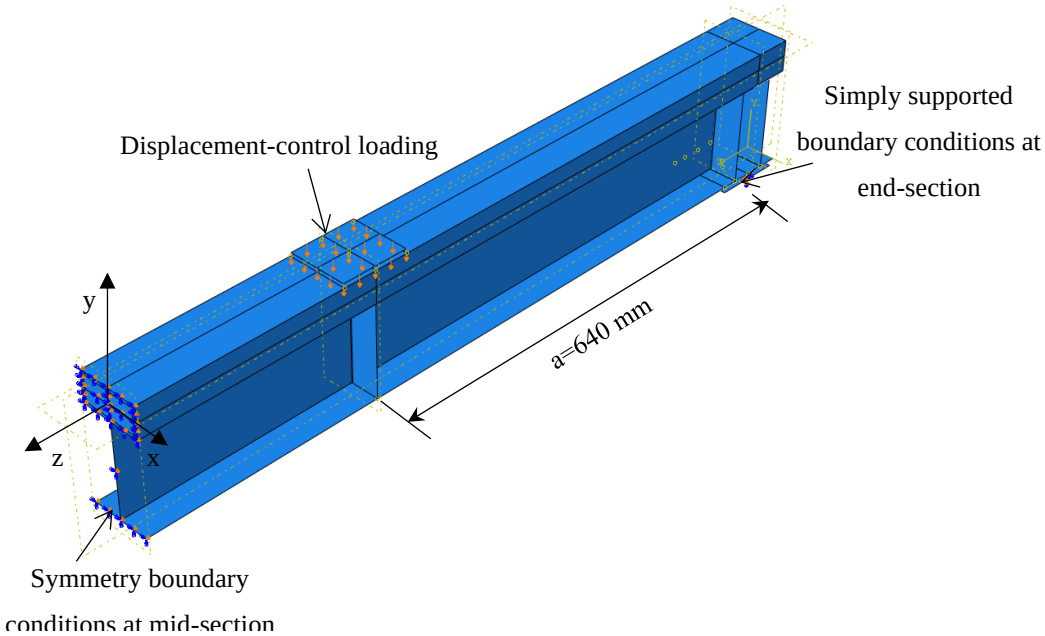

Fig. 5.5 Loading and boundary conditions in the FE model

Table 5.3 Boundary conditions of a typical RCFTFG

Boundary condition	u_x	u_y	u_z	θ_x	θ_y	θ_z
Simply support at ends	●	●	○	○	●	●
Symmetry at mid span	○	○	●	●	●	○

5.5 Initial imperfections and residual stresses

Geometric imperfections are typical in steel structures and are often introduced during production, fabrication and handling. They can be quite influential to the overall performance and are therefore included in the FE model, as shown in Fig. 5.6. The initial imperfection, obtained as the first eigenmode during an elastic buckling eigenvalue analysis, is added to the initially perfect geometry in terms of shape and amplitude. The imperfection has an amplitude of L/1000, where L is the member length, in accordance with the permitted out-of-straightness tolerance in EN 1090-2 (2008). For a RCFTFG, buckling takes place in a lateral-torsional mode as the web becomes stiffened transversally at the mid-span, causing lateral buckling to control rather than the web distortions, as shown in Fig. 5.6. On the other hand, residual stresses are not included in the current analysis in order to minimise complexity in the model, based on the findings in similar studies (Dong and Sause, 2009a).

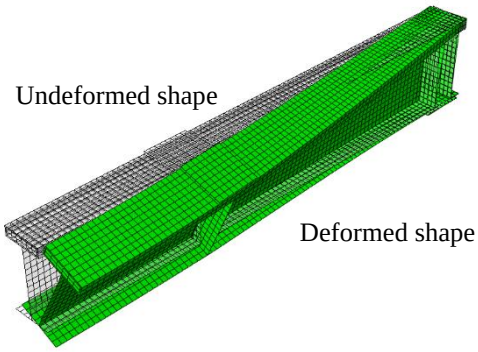

Fig. 5.6 First positive eigenmode used as the imperfection shape in the analysis of the RCFTFGs

5.6 Validation of the FE model

The accuracy of the FE model is assessed by analysing four different test specimens available in the literature (Muteb and Ali, 2016) and comparing the published results with those obtained from the FE model. The load-displacement response for both the concrete filled and the hollow rectangular flange girders are presented in Fig. 5.7. The ultimate load obtained from the FE analysis ($P_{u,FE}$) is presented together with the corresponding test value ($P_{u,Exp}$) in Table 5.1, which also includes the ratio of $P_{u,FE}$ to $P_{u,Exp}$. From Fig. 5.7, it can be seen that a good agreement is achieved between the experimental and finite element modelling results. The overall behaviour is well depicted and the load values are very closely predicted. Accordingly, it is concluded that the ABAQUS model is capable

of capturing the behaviour well for RCFTFGs in bending, and is employed to conduct more detailed parametric and validation studies, later in this chapter.

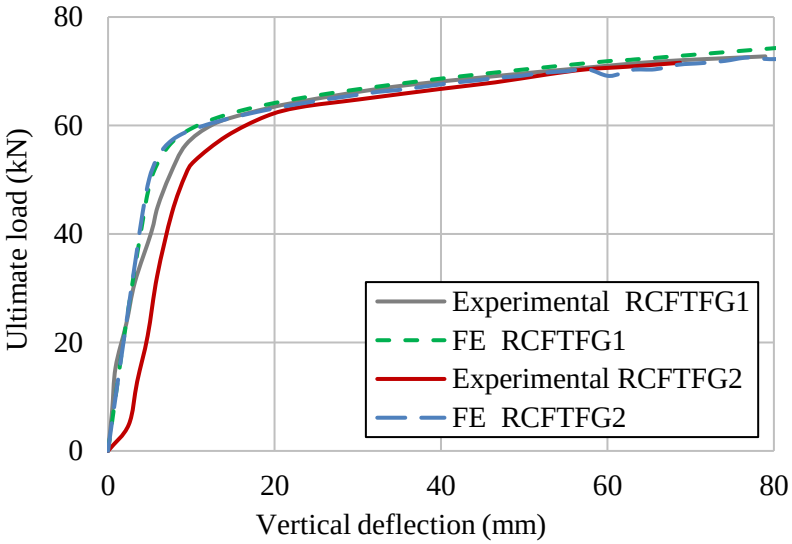

(a)

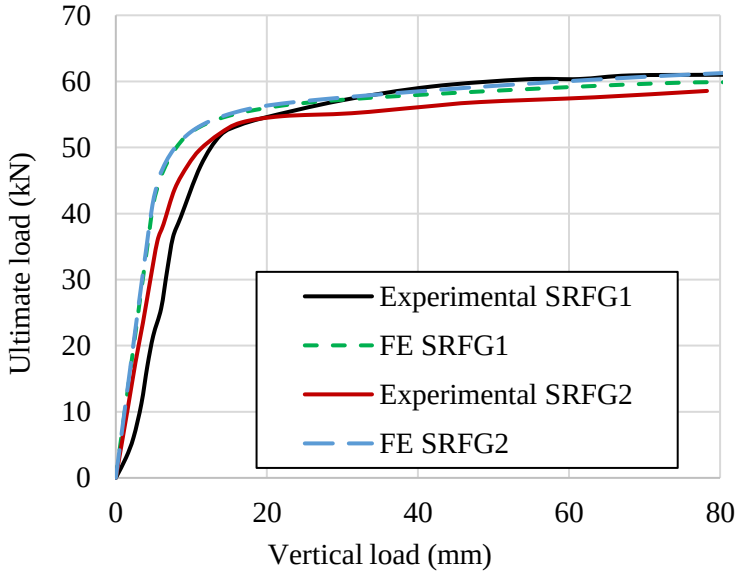

(b)

Fig. 5.7 Load versus deflection relationship from the FE analysis and experimental results including (a) RCFTFGs (b) SRFGs

5.7 Analytical design method

In this section, an analytical procedure for estimating the flexural strength of RCFTFGs is presented, based a fundamental assessment of the structural behaviour. Theoretical equations are derived based on plastic theory, in which the location of the plastic neutral

axis (PNA) and the flexural strength can be determined by applying the equilibrium of internal forces in the member. The model adopts equivalent stress blocks to represent the stress distribution in the steel and concrete and the confining effect provided by the steel tube to the concrete infill is also considered. The accuracy of the approach is examined by comparing the predictions of the equations with the FE results.

Two different cases are presented, depending on the location of the plastic neutral axis (PNA). Case 1 assumes that the PNA is in the web of the steel section while Case 2 assumes that the PNA is in the tubular flange. In order to determine the exact location of the PNA, the following assumptions are adopted:

- The term y_2, which is the vertical height of the triangular stress block is determined by interpolating the strain distribution across the cross-section, given by:

$$\frac{\varepsilon_{cc}}{y_1 - t_t} = \frac{\varepsilon_y}{y_2} \rightarrow y_2 = \frac{\varepsilon_y}{\varepsilon_{cc}}(y_1 - t_t)$$

- In the triangular stress block, where the steel is behaving in an elastic manner (i.e. $f_s = \varepsilon_s E_s$, where f_s and ε_s are the stress and strain in the steel section, respectively, and E_s is the elastic modulus), interpolation can be applied to establish that, at any location y in this region, the stress in the steel is determined as:

$$f_s = \frac{y f_y}{y_2}$$

In this expression, y_1 is the distance from the top of the cross section to the PNA. For Case 1, $y_1 > D_f$ (where D_f is the depth of the steel tube), and therefore the PNA is within the steel web. On the other hand, for Case 2, $y_1 < D_f$, and the PNA is within the concrete filled tube. The plastic moment for these two cases can be determined as described hereafter.

Case 1: PNA is in the web section ($y_1 > D_f$)

Fig. 5.8 presents the strain and stress distributions through the cross-section for Case 1, where the PNA is in the web of the steel section ($y_1 > D_f$). The internal axial force for each component of the section can be computed as shown in Table 5.4. The location of the PNA (y_1) for this case can be determined by applying the equilibrium of axial force condition, expressed in Eq. 5.15:

$$C_c + C1_{tf} + C2_{tf} + C_w = T1_w + T2_w + T_{Lf} \quad (5.15)$$

The ultimate moment (M_u) of the CFRFG section can then be calculated according to Eq. 5.16:

$$M_u = (C_c + C1_{tf} + C2_{tf}) \times y + C_w \times \frac{2}{3}(y_1 - D_f) + T1_w \times \frac{2}{3}y_2 + T2_w \times \frac{(h-y_1-y_2-t_w)}{2} + T_{Lf} \times (h - y_1 - \frac{t_f}{2}) \quad (5.16)$$

The flow chart of the procedure for calculating the position of the plastic neutral axis and the bending moment capacity is shown in Fig. 5.9.

Table 5.4 Internal force components in case the PNA exists at the web

Internal axial force component	Force equation
Compression force at infilled concrete (C_c)	$\int_{y_1-D_f+t_t}^{y_1-t_t} (B_{Tf} - 2t_t) \times \sigma_c dy$
Compression force at tubular flange ($C1_{tf}$)	$2\int_{y_2}^{y_1-t_t} t_t \times f_y dy + \int_{y_1-D_f+t_t}^{y_1} B_{Tf} \times f_y dy$
Compression force at tubular flange ($C2_{tf}$)	$2\int_{y_1-D_f+t_t}^{y_2} t_t \times f_s dy + \int_{y_1-D_f}^{y_1} B_{Tf} \times f_s dy$
Compression force at web above PNA (C_w)	$\frac{1}{2}t_w \times (y_1 - D_f) \times \frac{f_y(y_1 - D_f)}{y_2}$
Tension force at web below PNA ($T1_w$)	$\frac{1}{2} \times t_w \times y_2 \times f_y$
Tension force at web below PNA ($T2_w$)	$t_w \times (h - y_1 - y_2 - t_f) \times f_y$
Tension force at lower flange (T_{Lf})	$B_{Bf} \times t_f \times f_y$

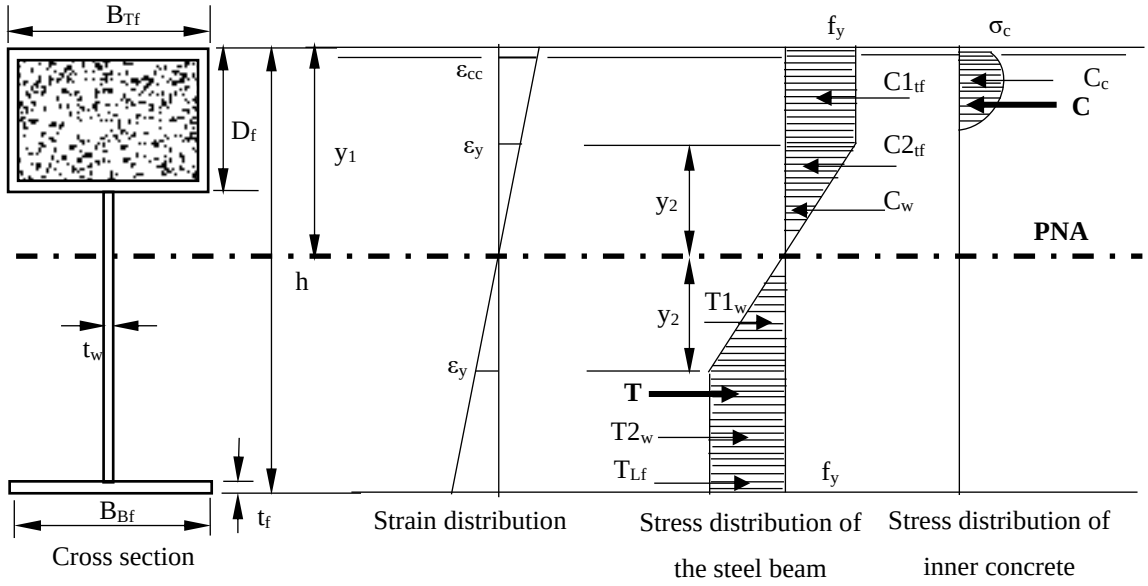

Fig. 5.8 Distributions of strain and stress for Case 1, where the PNA exists in the web of the steel section ($y_1 > D_f$)

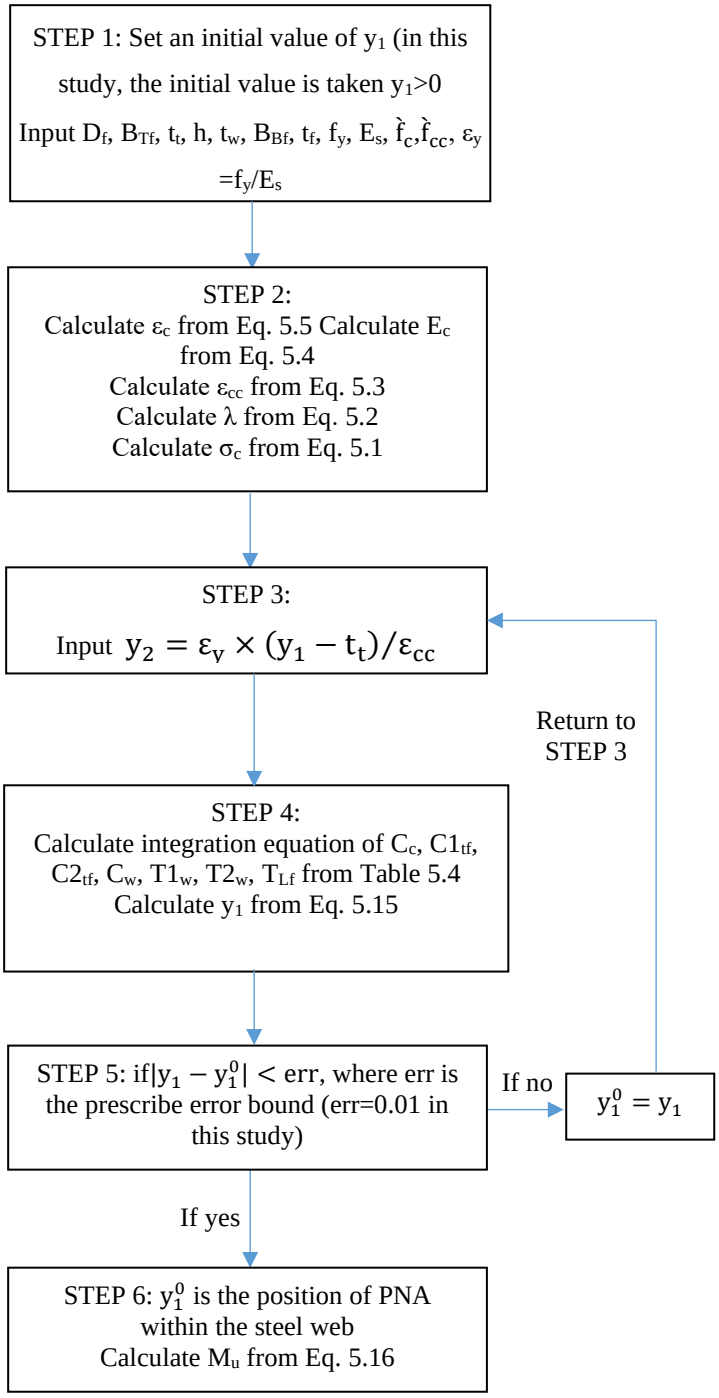

Fig. 5.9 Flow chart of the solution procedure case 1, $y_1 > D_f$

Case 2: PNA is in the tubular rectangular flange section ($y_1 < D_f$)

The internal axial force for each component of the section can be computed using the expressions presented in Table 5.5. The strain and stress distributions for Case 2 are given in Fig. 5.10, where it is shown that the PNA is in the tubular flange section ($y_1 < D_f$). It is assumed that the concrete below the PNA does not contribute to the tension capacity. The location of the PNA for this case can be determined from the equilibrium of axial forces, given as:

$$C_c + C1_{tf} + C2_{tf} = T_{tf} + T1_w + T2_w + T_{Lf} \quad (5.17)$$

Then, the ultimate moment (M_u) of the CFRFG section can be calculated as:

$$M_u = (C_c + C1_{tf} + C2_{tf} + T_{tf} + T1_w) \times y + T2_w \times ((h - y_1 - y_2 - t_f)/2 + (y_2)) + T_{Lf} \times (t_f/2 + (h - y_1 - y_2 - t_f) + (y_2)) \quad (5.18)$$

As before, Fig. 5.11 presents the different steps for calculating the position of PNA and the ultimate moment capacity.

In the equations presented in Tables 5.4 and 5.5, $C1_{tf}$ and $C2_{tf}$ represent the rectangular and triangular stress blocks for the compressive forces in the tubular flange, respectively. $T1_w$ and $T2_w$ denote the triangular and rectangular stress blocks for the tensile forces in the steel web below PNA, respectively, and σ_c is the stress in the confined concrete obtained using Eq. 5.3 earlier in this chapter.

The analytical model has been applied to the four test beams (Muteb and Ali, 2016) used before for the FE model validation, and the results are presented in Table 5.6. The ultimate moment capacity predicted using the analytical approach is denoted as $M_{u,Calc}$ whilst the corresponding value from the ABAQUS model and experimental test is $M_{u,FE}$ and $M_{u,Exp}$, respectively. There are some disparities between the experimental and numerical moment and the model somewhat over-predicts the capacity of the beam. This difference is likely to be due to a combination of factors which affect deformations, such as the idealisation of the material nonlinearity in the FE model, hardening of the steel in experimental test and as well as the likelihood of initial imperfections in the real structure. In term of analytical moment, the PNA is found to be in the web of the steel section for all of these beams and the formulations for Case 1 are therefore used. The results show that this depth of the PNA from the top of the steel sections is 37.1 and 49.4 mm for RCFTFG1 and RCFTFG2, respectively. On the other hand, for the similar members without concrete

infill, y_1 is 66.7 mm and 71.8 mm for SRFG1 and SRFG2, respectively. It is clear from the results in the table, particularly, the $M_{u,FE}$ to $M_{u,Calc}$ ratio, that the analytical approach provides a good prediction of the moment capacity for these beams, particularly for the concrete filled specimens. In this case, there is only 6% difference between the FE predictions and the capacities predicted by the simplified analytical approach.

Table 5.5 Internal force components in case the PNA exists at the tubular rectangular flange

Internal axial force component	Force equation
Compression force at infilled concrete (C_c)	$\int_{0}^{y_1-t_t} (B_{Tf} - 2t_t) \times \sigma_c \, dy$
Compression force at tubular flange above PNA ($C1_{tf}$)	$\int_{y_1-t_t}^{y_1} B_{Tf} \times f_y dy + 2\int_{y_2}^{y_1-t_t} t_t \times f_y dy$
Compression force at tubular flange above PNA ($C2_{tf}$)	$2\int_{0}^{y_2} t_t \times f_s dy$
Tension force at tubular flange below PNA (T_{tf})	$2\int_{-(D_f-t_t-y_1)}^{0} t_t \times f_s dy + \int_{-(D_f-y_1)}^{-(D_f-t_t-y_1)} B_{Tf} \times f_s dy$
Tension force at web below PNA ($T1_w$)	$\int_{-y_2}^{y_1-D_f} t_w \times f_s d_y$
Tension force at web below PNA ($T2_w$)	$(h - y_1 - y_2 - t_w) \times t_w \times f_y$
Tension force at lower flange (T_{Lf})	$B_{Bf} \times t_f \times f_y$

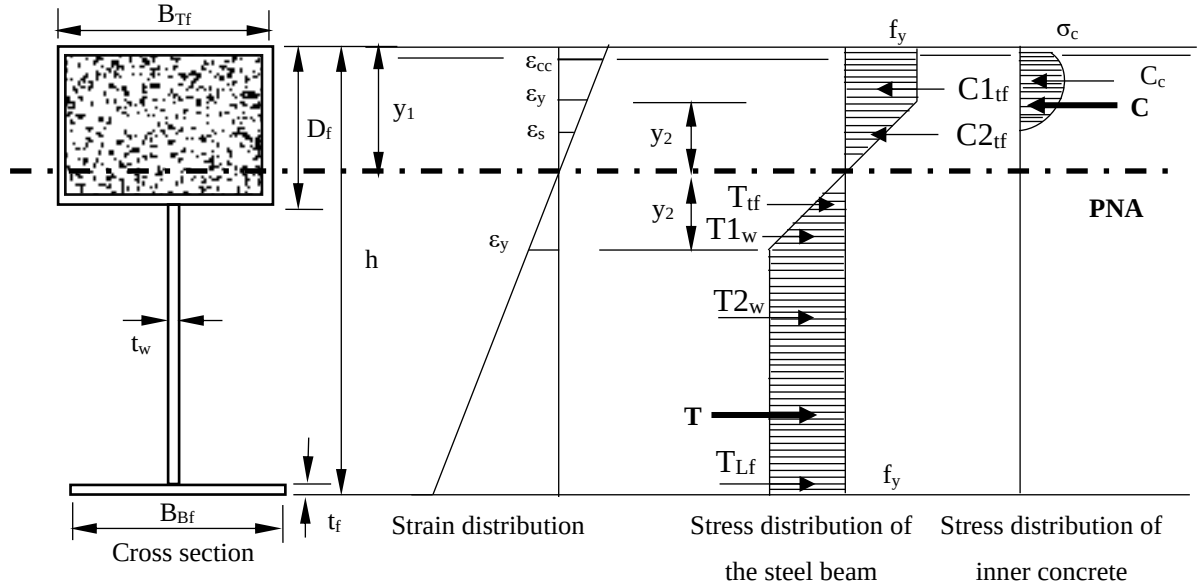

Fig. 5.10 Distributions of strain and stress for Case 2, where the PNA exists in the tubular flange section ($y_1 < D_f$)

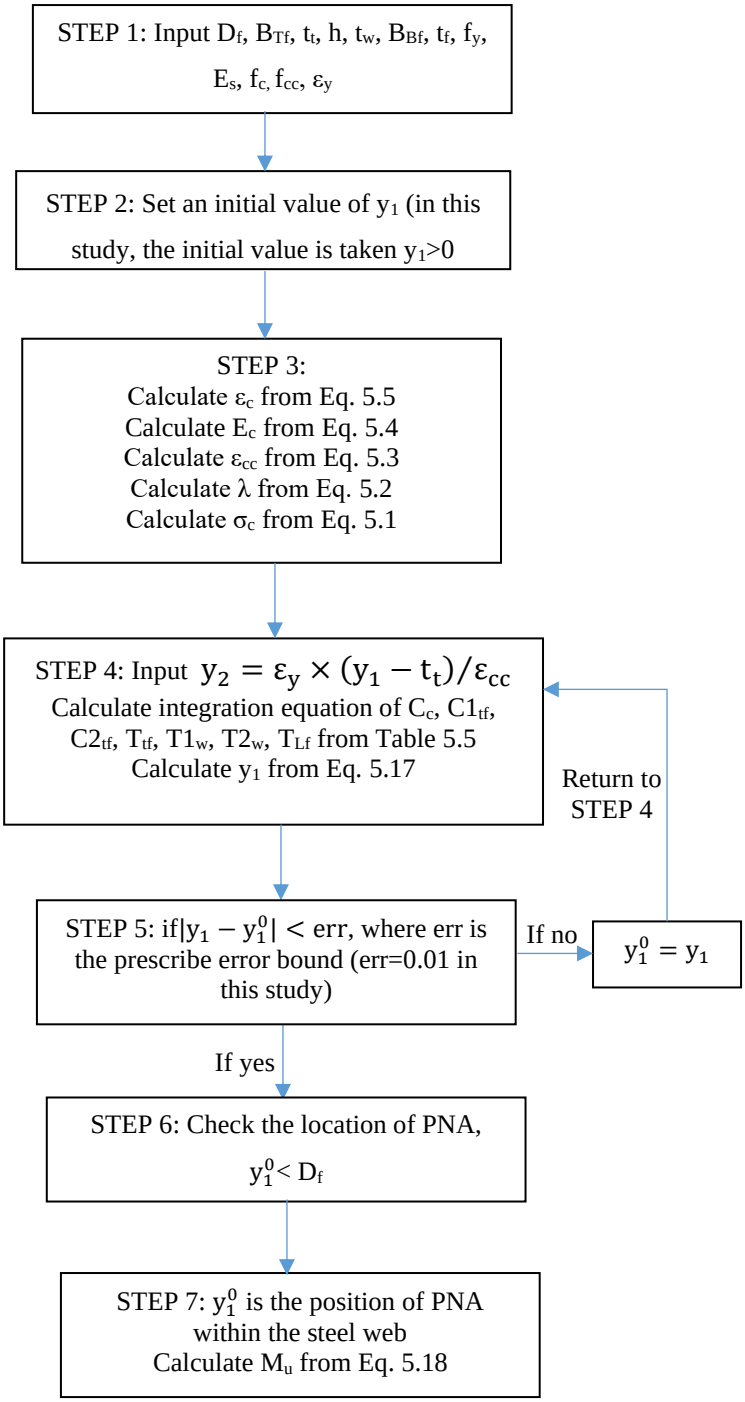

Fig. 5.11 Flow chart of the solution procedure case 2, $y_1 < D_f$

Table 5.6 Comparisons of experimental, numerical and analytical ultimate strengths

Specimen	$M_{u,Exp}$ (kNm)	$M_{u,FE}$ (kNm)	$M_{u,Calc}$ (kNm)	y_1 (mm)	$M_{u,FE}/M_{u,Calc}$
CFRFG1	23.5	18.7	19.9	37.1	0.94
CFRFG2	22.7	20.1	20.8	49.4	0.96
SRFG1	19.6	15.0	16.9	66.7	0.89
SRFG2	18.6	16.4	17.3	71.8	0.95

5.8 Parametric study

In this section, the validated FE model and simplified analytical approach are employed to conduct a parametric study to assess the influence of several salient properties on the flexural behaviour of RCFTFGs. The parameters studied are presented in Tables 5.7-5.10 and include various geometric properties such as tube thickness, depth and width as well as the thickness and depth of the web and the tension flange width and thickness. For ease of visualisation, the results are presented in two general categories. Firstly, as shown in Tables 5.7 and 5.8, members with different rectangular tube dimensions (D_f = 20, 22.3, 40 or 42.3 mm), web height (h_w taken as either 127, 147 or 250 mm), width of the bottom flange (B_{Bf} = 80 or 120 mm), thickness of the steel section (t_{beam} = 2.85 or 4 mm) and cross-sectional aspect ratios (a/h_w= 5.0, 4.4 or 2.6) are presented for both RCFTFGs (Table 5.7) and identical members without the concrete infill, i.e. SRFGs (Table 5.8). In this study, two different width-to-depth ratios (B_{Tf}/D_f =2 or 4) are studied. Tables 5.9 and 5.10 present the other parameters varied in the study, with the main focus being on the influence of steel section thickness of the various individual plate components (t_t, t_w and t_f), for RCFTFGs and SRFGs respectively.

In all cases, the webs of the girders are reinforced with double-sided flat plate stiffeners, which are 2.85 mm in thickness, and located at the support and loading points. The distance between the two intermediate stiffeners, as shown in Fig. 5.1, is 640 mm. All beams are 2020 mm in length. The specimens listed in Tables 5.7 and 5.9 are filled with concrete which has a compressive strength of 42.5 MPa. It is noteworthy that when studying the effect of steel section thickness (which is varied between 2.85 and 4 mm in this study), the area of concrete remains constant at either 2548.5 mm^2 or 1062.5 mm^2 for (D_f =20 or 40 mm), respectively. It is noted that during the FE simulation as well as experimental programme (Muteb and Ali, 2016), the failure mode for all specimens

considered is high levels of deflection, i.e. serviceability failure. The members with no concrete also exhibit a local buckling of the compression flange. Accordingly, in the current study, an allowable deflection limit of span/250 is considered as given in National Annex of Eurocode 3 (NA of BS EN 1993-1-1, 2005). In addition, all of the sections in the current study were examined for local buckling using the tube slenderness limit provided by the AASHTO LRFD specifications (1999) for rectangular tubular compression members, given in Eq. 5.19:

$$\frac{B_{Tf}}{t_t} \leq 1.7\sqrt{\frac{E_s}{f_y}} \tag{5.19}$$

This expression was originally developed for unfilled tubes, although the AASHTO specification now recommends using this check for filled concrete tubes also.

The ultimate moments determined using the FE model ($M_{u,FE}$) and the analytical expressions ($M_{u,Calc}$) are shown in Tables 5.7-5.10 together with the location of the PNA measured from the top of the section (y_1). Each pair of RCFTFGs and SRFGs had similar buckling forms, but the buckling resistance of the concrete filled members is higher than the corresponding SRFGs. For example, with reference to Tables 5.7 and 5.8, $M_{u,FE}$ is higher for GR1 (18.7 kNm) than GR17 (15.0 kNm) which are identical apart from the presence of the concrete infill in GR1. This corresponds to a 25% increase in capacity due to the presence of concrete in the tube, which increases the strength and rigidity of the upper flange and therefore allows additional loads to be carried by the concrete filled section. The load deflection and failure behaviour of both RCFTFGs and SRFGs with different key parameters are described and discussed in detail in the following sub-sections.

Table 5.7 Details of RCFTFG with different tubular flange depth

RCFTFG Group	Specimen	Geometric details							$M_{u,FE}$ (kNm)	$M_{u,Calc}$ (kNm)	PNA location, y_1 (mm)	$M_{u,FE}/M_{u,Calc}$	As (mm^2)
		t_{beam}	D_f	B_{Tf}	B_{Bf}	h_w	a/h_w	B_{Tf}/D_f					
G1	GR1	2.85	20	80	80	147	4.4	4	18.7	19.9	37.1	0.94	1185.0
	GR2	4	22.3	82.3					26.8	27.6	38.5	0.97	1681.4
	GR3	2.85	20	80		250	2.6		37.7	39.5	74.4	0.95	1478.0
	GR4	4	22.3	82.3					53.1	54.5	74.8	0.97	2092.8
G2	GR5	2.85	20	80	120	147	4.4		22.9	23.8	49.3	0.96	1299.0
	GR6	4	22.3	82.3					32.7	33.9	50.4	0.96	1841.4
	GR7	2.85	20	80		250	2.6		43.2	44.6	92.8	0.97	1592.0
	GR8	4	22.3	82.3					60.4	61.4	93.1	0.98	2252.8
G3	GR9	2.85	40	80	80	127	5.0	2	20.1	20.8	49.4	0.96	1242.0
	GR10	4	42.3	82.3					28.3	29.2	50.9	0.97	1761.4
	GR11	2.85	40	80		250	2.6		43.1	44.8	87.0	0.96	1592.0
	GR12	4	42.3	82.3					57.3	58.9	89.2	0.97	2252.8
G4	GR13	2.85	40	80	120	127	5.0		23.9	25.0	59.5	0.96	1355.5
	GR14	4	42.3	82.3					33.6	35.1	60.7	0.96	1921.4
	GR15	2.85	40	80		250	2.6		49.5	50.4	102.5	0.98	1706.0
	GR16	4	42.3	82.3					66.2	67.0	103.1	0.99	2412.8

Table 5.8 Details of SRFG with different tubular flange depth

SRFG Group	Specimen	Geometric details							$M_{u,FE}$ (kNm)	$M_{u,Calc}$ (kNm)	PNA location, y_1 (mm)	$M_{u,FE}/M_{u,Calc}$	As (mm^2)
		t_{beam}	D_f	B_{Tf}	B_{Bf}	h_w	a/h_w	B_{Tf}/D_f					
G5	GR17	2.85	20	80	80	147	4.4	4	15.0	16.9	66.7	0.89	1185.0
	GR18	4	22.3	82.3					22.4	24.7	67.6	0.91	1681.4
	GR19	2.85	20	80		250	2.6		32.9	35.1	92.5	0.94	1478.0
	GR20	4	22.3	82.3					47.3	49.4	93.4	0.96	2092.8
G6	GR21	2.85	20	80	120	147	4.4		18.4	19.6	76.3	0.94	1299.0
	GR22	4	22.3	82.3					27.5	29.2	77.9	0.94	1841.4
	GR23	2.85	20	80		250	2.6		37.9	40.0	102.7	0.95	1592.0
	GR24	4	22.3	82.3					52.8	55.1	103.6	0.96	2252.8
G7	GR25	2.85	40	80	80	127	5.0	2	16.4	17.3	71.8	0.95	1242.0
	GR26	4	42.3	82.3					23.3	24.3	72.9	0.96	1761.4
	GR27	2.85	40	80		250	2.6		36.0	36.9	102.5	0.97	1592.0
	GR28	4	42.3	82.3					52.2	53.2	103.8	0.98	2252.8
G8	GR29	2.85	40	80	120	127	5.0		19.6	19.8	81.4	0.98	1355.5
	GR30	4	42.3	82.3					27.8	28.0	82.3	0.99	1921.4
	GR31	2.85	40	80		250	2.6		41.7	42.1	110.7	0.99	1706.0
	GR32	4	42.3	82.3					58.9	59.2	113.9	0.99	2412.8

Table 5.9 Details of RCFTFG with different thicknesses

RCFTFG Group	Specimen	Geometric details							$M_{u,FE}$ (kNm)	$M_{u,Calc}$ (kNm)	PNA, y_1 (mm)	$M_{u,FE}/M_{u,Calc}$	As (mm^2)
		t_t mm	t_w mm	t_f mm	D_f mm	B_{Tf} mm	B_{Bf} mm	h_w (mm)					
G9	GR33	4	2.85	2.85	22.3	82.3	80	147	19.7	20.3	26.1	0.97	1420.2
	GR34	2.85	4	2.85	20	80			21.8	22.2	48.2	0.98	1354.0
	GR35	2.85	2.85	4	20	80			22.1	22.4	46.7	0.98	1277.0
G10	GR36	4	2.85	2.85	22.3	82.3	120	147	23.9	24.8	31.4	0.96	1534.2
	GR37	2.85	4	2.85	20	80			25.7	26.5	59.3	0.97	1468.1
	GR38	2.85	2.85	4	20	80			27.4	28.1	68.1	0.97	1437.0
G11	GR39	4	2.85	2.85	22.3	82.3	80	250	39.9	40.8	44.2	0.97	1713.3
	GR40	2.85	4	2.85	20	80			44.6	45.7	92.6	0.98	1765.5
	GR41	2.85	2.85	4	20	80			46.7	47.5	89.2	0.98	1570.0
|G12	GR42	4	2.85	2.85	22.3	82.3	120	250	45.7	46.9	56.0	0.97	1827.3
	GR43	2.85	4	2.85	20	80			49.6	50.7	106.3	0.97	1879.5
	GR44	2.85	2.85	4	20	80			52.3	52.9	116.7	0.98	1730.0
G13	GR45	4	2.85	2.85	42.3	82.3	80	127	21.8	23.3	38.8	0.93	1523.2
	GR46	2.85	4	2.85	40	80			22.7	23.9	58.3	0.95	1388.1
	GR47	2.85	2.85	4	40	80			23.3	24.4	57.4	0.95	1334.0
G14	GR48	4	2.85	2.85	42.3	82.3	120	127	25.9	26.8	45.3	0.97	1637.2
	GR49	2.85	4	2.85	40	80			26.6	27.2	67.8	0.97	1502.1
	GR50	2.85	2.85	4	40	80			28.8	29.3	74.3	0.98	1494.0
G15	GR51	4	2.85	2.85	42.3	82.3	80	250	44.4	46.8	60.5	0.95	1873.3
	GR52	2.85	4	2.85	40	80			51.0	53.6	105.6	0.95	1879.5
	GR53	2.85	2.85	4	40	80			54.4	55.6	99.3	0.98	1684.0
|G16	GR54	4	2.85	2.85	42.3	82.3	120	250	50.1	52.9	70.3	0.95	1987.3
	GR55	2.85	4	2.85	40	80			57.3	59.7	118.2	0.96	1993.5
	GR56	2.85	2.85	4	40	80			60.2	62.8	123.5	0.96	1844.0

Table 5.10 Details of SRFG with different thicknesses

SRFG Group	Specimen	Geometric details							$M_{u,FE}$ (kNm)	$M_{u,Calc}$ (kNm)	PNA, y_1 (mm)	$M_{u,FE}/M_{u,Calc}$	As (mm^2)
		t_t mm	t_w mm	t_f mm	D_f mm	B_{Tf} mm	B_{Bf} mm	h_w (mm)					
G17	GR57	4	2.85	2.85	22.3	82.3	80	147	18.2	18.9	51.6	0.96	1420.2
	GR58	2.85	4	2.85	20	80			18.4	18.9	54.8	0.97	1354.1
	GR59	2.85	2.85	4	20	80			19.0	19.6	55.4	0.97	1277.0
G18	GR60	4	2.85	2.85	22.3	82.3	120	147	22.8	23.6	58.7	0.97	1534.2
	GR61	2.85	4	2.85	20	80			21.3	21.9	69.1	0.97	1468.1
	GR62	2.85	2.85	4	20	80			23.4	23.8	83.5	0.98	1437.0
G19	GR63	4	2.85	2.85	22.3	82.3	80	250	37.4	38.1	51.7	0.98	1713.3
	GR64	2.85	4	2.85	20	80			37.2	37.4	106.3	0.99	1765.5
	GR65	2.85	2.85	4	20	80			36.3	36.3	106.8	0.99	1570.0
G20	GR66	4	2.85	2.85	22.3	82.3	120	250	43.1	45.8	71.7	0.94	1827.3
	GR67	2.85	4	2.85	20	80			40.4	41.7	120.6	0.97	1879.5
	GR68	2.85	2.85	4	20	80			40.7	42.0	134.9	0.97	1730.0
G21	GR69	4	2.85	2.85	42.3	82.3	80	127	17.6	18.7	58.1	0.94	1523.2
	GR70	2.85	4	2.85	40	80			18.4	19.4	50.6	0.95	1388.1
	GR71	2.85	2.85	4	40	80			19.2	19.7	45.4	0.97	1334.0
G22	GR72	4	2.85	2.85	42.3	82.3	120	127	22.7	23.9	65.2	0.95	1637.2
	GR73	2.85	4	2.85	40	80			21.3	22.2	64.8	0.96	1502.1
	GR74	2.85	2.85	4	40	80			23.1	23.5	73.5	0.98	1494.0
G23	GR75	4	2.85	2.85	42.3	82.3	80	250	40.6	42.3	43.7	0.96	1873.3
	GR76	2.85	4	2.85	40	80			41.3	41.9	112.1	0.98	1879.5
	GR77	2.85	2.85	4	40	80			40.2	40.6	106.8	0.99	1684.0

SRFG Group	pecimen	Geometric details							$M_{u,FE}$ (kNm)	$M_{u,Calc}$ (kNm)	PNA, y_1 (mm)	$M_{u,FE}/M_{u,Calc}$	As (mm^2)
		t_t mm	t_w mm	t_f mm	D_f mm	B_{Tf} mm	B_{Bf} mm	h_w (mm)					
G24	GR78	4	2.85	2.85	42.3	82.3	120	250	46.8	48.8	63.7	0.96	1987.3
	GR79	2.85	4	2.85	40	80			44.9	45.9	126.3	0.98	1993.5
	GR80	2.85	2.85	4	40	80			45.2	46.0	134.9	0.98	1844.0

5.8.1 Geometry of the tubular flange

The effect of a number of the most salient individual geometric properties such as rectangular tube depth (D_f), width (B_{Tf}) and thickness (t_t) are studied herein. Two different width-to-depth ratios (B_{Tf}/D_f) for the compression infilled concrete tubular flange are assessed. With reference to Fig. 5.12, the results indicate that reducing the aspect ratio of the flange has the effect of increasing the flexural capacity of the RCFTFGs. The data in Tables 5.7 and 5.8 shows that the ultimate moment for GR8 (B_{Tf}/D_f =4) is 60.4 kNm while the same value for GR16 (B_{Tf}/D_f =2) is 66.2 kNm. Similarly, the ultimate moment for GR24 (SFRG with B_{Tf}/D_f =4) is 52.8 kNm while $M_{u,FE}$ for GR32 (B_{Tf}/D_f =2) is 58.9 kNm. This demonstrates that the contribution to the overall flexural strength that is made by the tubular flange increases as the B_{Tf}/D_f ratio decreases.

The moment-deflection responses for (a) RCFTFGs and (b) SRFGs are shown in Fig. 5.12 and it is clear that decreasing the B_{Tf}/D_f ratio increases the ultimate flexural strength of the girder. The initial stiffness of the moment-deflection response is greater for members with a relatively lower B_{Tf}/D_f ratio. On the other hand, since increasing the flange depth (D_f) leads to an increase in the RCFTFG's entire cross-sectional area, it is important to assess the additional flexural strength of the girder which can be obtained. The rectangular tubular flange depth variation from 20 mm to 40 mm increases the cross-sectional steel area by around 8% (i.e. the total area for GR3 is 1478 mm^2 whereas it is 1592 mm^2 for GR11). These two beams have an ultimate moment capacity of around 37.7 kNm and 43.1 kNm for GR3 and GR11, respectively. Therefore, an 8% increase in the volume of steel can lead to a 15% increase in the bending moment capacity.

Two different tube thicknesses (t_t) are examined in this study, i.e. 2.85 mm and 4 mm. A general conclusion is that increasing the thickness of the steel tube increases the ultimate moment for RCFTFGs and SRFGs, as expected. For example, the ultimate moments are 20.1 and 21.8 kNm for GR9 (t_t=2.85 mm) and GR45 (t_t=4 mm), respectively. This improves the strength and stiffness of the compression flange and allows a 9% increase in capacity. The results show an improvement in moment when increase the steel thickness of the tube with constant area of concrete. In addition, Tables (5.7-5.10) present the variation of $M_{u,FE}/M_{u,Calc}$ for different groups of RCFTFGs and SRFGs. The values indicate the accuracy of the analytical expressions in predicting the ultimate moment as, in all cases, the $M_{u,FE}/M_{u,Calc}$ ratio is between 0.89 and 0.99.

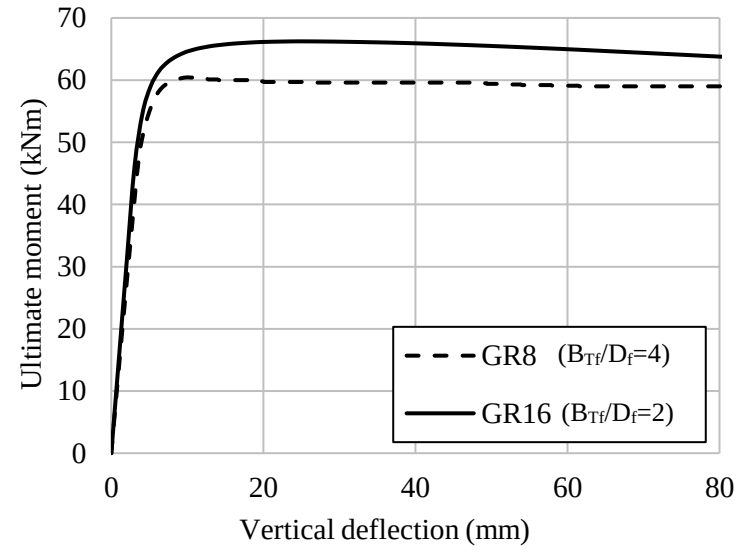

(a)

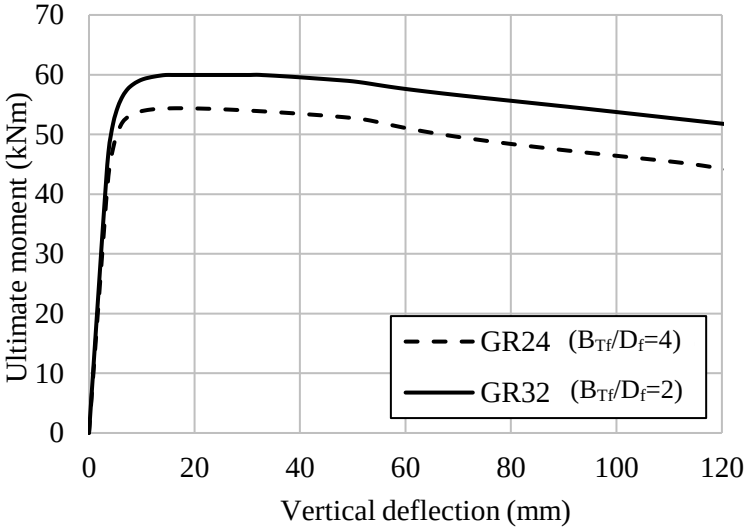

(b)

Fig. 5.12 Ultimate moment versus deflection responses for (a) RCFTFGs (b) SRFGs with different width-to-depth ratios (B_{Tf}/D_f)

5.8.2 Geometry of the steel web

Firstly, the effect of the aspect ratio of the girder web panel (a/h_w) is examined. As previously noted in Tables 5.7 and 5.8, a reduction of the aspect ratio of the web panels for the girders with otherwise identical geometries leads to an increase in the ultimate moment capacity of the member. Fig. 5.13 shows the ultimate moment-deflection curves for both types of girder and highlights the differences in their general behaviour. After the linear elastic stage and until the full strength of the girders is reached, the girder with the higher web panel aspect ratio (GR6) reaches the inelastic stress stage at a lower deflection relative to GR8 and also achieves a considerably higher flexural capacity. After

that point, the response plateaus as the displacement continues to increase with very little change in the flexural capacity. It is shown that the initial stiffness of the response in the elastic range is greater for the members with a relatively lower aspect ratio.

In order to illustrate the general behaviour of SRFGs, without a concrete infill, the moment-deflection curves of GR22 and GR24 are plotted in Figs. 5.13(b). These are identical to GR6 and GR8 mentioned above apart from having a hollow top flange. Generally, the behaviour of GR22 and GR24 are quite similar to GR6 and GR8, although the capacities are lower as expected. It is noteworthy that the capacity decreases more rapidly for the hollow members compared with the CFRFGs after the peak moment has been reached. In addition, it is shown that for members with a relatively high aspect ratio (i.e. GR6 and GR22), their ultimate bending moments are 32.7 and 27.5 kNm, respectively, representing a difference of 16%. On the other hand, the same values for GR8 and GR24 are 60.4 and 52.8 kNm, giving a difference of 12%. This show that the influence of the concrete infill is more pronounced for beams with a larger aspect ratio (i.e. GR6 and GR22).

With reference to the data presented in Tables 5.7 and 5.9, it can be seen that increasing the web thickness leads to an improvement of the flexural strength. This is evidenced by comparing GR1 (t_w=2.85 mm) with GR34 (t_w=4 mm), for example. These two beams have an ultimate moment capacity of around 18.7 kNm and 21.8 kNm, respectively, and a gross cross-sectional area (steel only) of 1185 and 1354 mm^2, respectively. Therefore, a 14% increase in steel volume results in a 17% improvement in bending moment capacity, for the same stiffener arrangement.

Similarly, it is observed in the data presented in Tables 5.7-5.10 that an increase in the web height (h_w) leads to a greater increase in the moment capacity of the RCFTFGs and SRFGs, as expected. For RCFTFGs, the ultimate moment of GR1 (h_w=147 mm) is 18.7 kNm, for example, whereas $M_{u,FE}$ for GR3 (h_w=250 mm) is 37.7 kNm. The effect of web height is further studied in Fig. 5.14 for two specimens with a web height of either 127 or 250 mm. It is observed that the initial stiffness of the curves is greater when h_w is relatively higher. Clearly, decreasing the web depth (h_w) reduces the volume of steel in the section as well as the fabrication costs as less welding is required and the associated risk of weld distortion is lowered. However, it also reduces the bending moment capacity. Therefore, this discussion highlights the importance of a careful consideration of all

factors (capacity requirements, flange depth, web depth, welding needs, etc.) when designing these types of members.

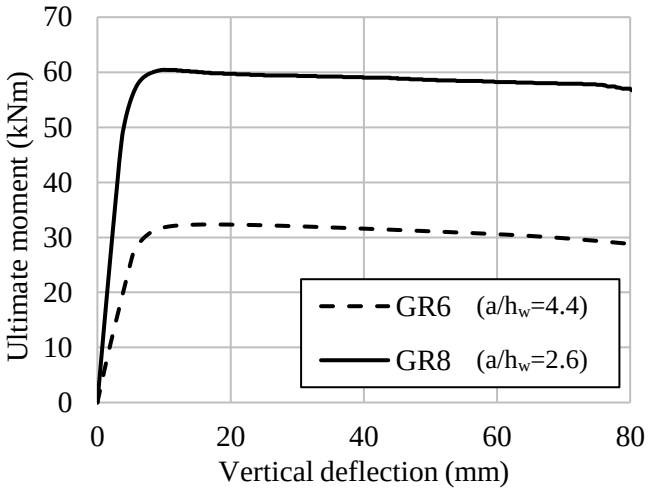

(a)

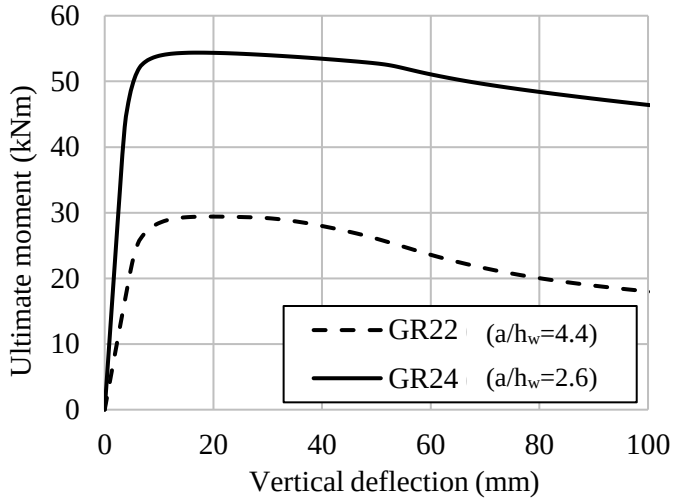

(b)

Fig. 5.13 Ultimate moment versus deflection responses for (a) RCFTFGs (b) SRFGs with difference web panel aspect ratios

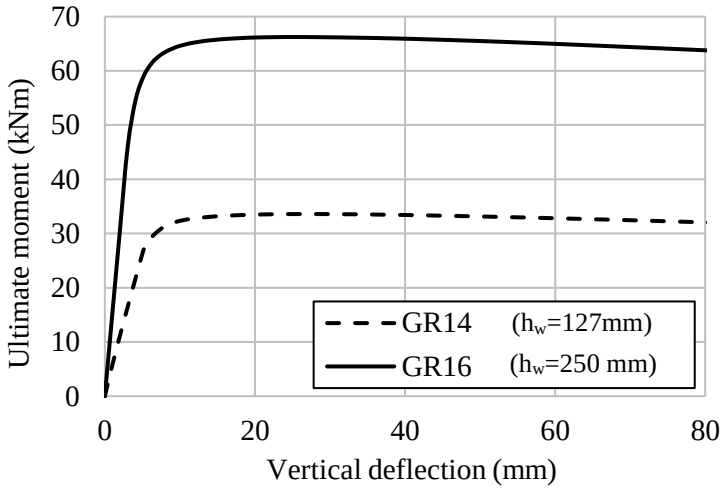

(a)

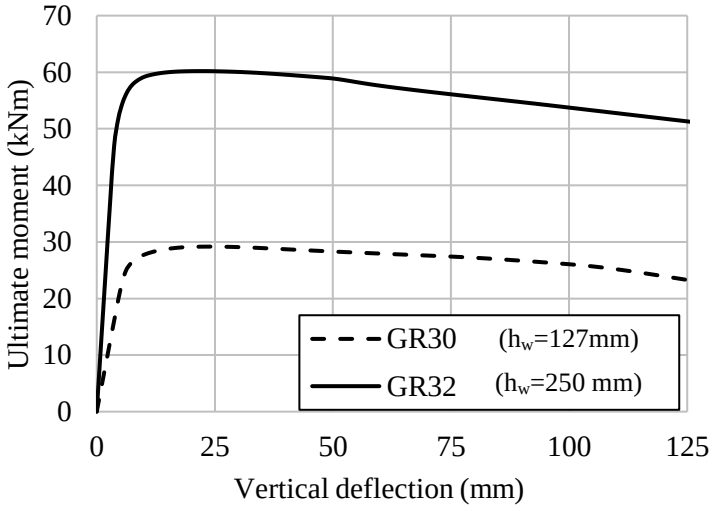

(b)

Fig. 5.14 Ultimate moment versus deflection responses for (a) RCFTFGs (b) SRFGs with difference web height

5.8.3 Geometry of the bottom flange

The effect that the width of the bottom flange (B_{Bf}) has on the structural behaviour of the RCFTFGs and SRFGs is observed in Fig. 5.15(a) and (b), respectively. Two different flange widths have been studied, namely 80 and 120 mm. It is clearly shown in the figures that a wider tension flange results in a greater second moment of area for the section and therefore increases the ultimate flexural strength. Accordingly, and as expected, the flexural capacity of both RCFTFGs and SRFGs increases for greater tension flange widths (B_{Bf}). As demonstrated in Fig. 5.15, and also the data in Tables 5.7 and 5.9, the increase in flexural capacity from GR9 and GR25, for the RCFTFG and SRFG with a

bottom flange width of 80 mm, to GR13 and GR29, which were identical except having a bottom flange width of 120 mm, is 19% and 20%, respectively, although the increase in steel area is only 9% (the total steel area in GR9 and GR25 was 1242 mm^2 whereas the same value for GR13 and GR29 is 1355.5mm^2).

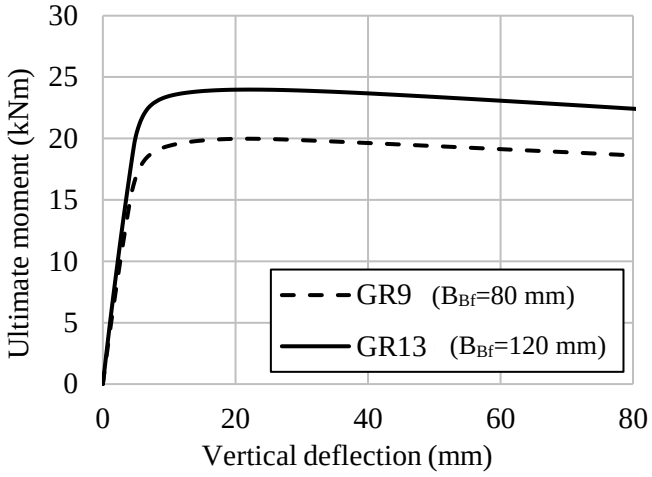

(a)

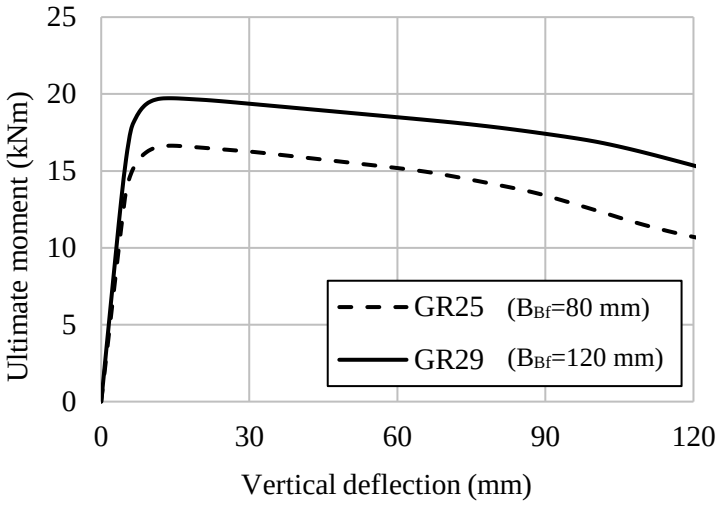

(b)

Fig. 5.15 Ultimate moment versus deflection responses for (a) RCFTFGs (b) SRFGs with difference tensile flange width

The influence of bottom flange thickness (t_f) on the capacity of the section is also investigated. With reference to Tables 5.7-5.10, for example, the ultimate moment of GR13 (t_f=2.85 mm) is 23.9 kNm whereas the same value for GR50 (t_f=4 mm) is 28.8 kNm. On the other hand, for equivalent SRFGs, these values are 19.6 kNm and 23.1 kNm for GR29 (t_t=2.85 mm) and GR74 (t_t=4 mm), respectively. Thus, changing the bottom flange thickness from 2.85 mm to 4 mm thereby increasing the total steel cross-sectional

area by 9%, results in an improved moment capacity of almost 21% and 18% for RCFTFGs and SRFGs, respectively. It is worth noting that the design of the cross-sectional properties must be carefully considered in terms of optimum thickness and width, relative to the required moment capacity, in order to provide an efficient and economical design both in terms of material and fabrication costs.

5.8.4 Concrete strength

In this section, the effect of concrete compressive strength on the response is considered by varying compressive strength values (f_c) between 20 and 80 N/mm^2 for the GR9 specimen presented in Table 5.11 (this girder is selected randomly for illustration purposes only). The data in the table shows that the f_c value has a relatively insignificant effect, which can be considered negligible, on the strength of the RCFTFGs. The ultimate moment-vertical deflection responses for these members are shown in Fig. 5.16. During the elastic phase, the concrete strength has no notable effect on the member rigidity. As expected, with greater concrete strengths, the moment capacity increases although it is quite marginal, and the PNA is located at a higher position in the cross-section. From the ratio of $M_{u,FE}$ to $M_{u,Calc}$, as presented in Table 5.11, it is evident that due to the reduced contribution of the concrete, the analytical model provides a more accurate prediction of the moment capacity for relatively low values of f_c. In general it can be concluded that the increase in capacity of the RCFTFGs compared with that of the SRFGs is attributed to the presence of a rigid medium in the upper flange, rather than directly from the concrete strength, in the range considered herein. Therefore, it is not necessary to directly include the concrete compressive strength in the design strength of RCFTFGs.

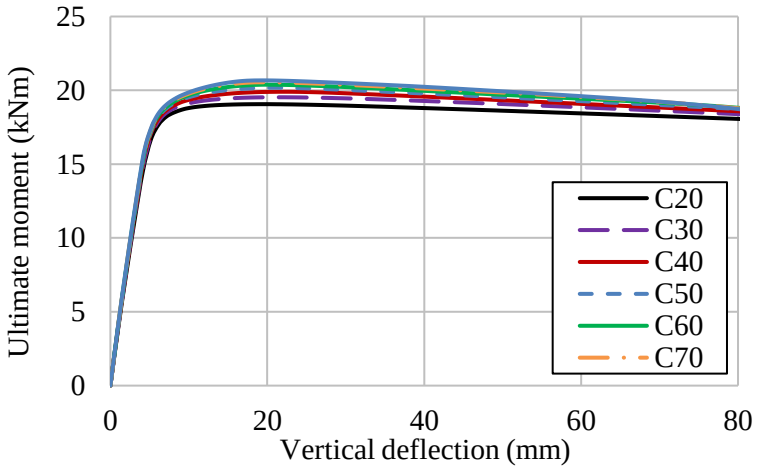

Fig. 5.16 Influence of concrete strength on the behaviour of RCFTFGs

Table 5.11 Influence of f_c and f_y on the capacity of model GR9

f_c (MPa)	f_y (N/mm^2)	$M_{u,FE}$ (kNm)	$M_{u,Calc}$ (kNm)	PNA location (mm)	$M_{u,FE}$/ $M_{u,Calc}$
20	236.8	19.1	19.4	50.3	0.98
30	236.8	19.5	20.1	49.9	0.97
40	236.8	19.8	20.6	49.5	0.96
42.5	236.8	20.1	20.8	49.4	0.96
50	236.8	20.2	21.5	49.1	0.94
60	236.8	20.4	21.9	48.8	0.93
70	236.8	20.5	22.3	48.5	0.92
80	236.8	20.7	22.7	48.0	0.91
42.5	235	19.2	20.3	47.8	0.95
42.5	236.8	20.1	20.8	49.4	0.96
42.5	355	28.8	29.7	54.6	0.97
42.5	460	36.5	37.1	58.8	0.98
42.5	690	53.1	53.6	67.9	0.99
42.5	960	71.1	71.5	80.3	0.99

5.8.5 Steel strength

It influence of the yield strength of the steel section (f_y) on the overall behaviour is assessed by varying this value between 235 and 960 N/mm^2 and the moment-deflection results are presented in Fig. 5.17 and Table 5.11. As before, the specimen GR9 is used for illustrative purposes. The results demonstrate that the ultimate bending capacity is proportional to the yield strength of steel, as expected. Moreover, the steel grade does not influence the early stages of the response, when stiffness of the member is more critical, as Young's modulus remains constant. From Table 5.11, it is clear that members with higher steel strength also have higher $M_{u,FE}/M_{u,Calc}$ ratios, which indicates that the behaviour of these members are particularly well captured by the analytical model.

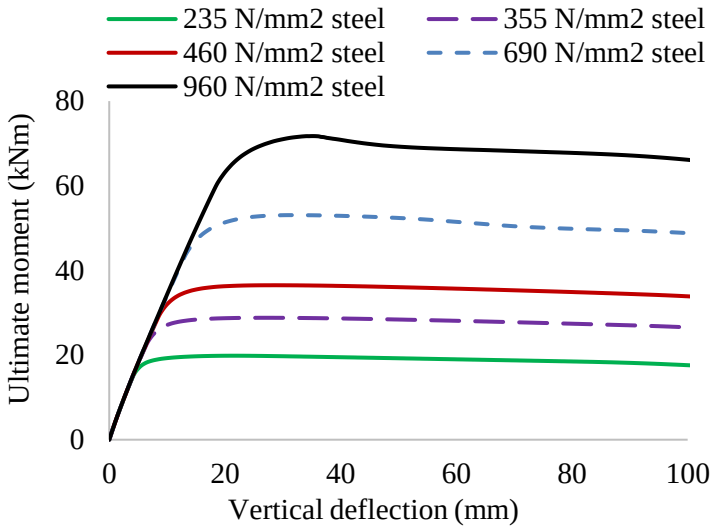

Fig. 5.17 Vertical deflection at mid-span beam with different yielding strength of steel

5.9 Concluding remarks

Both the numerical and the analytical models are employed in this chapter to conduct a detailed parametric study in order to identify and quantify the most salient and influential properties, both in terms of the flexural capacity and the overall behaviour. The key variables studied include the geometry of the different components (i.e. the compression tubular compression flange, web and bottom tension flange) and also the material strengths. The results also are compared with steel rectangular flange girders (SRFGs) which do not have the concrete infill to thoroughly investigate the difference in flexural behaviour between both types of girder. Based on the investigation, the following concluding remarks are presented:

- The analysis of the results indicate that reducing the aspect ratio of the tubular flange (B_{Tf}/D_f) increases the flexural strength of the girders.
- The flexural strengths predicted using the simplified analytical expressions show that the capacity of both RCFTFGs and SRFGs is accurate and slightly conservative.
- It has been shown clearly that a decrease in the aspect ratio of the web panel (a/h_w) results in an increase in the bending strength of the girders. Such an increase is greater for RCFTFGs compared with SRFGs. It can also be concluded that it is more significant and beneficial to increase the depth of the infilled tubular flange

($D_{f)}$ rather than decreasing the web panel aspect ratio (a/h_w) for girders that are formed from a relatively small top flange depth. Hence, design engineers should firstly work on checking the RCFTFGs formed from compression tubular flanges with relatively smaller width-to-depth ratios (B_{Tf}/D_f) and relatively big web panel aspect ratios (a/h_w) before considering larger flanges with relatively smaller aspect ratios (a/h_w).

- Finally, it is clear from the analysis presented in this paper that concrete filled tubular flange girders are a promising cross-section for heavily-loaded structural applications, providing both efficiency in terms of material usage and effectiveness in carrying large forces and moments.

Chapter 6 : Conclusions and recommendations for future work

6.1 Introduction

Two different cross-sections are studied, including circular and rectangular CFTFGs. These are complex members and their behaviour is governed by a number of inter-related parameters. The finite element models have been developed using the ABAQUS software and consider the effects of initial geometric imperfections, as well as other geometrical and material nonlinearities, on the response. In addition, the model has been further advanced to investigate the influence of combined loading on the overall response. Different combinations of tension and bending moment are studied, and the ultimate capacities and failure modes are identified and discussed. In this chapter, the key findings and conclusions from this thesis, as well as recommendations for further research following on from this work, are presented.

6.2 Conclusions from this work

Firstly, the thesis presented a detailed investigation in the behaviour of circular concrete filled tubular flange girders (CCFTFGs) under bending. A finite element model was developed using the ABAQUS software, version 6.14-4 (Simulia, 2011) to study the response and also the relative influence of the most salient parameters.

Secondly, the thesis presents the results of an extensive numerical investigation that is carried out to study the effects of axial tension applied in combination with sagging moment's for circular concrete filled tubular flange girders (CCFTFGs). A finite element model has been developed in order to investigate the combined effects. The model is then extended to account for the application of axial tension to the members and the resulting interaction diagrams are presented.

Thirdly, the flexural behaviour of concrete filled rectangular flange girders (RCFTFGs) is presented and assessed. Two different analysis techniques are developed including a numerical finite element model, developed in ABAQUS (Simulia, 2011), and also an analytical method based on the material and geometrical properties, using a plastic analysis approach. Based on the result of this study, the following conclusions can be made:

- In view of the absence of any suitable design expression in Eurocode 4 (EN 1994-1-1, 2004), the analytical design model which is developed in this paper provides appropriate predictions for the capacity of circle and rectangle CFTFGs under

bending. The model is based on a fundamental behavioural assessment which reveals the relative influence of material and geometric parameters.

- Both infilled concrete and hollow girders had similar buckling shapes, with the infilled concrete girders achieving greater buckling loads than those of the corresponding hollow section. This emphasizes the influence of the concrete infill which increases the stiffness of the upper flange and thus makes it possible for the web to carry greater moments, compared with hollow girder.
- The three-dimensional nonlinear finite element model can be used as a tool for the assessment of the nonlinear behaviour and the ultimate failure modes of CCFTFGs under combined positive bending and axial tension.
- A simplified design approach based on a linear moment–axial tension relationship is proposed for use in practice for the design of CCFTFGs.
- The reduction in moment compared with the ultimate moment (i.e. M_{FE}/M_u) increases with a relative increase in tube size and web height.
- The moment capacity of a CCFTFG is reduced under the presence of an axial tensile force acting in the steel beam section but this is not a major issue within the realistic range of applied axial loads (up to 50% of N_u).

6.3 Responding to the research objectives

The objectives for this research project were set out in Chapter 1. Following the work which has been described herein, the following responses to these conclusions are made:

- Using cross-sectional analyses, the fundamental structural behaviour of CFTFGs, including plastic neutral axis position, yield moment, and cross-section flexural strength can be accurately calculated.
- The detailed structural behaviour of CFTFGs, including the flexural strength under the combined effects of positive bending and axial tension and the moment-axial load interaction curves, can be accurately estimated using the FE models.
- The advantages of CFTFGs are clear and their usage has increased in buildings and bridges as a result, particularly for heavily loaded applications, and this will be further aided through the design guidance provided in this work.
- The design recommendations presented in this thesis are shown to be conservative for the flexural design of CFTFGs.
- For CFTFGs, an increase in the bottom flange thickness is advantageous in terms of the moment capacity and also the material costs. This is because the increase

in moment capacity achieved is disproportionately large, compared with the increase in the cross-sectional area.

6.4 Recommendations for future work

Based on the work conducted in this thesis, a number of areas which would benefit from more research in the future have been identified. These are summarised hereafter:

- Study the influinial parameters of multiple girders systems are required to fully investigate the behaviour of CFTFGs bridge systems.
- Girders with a concrete deck are required to study CFTFGs behaviour under different loading conditions.
- This research focused on CFTFGs for simple supported beam. Similar studies of CFTFGs for continuous span and curved CFTFGs bridges are needed.
- For CFTFGs composite and non-composite with deck, a complete welding procedure should be established to splicing the tubes as needed.
- In the FE parametric study, residual stresses are not included in the steel. Therefore, a FE parametric study of the flexural strength of CFTFGs considering the residual stresses in the steel should be conducted. The results of this study should be compared with the design flexural strength formulas proposed in this thesis.
- The effects of axial tension applied in combination with sagging moment's for concrete filled tubular flange girders (CFTFGs) is not investigated experimentally in this research. Therefore, it is recommended that laboratory experiments be conducted to investigate the combination of bending and tensile axial force of circular and rectangular CFTFGs. The recommended experiments should use test specimens with a simply supported beam and stiffened webs.

References

AASHTO LRFD Bridge design specifications, 1998. American association of state highway and transportation officials. Washington. DC, USA.

AASHTO LRFD Bridge design specifications, 2004. American association of state highway and transportation officials. Washington. DC, USA.

AISC (American Institute of Steel Construction), 2005. Specification for structural steel buildings. AISC 360-05, Chicago, USA.

AISC (American Institute of Steel Construction), 1999. Load and resistance factor design specification, for structural steel buildings. Chicago, USA.

Akay, H.U., Johnson, C.P. and Will, K.M., 1977. Lateral and local buckling of beams and frames. Journal of the Structural Division, 103(ASCE 13226).

Al-Dujele, R., Cashell, K.A. and Afshan, S., 2018. Flexural behaviour of concrete filled tubular flange girders. Journal of Constructional Steel Research, 151, pp.263-279.

Al-Dujele R., Cashell K.A., 2018a. Numerical analysis of the flexural behaviour of concrete-filled rectangular flange girders. Proceedings of 20th International Conference on Civil, Structural and Construction Engineering (ICCSCE), Paris, France, pp. 913-917.

Al-Dujele R., Cashell K.A., 2018b. An extended evaluation for flexural behaviour of concrete-filled rectangular flange girders. Proceedings of 9th International Conference on Advances in Steel Structures (ICASS), Hong Kong, China.

Al-Dujele R., Cashell K.A., 2019. The effects of axial tension on the sagging-moment regions of concrete-filled tubular flange girders. Proceedings of 9th International Conference on Steel and Aluminium Structures (ICSAS), Bradford, UK.

Anapayan, T., Mahendran, M. and Mahaarachchi, D., 2011a. Lateral distortional buckling tests of a new hollow flange channel beam. Thin-Walled Structures, 49(1), pp.13-25.

Anapayan, T., Mahendran, M. and Mahaarachchi, D., 2011b. Section moment capacity tests of LiteSteel beams. Thin-Walled Structures, 49(4), pp.502-512.

Anapayan, T. and Mahendran, M., 2012. Numerical modelling and design of LiteSteel Beams subject to lateral buckling. Journal of Constructional Steel Research, 70, pp.51-64.

Anapayan, T., 2010. Flexural behaviour and design of hollow flange steel beams. Doctoral dissertation, Queensland University of Technology.

Avery, P., Mahendran, M. and Nasir, A., 2000. Flexural capacity of hollow flange beams. Journal of Constructional Steel Research, 53(2), pp.201-223.

Avery, P. and Mahendran, M., 1997. Finite-element analysis of hollow flange beams with web stiffeners. ASCE Journal of structural engineering, 123(9), pp.1123-1129.

Ban, H. and Bradford, M.A., 2013. Flexural behaviour of composite beams with high strength steel. Engineering Structures, 56, pp.1130-1141.

Bradford, M.A. and Trahair, N.S., 1979. Distortional buckling of I-beams (No. Res Rpt No R353 Monograph).

CEN E, 2008. 1090-2: execution of steel structures and aluminium structures–part 2: technical requirements for steel structures. European Committee for Standardisation, Brussels.

Chen, J. and Jin, W.L., 2010. Experimental investigation of thin-walled complex section concrete-filled steel stub columns. Thin-Walled Structures, 48(9), pp.718-724.

Cheyrezy, M. and Combault, J., 1990. Composite bridges with corrugated webs-Achievements and prospects. Proc. IABSE symp., Brussels, pp. 479-484. Zurich: IABSE.

Choo, K.M., 1987. Buckling Program BASP for Use of a Microcomputer. MS Thesis, Department of Civil Engineering, the University of Texas at Austin.

Cuong, B.H., Tuyen, N.M. and Cuong, N.Q., 2016. Flexural-torsional buckling of mono-symmetrical I-section beam with hollow flange. Journal of Science and Technology in Civil Engineering (STCE)-NUCE, 10(5), pp.11-18.

Dabrowski, R., 1968. Curved Thin Walled Girders, Theory and Analysis. Cement and Concrete Association, London, England.

Dai, X. and Lam, D., 2010. Axial compressive behaviour of stub concrete-filled columns with elliptical stainless steel hollow sections. Steel and Composite Structures, 10(6), pp.517-539.

De Oliveira, W.L.A., De Nardin, S., de Cresce El, A.L.H. and El Debs, M.K., 2009. Influence of concrete strength and length/diameter on the axial capacity of CFT columns. Journal of Constructional Steel Research, 65(12), pp.2103-2110.

Dempsey, R.I., 1990. Structural behaviour and design of hollow flange beams. In Second National Structural Engineering Conference 1990: Preprints of Papers (p. 327). Institution of Engineers, Australia.

Ding, Y., Zhang, Y. and Zhao, J., 2009. Tests of hysteretic behavior for unbonded steel plate brace encased in reinforced concrete panel. Journal of Constructional Steel Research, 65(5), pp.1160-1170.

Dong, J. and Sause, R., 2009a. Flexural strength of tubular flange girders. Journal of Constructional Steel Research, 65(3), pp.622-630.

Dong, J. and Sause, R., 2009b. Behavior of hollow tubular-flange girder systems for curved bridges. ASCE Journal of structural engineering, 136(2), pp.174-182.

Dong, J. and Sause, R., 2010. Finite element analysis of curved steel girders with tubular flanges. Engineering Structures, 32(1), pp.319-327.

Dong, J., 2008. Analytical study of horizontally curved hollow tubular flange girders. ATLSS Report 08-15, ATLSS Engineering Research Centre, Lehigh University, Bethlehem, PA.

El Hadidy, A.M., Hassanein, M.F. and Zhou, M., 2018. The effect of using tubular flanges in bridge girders with corrugated steel webs on their shear behaviour–A numerical study. Thin-Walled Structures, 124, pp.121-135.

Elgaaly, M., Hamilton, R.W. and Seshadri, A., 1996. Shear strength of beams with corrugated webs. ASCE Journal of Structural Engineering, 122(4), pp.390-398.

Elgaaly, M., Seshadri, A. and Hamilton, R.W., 1997. Bending strength of steel beams with corrugated webs. ASCE Journal of Structural Engineering, 123(6), pp.772-782.

El-Khoriby, S.R., Hassanein, M.F., Kharoob, O.F., El Hadidy, A.M. and Alnaggar, G.A.N., 2016. Tubular flange plate girders with corner square web openings in the panel of maximum shear: Strength and behaviour. Thin-Walled Structures, 99, pp.142-154.

Ellobody, E., Young, B. and Lam, D., 2006. Behaviour of normal and high strength concrete-filled compact steel tube circular stub columns. Journal of Constructional Steel Research, 62(7), pp.706-715.

Ellobody, E. and Young, B., 2006. Nonlinear analysis of concrete-filled steel SHS and RHS columns. Thin-walled structures, 44(8), pp.919-930.

Ellobody, E., 2013. Numerical modelling of fibre reinforced concrete-filled stainless steel tubular columns. Thin-Walled Structures, 63, pp.1-12.

EN 1992-1-1, 2004. Eurocode 2: Design of Concrete Structures: Part 1-1: General Rules and Rules for Buildings.

EN1994-1-1, 2004. Eurocode 4: Design of Composite Steel and Concrete Structures. Part 1-1: General Rules and Rules for Buildings, CEN, Brussels.

Fan, Z., 2007. Behavior of horizontally curved steel tubular-flange bridge girders. Ph.D. Dissertation, Department of Civil and Environmental Engineering, Lehigh University, Bethlehem, PA.

Ge, H.B. and Usami, T., 1994. Strength analysis of concrete-filled thin-walled steel box columns. Journal of Constructional Steel Research, 30(3), pp.259-281.

Gao, F., Zhu, H.P., Zhang, D.H. and Fang, T.S., 2014. Experimental investigation on flexural behavior of concrete-filled pentagonal flange beam under concentrated loading. Thin-Walled Structures, 84, pp.214-225.

Giakoumelis, G. and Lam, D., 2004. Axial capacity of circular concrete-filled tube columns. Journal of Constructional Steel Research, 60(7), pp.1049-1068.

Goode, C.D. and Lam, D., 2011. Concrete-filled steel tube columns-tests compared with Eurocode 4. International Conference on Composite Construction in Steel and Concrete, vol. VI, ASCE, Reston (pp. 317-325).

Hamada, M., Nakayama, K., Kakihara, M., Sato, K. and Ohtake, F., 1983. Development of welded I-beam with corrugated web. Bull. Jpn. Inst. Met., 22(6), pp.528-530.

Hampe, K.M., 2012. Analysis and Design of Test Setup and Loading Fixture for Horizontally Curved Tubular Flange Girder Test Specimen. Ph.D. Dissertation, Department of Civil and Environmental Engineering, Lehigh University, Bethlehem, PA.

Han, L.H., Yao, G.H. and Tao, Z., 2007. Performance of concrete-filled thin-walled steel tubes under pure torsion. Thin-Walled Structures, 45(1), pp.24-36.

Han, L.H., Li, W. and Bjorhovde, R., 2014. Developments and advanced applications of concrete-filled steel tubular (CFST) structures: Members. Journal of Constructional Steel Research, 100, pp.211-228.

Harries, K.A. and Kharel, G., 2003. Experimental investigation of the behavior of variably confined concrete. Cement and Concrete research, 33(6), pp.873-880.

Hancock, G.J., 2003. Cold-formed steel structures. Journal of constructional steel research, 59(4), pp.473-487.

Hassanein, M.F. and Kharoob, O.F., 2012. An extended evaluation for the shear behavior of hollow tubular flange plate girders. Thin-Walled Structures, 56, pp.88-102.

Hassanein, M.F. and Kharoob, O.F., 2010. Shear strength and behavior of transversely stiffened tubular flange plate girders. Engineering Structures, 32(9), pp.2617-2630.

Hassanein, M.F. and Kharoob, O.F., 2013. Shear capacity of stiffened plate girders with compression tubular flanges and slender webs. Thin-Walled Structures, 70, pp.81-92.

Hassanein, M.F., 2014. Shear strength of tubular flange plate girders with square web openings. Engineering Structures, 58, pp.92-104.

Hassanein, M.F. and Silvestre, N., 2013. Lateral–distortional buckling of hollow tubular flange plate girders with slender unstiffened webs. Engineering Structures, 56, pp.572-584.

Hassanein, M.F., 2015. Fundamental behaviour of concrete-filled pentagonal flange plate girders under shear. Thin-Walled Structures, 95, pp.221-230.

Homma, K. and Sause, R., 1995. Potential for high performance steel in plate-girder bridges. In Restructuring: America and Beyond (pp. 177-192), ASCE.

Hrennikoff, A., 1941. Solution of problems of elasticity by the framework method. J. appl. Mech.

Hu, H.T., Huang, C.S., Wu, M.H. and Wu, Y.M., 2003. Nonlinear analysis of axially loaded concrete-filled tube columns with confinement effect. ASCE Journal of Structural Engineering, 129(10), pp.1322-1329.

Hu, H.T. and Schnobrich, W.C., 1989. Constitutive modeling of concrete by using nonassociated plasticity. ASCE Journal of Materials in Civil Engineering, 1(4), pp.199-216.

Hu, H.T., Huang, C.S. and Chen, Z.L., 2005. Finite element analysis of CFT columns subjected to an axial compressive force and bending moment in combination. Journal of Constructional Steel Research, 61(12), pp.1692-1712.

Huang, C.S., Yeh, Y.K., Liu, G.Y., Hu, H.T., Tsai, K.C., Weng, Y.T., Wang, S.H. and Wu, M.H., 2002. Axial load behavior of stiffened concrete-filled steel columns. ASCE Journal of Structural Engineering, 128(9), pp.1222-1230.

Ibrahim, S.A., El-Dakhakhni, W.W. and Elgaaly, M., 2006. Behavior of bridge girders with corrugated webs under monotonic and cyclic loading. Engineering Structures, 28(14), pp.1941-1955.

Kharoob, O.F., 2017. Flexural strength of steel plate girders with a tubular compression flange. Proceedings of the Institution of Civil Engineers-Structures and Buildings, 170(3), pp.180-189.

Keerthan, P., Hughes, D. and Mahendran, M., 2014. Experimental studies of hollow flange channel beams subject to combined bending and shear actions. Thin-Walled Structures, 77, pp.129-140.

Keerthan, P. and Mahendran, M., 2011. New design rules for the shear strength of LiteSteel beams. Journal of Constructional Steel Research, 67(6), pp.1050-1063.

Keerthan, P., 2010. Shear behaviour and design of litesteel beams. Ph.D. dissertation, Department of Faculty of Environmental and Engineering, Queensland University of Technology, Australia.

Kim, B.G. and Sause, R., 2005. High performance steel girders with tubular flanges (ATLSS Report 05–15). Bethlehem, PA: ATLSS Engineering Research Center, Lehigh University.

Kim, B.G. and Sause, R., 2008. Lateral torsional buckling strength of tubular flange girders. ASCE Journal of structural engineering, 134(6), pp.902-910.

Kirkland, B., 2014. Behaviour and design of composite steel-concrete beams subjected to flexure and axial load. Thesis (Ph.D.) University of Western Sydney, Australia.

Kmiecik, P. and Kamiński, M., 2011. Modelling of reinforced concrete structures and composite structures with concrete strength degradation taken into consideration. Archives of civil and mechanical engineering, 11(3), pp.623-636.

Knowles, R.B. and Park, R., 1969. Strength of concrete filled steel tubular columns. Journal of the structural division, 95(12), pp.2565-2588.

Kovac, B., 2010. Structural response of circular concrete filled tube piers in integral bridges. Master's thesis, Universitat Politècnica de Catalunya.

Kwon, G., Engelhardt, M.D. and Klingner, R.E., 2010. Experimental behavior of bridge beams retrofitted with postinstalled shear connectors. ASCE Journal of Bridge Engineering, 16(4), pp.536-545.

Lam, D. and Testo, N., 2011. Structural design of concrete filled steel elliptical hollow sections. ASCE International Conference on Composite Construction in Steel and Concrete VI (pp. 252-262).

Lee, S.H., Uy, B., Kim, S.H., Choi, Y.H. and Choi, S.M., 2011. Behavior of high-strength circular concrete-filled steel tubular (CFST) column under eccentric loading. Journal of Constructional Steel Research, 67(1), pp.1-13.

Levy, S., 1947. Computation of influence coefficients for aircraft structures with discontinuities and sweepback. Journal of the aeronautical Sciences, 14(10), pp.547-560.

Levy, S., 1953. Structural analysis and influence coefficients for delta wings. Journal of the Aeronautical Sciences, 20(7), pp.449-454.

Liang, Q.Q., 2009. Performance-based analysis of concrete-filled steel tubular beam–columns, Part I: Theory and algorithms. Journal of Constructional Steel Research, 65(2), pp.363-372.

Ma, H.Y., 2014. Analytical and experimental study on horizontally curved bridges with tubular top flange girders. Doctoral dissertation, Department of Civil and Environmental Engineering, Lehigh University, Bethlehem, PA.

Mander, J.B., Priestley, M.J. and Park, R., 1988. Theoretical stress-strain model for confined concrete. ASCE Journal of structural engineering, 114(8), pp.1804-1826.

Martin, H.C., 1961. Plane elasticity problems and the direct stiffness method. The trend in Engineering, 13, pp.5-19.

McHenry, D., 1943. A lattice analogy for the solution of stress problems. Journal of the Institution of Civil Engineers, 21(2), pp.59-82.

Mohebkhah, A. and Azandariani, M.G., 2015. Lateral–torsional buckling of Delta hollow flange beams under moment gradient. Thin-Walled Structures, 86, pp.167-173.

Mollazadeh M. H., 2015. Load Introduction into Concrete Filled Steel Tubular Columns. Doctoral dissertation, the University of Manchester.

Muteb, H. and Ali, A., 2016. Experimental and Finite Element Analysis of Lateral Torsional Buckling of Concrete Filled Tubular Flange Steel Girders. Journal of Civil and Environmental Research, Vol.8, No.4.

Nakamura, S.I., Momiyama, Y., Hosaka, T. and Homma, K., 2002. New technologies of steel/concrete composite bridges. Journal of Constructional Steel Research, 58(1), pp.99-130.

NA of BS EN 1993-1-1, 2005. UK National Annex to Eurocode 3: Design of Steel Structures Part 1-1: General rules and rules for buildings.

NSBA (National Steel Bridge Alliance), 2012. Prize Bridge Awards. Modern Steel Construction, pp. 47.

O'Connor, C., Goldsmith, P.R. and Ryall, J.T., 1965. The reinforcement of slender steel beams to improve beam buckling strength. Civil Engineering Transactions, CE7, 11, pp.29-37.

Ollgaard, J.G., Slutter, R.G. and Fisher, J.W., 1971. Shear strength of stud connectors in lightweight and normal weight concrete. AISC Eng'g Jr., April 1971 (71-10).

Pi, Y.L., Bradford, M.A. and Trahair, N.S., 2000. Inelastic analysis and behavior of steel I-beams curved in plan. ASCE Journal of Structural Engineering, 126(7), pp.772-779.

Pi, Y.L. and Bradford, M.A., 2001. Strength design of steel I-section beams curved in plan. ASCE Journal of Structural Engineering, 127(6), pp.639-646.

Pi, Y.L. and Trahair, N.S., 1997a. Lateral-distortional buckling of hollow flange beams. ASCE Journal of Structural Engineering, 123(6), pp.695-702.

Pi, Y.L. and Trahair, N.S., 1997b. Nonlinear elastic behavior of I-beams curved in plan. ASCE Journal of Structural Engineering, 123(9), pp.1201-1209.

Putnam, E., 2010. Design, experimental, and analytical study of a horizontally curved tubular flange girder. MSc thesis, Department of Civil and Environmental Engineering, Lehigh University, Bethlehem, PA.

Richart, F.E., Brandtzaeg, A. and Brown, R.L., 1928. A study of the failure of concrete under combined compressive stresses. University of Illinois at Urbana Champaign, College of Engineering. Engineering Experiment Station.

Saenz, L.P., 1964. Equation for the stress–strain curve of concrete (Discussion). Journal of the American Concrete Institute, 61(9), pp.1229-1235.

Sause, R., 2015. Innovative steel bridge girders with tubular flanges. Structure and Infrastructure Engineering, 11(4), pp.450-465.

Sause, R. and Fisher, J.W., 1996. Application of high-performance steel in bridges. In Proc., 12th US-Japan Bridge Engineering Workshop (pp. 317-331).

Schneider, S.P., 1998. Axially loaded concrete-filled steel tubes. ASCE Journal of structural Engineering, 124(10), pp.1125-1138.

Schumacher, A., Nussbaumer, A. and Hirt, M.A., 2001. Fatigue behaviour of welded circular hollow section (CHS) joints in bridges. In tubular structures-international symposium (Vol. 9, pp. 291-298).

Sennah, K.M. and Kennedy, J.B., 2002. Literature review in analysis of box-girder bridges. ASCE Journal of Bridge Engineering, 7(2), pp.134-143.

Shams, M. and Saadeghvaziri, M.A., 1997. State of the art of concrete-filled steel tubular columns. Structural Journal, 94(5), pp.558-571.

Shanmugam, N.E. and Lakshmi, B., 2001. State of the art report on steel–concrete composite columns. Journal of constructional steel research, 57(10), pp.1041-1080.

Shao, Y. and Wang, Y., 2017. Experimental study on static behavior of I-girder with concrete-filled rectangular flange and corrugated web under concentrated load at mid-span. Engineering Structures, 130, pp.124-141.

Shao, Y.B. and Wang, Y., 2016. Experimental study on shear behavior of I-girder with concrete-filled tubular flange and corrugated web. Steel and Composite Structures, 22(6), pp.1465-1486.

Simulia, 2011. ABAQUS Theory Manual. Version 6.14-4, Dassault Systems.` `

Standard Australia code, 2004. Composite structures part I: Simply supported beams. AS 2327.1, Sydney.

Susantha, K.A.S., Ge, H. and Usami, T., 2001. Uniaxial stress–strain relationship of concrete confined by various shaped steel tubes. Engineering Structures, 23(10), pp.1331-1347.

Szewczak, R.M., Smith, E.A. and DeWolf, J.T., 1983. Beams with torsional stiffeners. ASCE Journal of Structural Engineering, 109(7), pp.1635-1647.

Takabatake, H., 1988. Lateral buckling of I beams with web stiffeners and batten plates. International journal of solids and structures, 24(10), pp.1003-1019.

Tomii, M. and Sakino, K., 1979. Elasto-plastic behavior of concrete filled square steel tubular beam-columns. Transactions of the Architectural Institute of Japan, 280, pp.111-122.

Turner, M.J., 1956. Stiffness and deflection analysis of complex structures. journal of the Aeronautical Sciences, 23(9), pp.805-823.

Uy, B. and Tuem, H.S., 2006. Behaviour and design of composite steel-concrete beams under combined actions. In Proceedings of the 8th International Conference on Steel-Concrete Composite and Hybrid Structures (ASCCS).

Vasdravellis, G., Uy, B., Tan, E.L. and Kirkland, B., 2015. Behaviour and design of composite beams subjected to sagging bending and axial compression. Journal of Constructional Steel Research, 110, pp.29-39.

Vasdravellis, G., Uy, B., Tan, E.L. and Kirkland, B., 2012a. The effects of axial tension on the sagging-moment regions of composite beams. Journal of Constructional Steel Research, 72, pp.240-253.

Vasdravellis, G., Uy, B., Tan, E.L. and Kirkland, B., 2012b. The effects of axial tension on the hogging-moment regions of composite beams. Journal of Constructional Steel Research, 68(1), pp.20-33.

Wang, C.S., Zhai, X.L., Duan, L. and Li, B.R., 2008, September. Flexural limit load capacity test and analysis for steel and concrete composite beams with tubular up-flanges. In SHEN ZY, CHEN YY, ZHAO X Z. Tubular Structures XII: Proceedings of the 12th International Symposium on Tubular Structures. Boca Raton: CRC Press (pp. 413-420).

Wang, X., 2003. Behavior of steel members with trapezoidally corrugated webs and tubular flanges under static loading. Drexel University, Ph. D. thesis.

Wassef, W.G., Ritchie, P.A. and Kulicki, J.M., 1997. Girders with corrugated webs and tubular flanges—An innovative bridge system. In Proceedings, 14th Annual Meeting, International Bridge Conference, Pittsburgh, Pennsylvania (pp. 425-432).

Wardenier, J., Packer, J.A., Zhao, X.L. and Van der Vegte, G.J., 2002. Hollow sections in structural applications. Rotterdam,, The Netherlands: Bouwen met staal.

Wimer, M.R., 2004. Concrete filled rectangular tubular flange girders with corrugated and flat webs. M.S. Thesis, Department of Civil and Environmental Engineering, Lehigh University, Bethlehem, PA.

Wu, Q., Yoshimura, M., Takahashi, K., Nakamura, S. and Nakamura, T., 2006. Nonlinear seismic properties of the Second Saikai Bridge: A concrete filled tubular (CFT) arch bridge. Engineering Structures, 28(2), pp.163-182.

Yura, J.A., Phillips, B., Raju, S. and Webb, S., 1992. Bracing of steel beams in bridges. Center for Transportation Research, The University of Texas at Austin.

Zheng, J. and Wang, J., 2018. Concrete-filled steel tube arch bridges in China. Engineering, 4(1), pp.143-155.